MODELLING AND OPTIMIZATION STUDY OF PROTONIC CERAMIC ELECTROLYSIS CELLS

LI ZHENG

PhD

The Hong Kong Polytechnic University

2024

The Hong Kong Polytechnic University

Department of Building and Real Estate

Modelling and Optimization Study of Protonic Ceramic Electrolysis Cells

LI Zheng

A thesis submitted in partial fulfilment of the requirements for the degree of Doctor of Philosophy

May 2024

CERTIFICATE OF ORIGINALITY

I hereby declare that this thesis is my own work and that, to the best of my knowledge and belief, it reproduces no material previously published or written, nor material that has been accepted for the award of any other degree or diploma, except where due acknowledgement has been made in the text.

_____ (Signed)

___LI Zheng_____ (Name of student)

Abstract

Hydrogen serves as a clean energy carrier that holds great potential for enhancing the utilization of renewable energy and driving the transition towards a zero-carbon society in the future. Protonic ceramic electrolysis cell (PCEC) is a promising electrochemical technology for achieving efficient and sustainable large-scale hydrogen production. However, the intrinsic mixed-conducting nature of the electrolyte employed in PCEC results in the occurrence of current leakage, significantly impeding the Faradaic efficiency (FE) of PCEC. Furthermore, the chemical expansion caused by the hydration reaction between the electrolyte and gas phase raises significant concerns regarding the mechanical integrity of PCECs during operation. Therefore, current leakage and chemical expansion phenomena are challenges facing the development of PCEC. Numerical models of PCEC incorporating approaches such as the machine learning techniques and design of experiments (DOE) have been developed. The influences of various parameters on the PCEC are investigated to provide a comprehensive understanding of these phenomena.

The simulation results reveal an observed non-linear correlation between the current density and Faradaic efficiency (FE). An optimal of 82% is found at 0.4 A cm^{-2} 600 °C. When the current density further increases to 0.8 A cm^{-2}, FE and its uniformity in the PCEC are respectively reduced by 21.3% and 8.8%. While the FE shows a continuous increase with increasing anode inlet flow rate or steam fraction. The results indicate that controlling the anodic operating parameter has a greater impact on regulating the electrochemical performance and FE of PCEC compared to the cathodic operating parameter. Indicated by the DOE results, the anodic inlet steam mole fraction is identified as the most important operating parameter affecting the FE of PCEC. The optimal trade-off operating point between electrochemical performance and FE can be achieved at 0.78 A m^{-2}, 600 °C, delivering a 12.8% performance enhancement compared to the base condition. From the modelling results, it reveals that the

inclusion of chemical expansion results in a higher stress level in PCECs, accounting for more than 25% of the total stress at 600 °C. Similarly, the anode operating parameters have a greater impact on the mechanical behaviour of PCEC than the cathode operating parameters. Cathode porosity is identified as the most essential parameter to the mechanical behaviour of PCEC during the operation since increasing the cathode porosity can significantly reduce both thermal stress and chemically induced stress.

Overall, the framework proposed in this work, which combines numerical modelling with other techniques, shows its power in understanding current leakage and chemical expansion in PCECs. The modelling investigations identify the important operating and structural parameters to the current leakage and chemical expansion in PCECs. Therefore, the simulation results can serve as a guide for formulating PCEC operation strategies and manufacturing designs to control or mitigate harmful phenomena during PCEC operation. The quantified description of various parameters is obtained from this study, revealing their impacts on the electrochemical performance, FE, and mechanical characteristics of PCEC. This study offers comprehensive insights into the phenomena of current leakage and chemical expansion in PCECs, providing a deeper understanding of these critical aspects. More importantly, the developed framework can help other researchers and be extended to address other problems in PCEC.

Publications arising from the thesis

1. **Li, Z.**, Yu, J., Wang, C., Bello, I.T., Yu, N., Chen, X., Zheng, K., Han, M. and Ni, M., 2024. Multi-objective optimization of protonic ceramic electrolysis cells based on a deep neural network surrogate model. *Applied Energy*, 365, p.123236.
2. **Li, Z.**, Guo, M., Wang, C., Bello, I. T., Yu, N., Chen, X., ... & Ni, M. (2024). Thermo-chemo-mechanical analysis of protonic ceramic electrolysis cell: A statistically-designed numerical study. *International Journal of Hydrogen Energy*, *61*, 173-187.
3. **Li, Z.**, Bello, I. T., Wang, C., Yu, N., Chen, X., Zheng, K., & Ni, M. (2023). Revealing interactions between the operating parameters of protonic ceramic electrolysis cell: A modelling study. *Applied Energy*, *351*, 121886.

Acknowledgements

I would like to express my deepest gratitude and appreciation to all those who have supported and contributed to the completion of this PhD thesis. First and foremost, I am very grateful to my supervisor Prof. Ni Meng, who has guided and supported me throughout this journey. His valuable insights and encouragement have been strongly helpful for me to enhance my research. I would like to acknowledge my co-supervisor Prof. Zheng Keqing for sharing her expertise in solid oxide fuel cells and numerical modelling.

I would like to acknowledge all the faculty and staff of the Department of Building and Real Estate for providing a pleasant academic environment and efficient resources for my research. I would also like to acknowledge the financial support provided by the Research Grants Council of Hong Kong and The Hong Kong Polytechnic University. Their funding enables me to carry out my research as well as enhance my career development by attending international conferences.

I would like to thank all my colleagues and friends who shared their expertise, experiences, and discussions. Their contributions enrich me and my thesis. Finally, I would like to express my gratitude to my family for their support throughout this challenging journey.

Table of contents

List of tables

List of figures

Nomenclature

Abbreviation

PCEC	Protonic ceramic electrolysis cell
SOEC	Solid oxide electrolysis cell
MCEC	Molten carbonate electrolysis cell
AEC	Alkaline electrolysis cell
PEMEC	Proton exchange membrane electrolysis cell
HC	Hydrocarbon
FE	Faradaic efficiency
OCV	Open-circuit voltage
DFT	Density functional theory
TPB	Triple phase boundary
DPB	Double phase boundary
MPEC	Mixed-protonic and electronic conducting
NPP	Nernst-Planck-Poisson
DOF	Degree of Freedom
DOE	Design of Experiments
CTE	Coefficient of thermal expansion
CCE	Coefficient of chemical expansion
OFAT	One-Factor-At-a-Time
DNN	Deep neural network
ML	Machine learning
SVM	Support Vector Machines
GA	Genetic algorithm
PSO	Particle swarm optimization
NSGA	Non-dominated sorting genetic algorithm
R^2	R-squared
RMSE	Root-mean-square-error
GSA	Global sensitivity analysis

SSA	Sobol sensitivity analysis
SI	Sensitivity index
SU	Steam utilization
NSGA	Non-dominated Sorting Genetic Algorithm
TOPSIS	Technique for Order Preference by Similarity to an Ideal Solution
AI	Artificial intelligence

Letters

P_k	Percolation probability
$Z_{k,k}$	Average number of contacts between k particles
ϕ_k	Volume fraction
r_k	Particle-radii
Z_{avg}	Average total coordinate number, 6
$\lambda_{TPB,V}^{eff}$	TPBs per unit volume, m m^{-3}
n_e^V	Number density of electronic particles, no. m^{-3}
θ	Contact angle, 30°
$\lambda_{TPB,A}^{eff}$	Area-specific TPBs, m^2 m^{-3}
S_{por-k}	Area of k particles exposed to the pore-phase, m^2
σ_k^0	Intrinsic conductivity of k phase
ε	Porosity
ζ	Bruggeman factor
σ_k^{eff}	Effective conductivity, S m^{-1}
S_{Ni}^{eff}	Effective specific Ni surface area, m^2 m^{-3}
d_{pore}	Average pore diameter, m
κ	Permeability of porous media, m^2
$\boldsymbol{i_k}$	Current vectors, A m^{-3}
φ_k	Electrochemical potential of k phase, V
i_0	Exchange current density, A m^{-2}
c_i	Concentration of species i, mol m^{-3}
J_i	Molar flux of species i, mol m^{-2} s^{-1}

β_i	Coefficient of chemical expansion, m^3 mol^{-1}
D_i^{eff}	Effective diffusion coefficient of species i, m^2 s^{-1}
F	Faraday constant, 96458.3 C mol^{-1}
ε_{abs}	Absolute permittivity of the membrane material, C V^{-1} m^{-1}
z_i	Number of charges carried by the species i
p_i	Gas partial pressure of gas species i
c_i	Concentration of species i, mol m^{-3}
$k_{f/b}$	Forward or backward reaction rate coefficient
K_{eq}	Equilibrium constant for reaction
$[X_B]$	Molar concentration of defect species X_B, mol m^{-3}
V_m	Molar volume of the electrolyte materials, m^3 mol^{-1}
$[X_B]_L$	Defect unit concentration
ΔS°	Entropy change, J mol^{-1} K^{-1}
ΔH°	Enthalpy change, J mol^{-1}
D_i^0	Pre-exponential factor of diffusion coefficient
E_{act}	Activation energy, J mol^{-1}
E_{eq}	Equilibrium potential, V
ΔG^0	Standard Gibbs energy change, J mol^{-1}
n	Number of charges transferred
R	Universal gas constant, 8.31446 J mol^{-1} K^{-1}
T	Absolute temperature, K
$a_{Red/ox}$	Activity of reduced/oxidised species
$\alpha_{a/c}$	Charge transfer coefficient for anodic/cathodic electrochemical reaction
$\eta_{act,a/c}$	Anodic/cathodic activation overpotential, V
$i_{a,c}^0$	Anodic/cathodic exchange current density, A m^{-2}
$\gamma_{a/c}$	Pre-exponential factor of anodic/cathodic exchange current density
i_{op}	Operating current density, A m^{-2}
V_{op}	Operating voltage, V
η_{conc}	Concentration overpotential, V
T_{op}	Operating temperature, K

P_{op}	Operating pressure, Pa
R_i	Reaction rate, mol m^{-3} s^{-1}
y_i	Molar fraction for gas species i
ν_i	Stoichiometric coefficient of species i
$\boldsymbol{u}$	Velocity vector, m s^{-1}
ρ	Density, kg m^{-3}
μ	Viscosity, Pa s
ω_i	Mass fraction of species i
M_i	Molar mass of species I, kg mol^{-1}
φ_{ij}	Inter-collisional parameter
$\boldsymbol{N}_i$	Molar flux of species i, mol m^{-2} s^{-1}
D_{iK}^{eff}	Effective Knudsen diffusion coefficient of species i, m^2 s^{-1}
τ	Tortuosity of porous media
D_{ij}^{eff}	Effective binary diffusion coefficient, m^2 s^{-1}
D_{ij}^{0}	Intrinsic binary molecular diffusion coefficient, m^2 s^{-1}
Ω_D	Temperature-dependent collision integral
T_b	Boiling temperature at the standard air pressure, K
A-H	Empirical constants used in Chapman-Enskog relation
C_p	Specific heat capacity, J kg^{-1} K^{-1}
k_{eff}	Effective thermal conductivity, W m^{-1} K^{-1}
η_{ohmic}	Ohmic overpotential, V
∇T	Temperature gradient, K m^{-1}
$\boldsymbol{\varepsilon}$	Strain
$\boldsymbol{I}$	Unit tensor
α	Coefficient of thermal expansion, K^{-1}
T_{ref}	Reference stress-free temperature, K
$\boldsymbol{D}$	Elastic matrix
$\boldsymbol{\sigma}$	Stress, Pa
K	Bulk modulus, Pa
G	Shear modulus, Pa

ν_i	Poisson ratio
E_i	Young's modulus
Γ	Indicator for describing the uniformity
$\overline{FE}$	Mean faradaic efficiency, %
F_i	Molar flow rate of specie i, mol s^{-1}
Q_i	Source term i
$x_{an/ca,inlet}$	Inlet composition at the anode/cathode side gas channel, %
$v_{an/ca,inlet}$	Inlet volumetric flow rate at the anode/cathode side gas channel, SCCM or kg s^{-1}
SS	Sum of squares
$y_{real/pred}$	Real value or predicted value
S_i	Sobol sensitivity index
ed	Electron-conducting phase
el	Electrolyte phase
re	Reversible heat
ir	Irreversible heat
tot	Total strain
ela	Elastic strain
therm	Thermal strain
chem	Chemically-induced strain

Chemical species & charged species

H_2	Hydrogen
NH_3	Ammonia
CO_2	Carbon dioxide
CO	Carbon monoxide
H_2S	Hydrogen sulphide
H_2O	Water
O_2	Oxygen
KOH	Potassium hydroxide
Na_2CO_3	Sodium carbonate
$LiAlO_2$	Lithium aluminate

$Ni(OH)_x$	Nickel hydroxide
YSZ	Yttria-stabilized zirconia
SDC	Samaria-doped ceria
GDC	Gadolinium-doped ceria
BZY	Yttrium-doped barium zirconate
BZCY	Yttrium-doped barium zirconate-cerate
H^+	Proton
OH^-	Hydroxide
CO_3^{2-}	Carbonate ion
$O_O^\times$	Lattice oxygen
$OH_O^\cdot$	Proton defect
$V_O^{\cdot\cdot}$	Oxygen vacancy
$O_O^\cdot$	Oxygen-site polaron
Y_{Zr}'	Yttrium-dopant

Chapter 1 Introduction

1.1 Background

Climate change and the energy crisis represent two urgent challenges that humanity must address. On one hand, the heavy dependence on fossil fuels not only contributes to excessive emissions of harmful pollutants like carbon dioxide and sulphur dioxide but also contributes to the ongoing issue of climate change [1]. On the other hand, the unsustainable exploitation of fossil fuel reserves accelerates their depletion, leading to an imminent energy crisis [2]. Consequently, it is imperative to foster a revolution in our current energy structure. The development and widespread adoption of renewable and clean energy sources to replace fossil fuels has become an imperative task. Wind and solar power are excellent renewable sources of energy for generating clean electricity without producing harmful emissions [3]. While wind and solar power possess numerical advantages, they are highly dependent on local geography and weather conditions, causing their main challenge to be intermittency [3]. This intermittency can lead to wasted or underutilized electricity generation when demand is inconsistent with the availability of wind or solar power. For example, in 2016, approximately 50 TWh of electricity generated from wind power was unused in China, accounting for nearly 17% of the total wind power generation [4]. This resulted in an economic loss of around 3.4 billion USD [4]. Hydrogen is a clean and efficient chemical fuel that has the potential to solve this problem. When wind and solar power are used for powering the electrolysis cells, the excess electrical energy that cannot be immediately utilized can be stored in the form of hydrogen [5]. The produced hydrogen can be easily converted back into electricity using fuel cells when there is a high electricity demand [6]. Hydrogen is therefore a promising and flexible energy carrier that can further reduce waste and improve the overall efficiency of energy systems through efficient storage and utilization of excess renewable energy. In this regard, developing

advanced electrolysis cells is becoming increasingly important to achieve efficient, large-scale hydrogen production. There are many types of electrolysis cells, in which protonic ceramic electrolysis cell (PCEC) is very attractive and has specific advantages. The comparison between PCEC and other electrolysis cells is shown in Table 1-1.

Table 1-1 The comparison between PCEC and other electrolysis cell [7–12].

Electrolysis cells	**Operating temperature, ° C**	**Noble/non-noble Catalyst**	**Typical electrolyte (charge carrier)**	**Efficiency, %**
Protonic ceramic electrolysis cell (PCEC)	400-600	Non-noble	BZY(H^+)	70-90
Solid oxide electrolysis cell (SOEC)	800-1000	Non-noble	YSZ(O^{2-})	<110
Molten carbonate electrolysis cell (MCEC)	600-700	Non-noble	Na_2CO_3 in $LiAlO_2$ (CO_3^{2-})	70-82
Alkaline electrolysis cell (AEC)	25-200	Non-noble	KOH solution (OH^-)	60-80
Proton exchange membrane electrolysis cell (PEMEC)	60-180	Noble	Nafion® membrane (H^+)	65-80

The operation of PCEC does not depend on noble metal catalysts, thanks to its high operating temperature [13]. In addition, the operating temperature enables PCEC can utilize the thermal energy, leading to a higher efficiency [14]. This makes PCEC more economically attractive than low-temperature electrolysis cells such as PEMEC. Compared with high-temperature electrolysis cells such as MCEC, PCEC is equipped with a solid electrolyte, enabling it a more

stable and safer operation [15]. This makes PCEC more technologically attractive. An interesting comparison is between PCEC and SOEC. As illustrated, the operating temperature of PCEC is slightly lower than that of SOEC, which allows for richer material choices and longer service life [16]. This makes PCEC more technically and economically viable [16,17]. Therefore, based on the above discussion, it can be acknowledged that PCEC is a promising technology that can serve as a key engine for building a hydrogen society in the future. However, it must be admitted that PCEC is still an immature technology. More efforts should be devoted to its research. This section will next review the working principle.

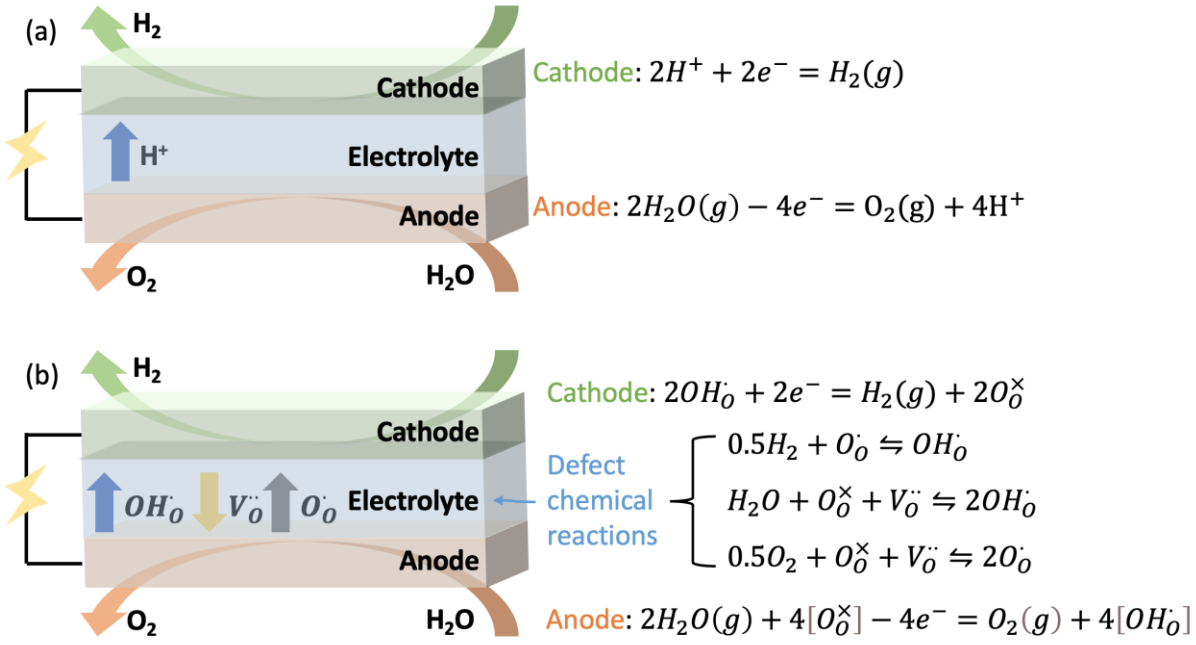

Figure 1.1 Schematics of (a) working principle of PCEC using a pure proton conductor; (b) working principle of PCEC using a mixed conductor.

In Figure 1.1 (a), it demonstrates that H_2O as a hydrogen carrier can provide protons to cathodic electrochemical reactions for producing H_2. Likewise, an incomparable advantage of PCEC compared to SOEC is that no H_2O is generated in the cathode [14]. This characteristic allows the PCEC system to ignore the downstream separation process between H_2 and H_2O, which is an indispensable process in the SOEC system [18]. This can not only remarkably simplify the

operation, but also greatly simplify the design of the entire system. For this reason, using PCEC for large-scale H_2 production is more economically promising than using SOEC. Additionally, the absence of H_2O in the cathode of PCEC can avoid Ni oxidation, which is one of the most important causes of SOEC cathode degradation [19,20]. In the cathode of SOEC, the presence of H_2O may react with the Ni particles to generate volatile $Ni(OH)_x$ species which is widely considered to be the mechanism leading to Ni coarsening [21–23]. Ni coarsening is also one of the reasons leading to the performance degradation of SOEC [24]. This illustrates that the Ni coarsening can be inhibited in the cathode of PCEC. Moreover, in previous experimental studies of SOEC, it is found that the delamination of the anode from the electrolyte should be the dominant reason for the performance degradation [25–27]. Previous findings show that the delamination tends to occur under high oxygen partial pressure and high temperature (> 750 °C) conditions [28–31]. As shown in Table 1-1, PCEC can operate under a lower temperature than SOEC. Based on the above discussion, unlike the counterpart SOEC, PCEC exhibits the potential to operate stably for a long time without significant degradation. This also demonstrates the technological advantages of PCEC.

1.2 Literature review

This section will review the latest progress of PCEC and the challenges facing its development. Currently, many researchers have devoted tremendous efforts to the development of PCECs. Vøllestad et al. developed a tubular PCEC using $BaZr_{0.7}Ce_{0.2}Y_{0.1}O_{2.95}$ as an electrolyte (10 cm^2 active area) [32]. The highest hydrogen production rate was found to be around 0.8 ml min^{-1} cm^{-2} at 600 °C. Duan et al. developed a $BaCe_{0.7}Zr_{0.1}Y_{0.1}Yb_{0.1}O_{3-\delta}$ -based PCEC, which can also operate in fuel cell mode efficiently [33]. Additionally, numerous studies have reported excellent results in terms of hydrogen production rate [33–36]. For example, Ding et al. reported a hydrogen production rate of nearly 90 ml cm^{-2} h^{-1} at 550 °C, 1.4V, which is

substantially higher than the hydrogen production rate of a typical PEMEC [37–39]. However, a major disadvantage of PCEC, current leakage, can be caused by the intrinsic property of electrolyte materials. Explicitly, the electrolyte material is not a pure proton conductor but a mixed conductor [40]. For example, many experimental data show that the Yttria-doped Barium Zirconate (BZY), a typical proton-conducting electrolyte used in PCEC, can conduct other charge carriers besides protons [41,42]. Specifically, in addition to protons ($OH_O^{\cdot}$), the oxygen vacancies ($V_O^{\cdot\cdot}$) and polarons ($O_O^{\cdot}$) can also transfer through the electrolyte. Those charge carriers can be generated via the defect chemical reactions between the gas species and electrolyte material [43]. For example, in Figure 1.1 (b), the polarons can be generated through the reaction between oxygen, lattice oxygen and oxygen vacancies in the electrolyte. Additionally, the polarons can react with the electrons released by the electrochemical reactions [44–46]. In such a way, electrons cannot fully react with protons to generate hydrogen, which considerably weakens the faradaic efficiency (FE) of PCEC [32,37]. Therefore, the conduction of polarons is significantly detrimental to the electrochemical performance of PCEC. For a PCEC using BZY20 as the electrolyte, the maximum FE is only around 40% under 600 °C with an 80% O_2-20% H_2O gas composition in the anode [47]. The current leakage is a troublesome problem hindering the development of PCEC. Some experimental efforts have been made to understand and investigate the current leakage phenomenon in PCEC.

The effects of doping concentration on the properties of BZY and Yttria-doped Barium Zirconate-Cerate (BZCY) have been investigated experimentally. It shows that in BZY, the protonic defects and oxygen vacancies tend to be located near the Y cations while increasing the partial pressure of H_2O can suppress the current leakage [48]. Small grains and numerous grain boundaries are observed in BZY, leading to a lower conductivity of BZY [49]. It is found that although increasing the doping of Ce can enhance the proton uptake of BZCY, it reduces

the stability of the electrolyte under humidified conditions [50]. To inhibit the current leakage and improve the FE of the PCEC, some fabrication strategies have been experimentally developed by many researchers [51]. For example, a heterogeneous design of PCEC is conceived, from which the electrochemical performance benefited [52]. In other words, the electrolyte particles in the anode are different from the material used as the electrolyte. It is found that with this novel design, the FE is improved by 10% at 1.3 V, 823 K. In addition, some researchers work on another strategy, i.e., using a hole-blocking layer supported on the proton-conducting electrolyte, to suppress the current leakage [53–55]. It is found that although the proton conductivity of the hole-blocking layer is lower than that of BZY, its low electronic hole transport number can efficiently block the transport of electronic holes. In addition, the electrochemical testing results show that this bilayer design of the electrolyte is an efficient strategy to increase both open-circuit voltage (OCV) and FE of the PCEC.

In addition to these experimental studies, some numerical investigations have been performed [56]. Unlike early developed numerical models of PCEC [57–59], in which the electrolyte is considered a pure proton conductor, recent modelling studies have considered the transport of various charge carriers in the electrolyte to simulate current leakage phenomenon. Zhang and co-workers develop a numerical model to account for the current leakage in the BZY20 [60]. Notably, an analytical solution is derived in their work to quantitatively describe the amount of leakage currents in the BZY20. The results suggest that the FE at a high temperature is generally lower than that at a low temperature. Another numerical model is developed to investigate the defect transport in the radial direction through the BZY20 [61]. Both steady-state and transient behaviours of the BZY20 membrane are taken into consideration. Unlike the previous numerical work, in which the analytical equation is applied to describe the leakage current, a Nernst-Planck-Poisson (NPP) model is developed in this work to describe the transport of different charge carriers through the BZY20 membrane. As a result, this NPP

model can systematically describe the complex transport processes of different charge carriers through the electrolyte, thereby unveiling the mechanism of leakage current. Thereafter, Zhu et al. further apply this NPP model to a PCEC using BZY10 as the electrolyte [62]. The effects of environmental atmosphere composition on the OCV of PCEC are well-investigated in their work. Their 1D model results show that the FE is higher at a lower operating temperature. Furthermore, it also indicates that FE tends to be higher at a higher voltage when the operating temperature is fixed. A 1D model is developed for another proton conductor, BCZYYb711 [63]. The hydration thermodynamics and transport characteristics in this material are investigated. It is found that this material could achieve a higher FE at 600 °C compared to BZY20. Priya and Aluru [64] develop a multiscale model of BZY15 based PCEC model. an important contribution in their model is using density functional theory (DFT) to calculate the energy barriers of electrochemical reactions and defect chemical reactions. Therefore, the information obtained from the micro-scale model (DFT) can be used as input in the cell-level model. The results found that the reducing or oxidizing environment can significantly affect the performance of electrolyte. PCEC is more fit to the oxidizing environment. Putilov et al. [65] propose a 1D model of PCEC to study the role of acceptor impurities on the transport of protons and oxygen vacancies in the electrolyte. Results demonstrate a substantial interaction between the acceptor impurities and protonic defects. Their work also demonstrates the possibility of various acceptor impurities to modulate the FE of PCEC. Virkar [66] derives the transport flux of various charge carriers in the electrolyte based on the equilibrium between the electrochemical potential. In addition, the OCV of the PCEC is expressed in the Goldman–Hodgkin–Katz form. The analysis also shows the distribution of chemical potential of H_2 and O_2 across the cell. Additionally, some modelling studies offer theoretical support for the implementation of the bilayer electrolyte strategy. Ortiz-Corrales and coworkers [67] develop a 1D model to simulate bilayer electrolyte with BZY20 in the hydrogen electrode side and

LWO in the oxygen electrode side. The leakage current can be effectively blocked by the LWO layer, and the FE can reach 90% with the bilayer electrolyte. Otomo et al. [68] demonstrate that the thickness of LWO should be well controlled since its proton conductivity is smaller than that of BZY20. The optimal thickness is identified to be 1 μm in their study. Another study done by Lei et al. [69] investigates the complex transport process in proton-conducting electrolytes from the perspective of oxygen ion conduction. The simulation suggest that the oxygen ion conduction is mainly affected by the partial pressure of steam in the hydrogen electrode side, rather than that in the oxygen electrode side. The oxygen ion conduction in the electrolyte can be significantly enhanced by decreasing the partial pressure of steam in the hydrogen electrode side.

Although the previous studies could provide a comprehensive description of the complicated transport processes within the electrolyte, the heat transport in the PCEC is not taken into consideration. The heat transport can significantly affect the temperature distribution in the PCEC, thereby affecting the electrochemical performance of the PCEC [70]. In addition, as previous studies reveal, the FE of PCEC is very sensitive to temperature. Hence, taking heat transport into account can provide a more realistic understanding of the current leakage phenomenon in PCEC. With the consideration of heat transfer in the PCEC, a comprehensive description of the effects of various operating parameters on the electrochemical performance as well as the FE of PCEC should be provided by a numerical model. Furthermore, previous studies are all one-dimensional (1D) models, i.e., along the cell thickness direction. From Ref. [71], authors derives an analytical expression of molar flux of charge carriers in the electrolyte as a function of concentration of gas species along the gas channel. In this regard, the effects of gas species concentration distribution on the transport of charge carriers within the electrolyte should be incorporated into the model. Therefore, two-dimensional (2D) models should be developed to provide valuable information on PCEC along both the cell length direction and the cell thickness direction. The numerical model of PCEC can not only

accurately describe the leakage current of PCEC, but also help researchers study the effects of various operating parameters on the electrochemical performance and FE of PCEC.

In addition to the current leakage in PCEC, there is another phenomenon that should be considered, namely, chemical expansion. The chemical expansion has been reported in previous experimental studies of PCECs [92]. As shown in Figure 1.1 (b), steam can react with the deficiencies in the electrolyte material, the process of which is known as hydration reaction [93]. Two protonic defects can be produced from the hydration reaction, eventually leading to the lattice expansion in the electrolyte material on a microscopic scale. The hydration reaction can take place between the electrolyte material and steam even under the open-circuit condition [94]. However, when the current is provided to the PCEC, the charge transfer reactions will pose a significant impact on the concentration of protonic defects [95]. As shown in Figure 1.1, the protonic defects will be generated and consumed in the anodic and cathodic charge transfer reactions respectively. The concentration of protonic defect in the anode side tends to be higher than that in the cathode side. The charge transfer reactions in the cell would affect the chemical expansion significantly via the producing/consuming the protonic defects. Therefore, chemical expansion is an important phenomenon that should be considered in PCEC mechanical simulations. Chen and co-workers show that a reduced chemical expansion in PCEC can contribute to an improvement in its durability [94]. They find that the doping concentration has an impact on the chemical expansion of proton conductor (BCZY). It demonstrates that the chemical expansion would decrease with the decreasing Zr content. A similar result is reported by Zvonareva et al. [96]. They observe the chemical expansion in $BaSn_{1-x}Y_xO_{3-\delta}$ is enhanced with an increase in Y-content. Similar to thermal expansion, such a chemical expansion can also cause chemically induced mechanical stress [97]. Considering the significance of both thermal expansion and chemical expansion, it is crucial to incorporate them into the numerical model. This inclusion will provide a comprehensive understanding of the mechanical stress

experienced during the operation of the PCEC. Such understanding is vital for improving the durability and stability of the PCEC. Although the mechanical analysis of PCECs is limited, many studies on the mechanical analysis of SOECs have emphasized the importance of understanding how various parameters affect the mechanical behaviour of SOECs [98–101]. For example, Han et al. [99] propose a new design of SOEC using the metal foam, which showed a significant effect on enhancing the heat transfer process in SOEC. It is found that compared to conventional design, the maximum temperature in the cell can be reduced by more than 35 K, while the maximum thermal stress can be reduced by around 70%. Sun et al. [100] investigate the thermal stress distribution in the SOEC by examining the effects of different operating parameters. The operating temperature is found to be the most significant parameter. Wang et al. [102] perform a mechanical analysis on the SOEC to evaluate the crack formation. Their results show that the galvanostatic electrolysis mode is more robust in terms of mechanical integrity compared to the potentiostatic electrolysis mode, which became more prominent at high current densities. Furthermore, Bao et al. [103] apply risk-of-rupture approach to conduct the reliability analysis on the SOEC by considering the thermal stress. A potential risk of cell failure is indicated from their results reliability analysis when the operating voltage is much higher than the thermoneutral voltage. With this knowledge, a more rational operation strategy can be developed to play a crucial role in enhancing the durability and stability of the PCEC system. Therefore, it is essential to perform a thermo-mechanical analysis of PCEC. Furthermore, it is worth noting that some numerical studies on the chemical expansion of doped ceria materials used in SOEC have been reported. Zhu and coworkers simulate the mechanical stress in a SOEC using samaria-doped ceria (SDC) [104]. They suggest that the working temperature of SOEC should be less than 700 °C to reduce the stress-level in a SOEC. In addition, Lenser et al. simulate the chemical expansion in a SOEC using gadolinium-doped ceria (GDC) [105]. It shows that the decreased partial pressure of oxygen

can affect the chemical expansion of GDC, resulting in substantial chemically induced stress. Terada et al. [106] investigate the chemical expansion in GDC in SOFC operation. It is found that the expansion at the cathode and anode leads to compressive stresses, which are counterbalanced by tensile stresses in the electrolyte. Swaminathan et al. [107] formulate an electro-chemo-mechanical theory that integrates electrical potential with the transport of defects, establishing a connection between mechanical stress and defect transfer. However, modelling work specifically on the chemical expansion of PCEC has yet to be completed. Therefore, in Chapter 4, the modelling work considering both chemical and thermal expansion in PCECs will be introduced in detail.

Furthermore, there exists a trade-off between the electrochemical performance and Faradaic efficiency (FE) of PCEC due to the tendency of electrochemical performance to improve at higher temperatures, whereas FE tends to exhibit the opposite behaviour [72]. Hence, when the electrolyte material is predetermined, it becomes significant to regulate the operating parameters of PCEC to achieve a balance between electrochemical performance and Faradaic efficiency. This route holds promise for enhancing the overall efficiency of PCEC. To address this research gap, it is necessary to undertake a multi-objective optimization study of PCEC. Due to the computational cost associated with considering the complex transport processes in the electrolyte in the numerical model, employing a surrogate model is advantageous in performing the optimization process. This allows for faster evaluations and iterations during the optimization process, enabling more efficient exploration of the parameter space and accelerating the overall optimization of PCEC. Deep neural network (DNN) can be used to fulfil this requisite. It has been reported that the average maximum relative error in predictions of electrochemical performance using a DNN model can be less than 1% [73–75]. Moreover, the efficiency of the DNN model is highlighted by the fact that obtaining a solution requires less than 1 second, compared to the more than 3 minutes needed for solving numerical models

[76]. Consequently, the DNN model proves to be a rapid and precise means of reproducing the results derived from the numerical model [77,78]. In addition to the DNN model, several conventional machine learning (ML) models, such as Support Vector Machines (SVM) and Bayesian networks, can be employed in the domains of fuel cells and electrolysis cells as well [79,80]. Numerous studies have conducted comparisons between neural network models and traditional ML methods. While it is observed that DNN models necessitate a larger volume of data for training compared to traditional models, consequently extending the training duration [81,82]. The feature selection process in DNN model is notably simpler and time efficient. Importantly, the findings underscore that the DNN model consistently outperforms traditional methods, especially in multivariate output regression [83–86]. Therefore, the selection of DNN is motivated by its demonstrated high performance. The most common used multi-objective algorithms in the domain of fuel cell and electrolysis cells simulations are evolution based algorithms and swarm based algorithms [87,88]. Both categories are heuristic optimization methods. Evolution-based algorithms, such as Genetic algorithm (GA), are inspired by the natural selection/genetics [89]. Swarm-based algorithms, typified by Particle swarm optimization (PSO), draw inspiration from social behaviour of animals [90]. Some work studies have been undertaken to compare the performance of these algorithms. Notably, in an optimization study of a fuel cell/gas turbine system, PSO demonstrated superior convergence performance over GA [91]. However, in a fuel cell/electrolysis cell system optimization study, GA outperformed PSO in terms of finding optimal solutions. Hence, the comparison of algorithm performance should be problem specific. In the following optimization work introduced in Chapter 5, GA is used for optimization process. Noteworthy, given the multi-objective nature of the study, the GAs capable of handling multiple objectives should be utilized.

Based on the literature review, the research gaps are summarized as follows: Firstly, a 2D model of PCEC that considers the influences of heat transport and gas species distribution along the cell length on the charge transfer in the electrolyte should be developed. This will result in a more realistic portrayal of PCEC behaviour. Secondly, a comprehensive model of PCEC that considers both thermal and chemical expansions should be constructed to provide insights into the role of chemical expansion and the mechanical properties of PCEC during operation. Lastly, incorporating faraday efficiency into consideration in multi-objective optimization study in PCEC is crucial, which aims to strike a balance between electrochemical performance and faradaic efficiency.

1.3 Research objectives

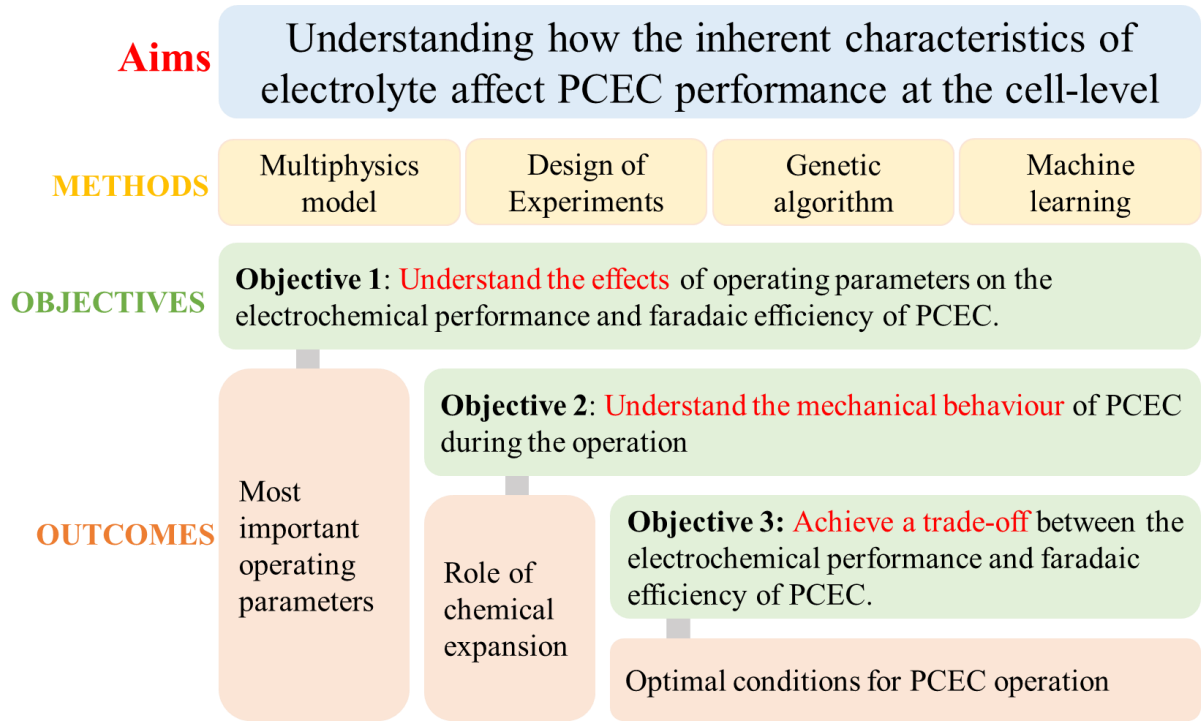

Figure 1.2 Outline of thesis.

The overall goal of this research work is to develop a 2D comprehensive model to accurately understand how the inherent characteristics of electrolyte, i.e. current leakage and chemical

expansion affect the electrochemical performance, Faradaic efficiency, and mechanical behaviour of PCECs. In addition, the objectives of this research are shown in Figure 1.2:

1) Provide the understanding of the main effects of various operating parameters and interactions between them on the electrochemical performance and faradaic efficiency of PCEC by a numerical model combined with the design of experiments (DOE) method.
2) Obtain a comprehensive mechanical understanding of PCEC during the operation using a numerical model integrated with DOE method.
3) Achieve a trade-off between the electrochemical performance and faradaic efficiency of PCEC via a numerical model coupled with a machine learning accelerated optimization process.

After achieving the three objectives, some important outcomes can be captured, as shown in Figure 1.2. In addition, the originalities of this research can be summarized as follows:

1) Heat transfer in PCEC is considered, making the simulation results more persuasive and accurate.
2) 2D model is developed to provide valuable information along both cell length and cell thickness directions, which enables the consideration of the effect of species concentration distribution on different charge carrier transport in the electrolyte.
3) DOE method is applied to enable a statistically designed numerical study.
4) The chemical expansion the PCEC electrolyte is accounted for, enabling a more realistic prediction.

Chapter 2 Methodologies for developing numerical model, surrogate model and parametric studies

2.1 Percolation theory

Percolation theory is widely applied in SOEC/PCEC modelling to portray the relationship between the microstructural properties of electrodes and the effective properties of electrodes. Detailed information concerning the percolation theory can be found in Refs. [108,109]. A percolation probability, P_k, defining the possibility of particles forming effective-connected conduction paths, can be determined as [110,111]:

$$P_k = 1 - (\frac{4.236 - Z_{k,k}}{2.472})^{3.7} \tag{2-1}$$

where $Z_{k,k}$ is the average number of contacts between k particles, which can be determined by volume fraction (ϕ_k) and the radii of particles (r_k) [108,109,112]:

$$Z_{el,el} = Z_{avg} \frac{\phi_{el}/r_{el}}{\phi_{ed}/r_{ed} + \phi_{el}/r_{el}} \tag{2-2}$$

$$Z_{ed,ed} = Z_{avg} \frac{\phi_{ed}/r_{ed}}{\phi_{ed}/r_{ed} + \phi_{el}/r_{el}} \tag{2-3}$$

where Z_{avg} represents the average total coordinate number and is assigned to be 6 in a random packing spheres system [109]. The subscripts el and ed denote the electrolyte phase and electrode phase, respectively. Moreover, the average number of contacts between two different particles, $Z_{el,ed}$, can be estimated as [109]:

$$Z_{el,ed} = \frac{1}{2}\left(1 + \frac{r_{el}^2}{r_{ed}^2}\right) Z_{el,el} \tag{2-4}$$

Consequently, based on percolation probability and number of contacts, some effective microstructural properties of porous electrodes can be calculated and listed as follows.

2.1.1 Effective electrochemically active length (area) per unit volume

Firstly, the triple-phase boundaries (TPBs) per unit volume (m m^{-3}), $\lambda_{TPB,V}^{eff}$, can be calculated as:

$$\lambda_{TPB,V}^{eff} = 2\pi min(r_{ed}, r_{el}) P_{ed} P_{el} n_{ed}^{V} Z_{ed,el} sin(\theta/2) \quad (2\text{-}5)$$

where n_{ed}^{V} represents the number density of electronic particles (no./m^3), namely, $n_{ed}^{V} = \big((1-\varepsilon)\phi_{ed}\big)/(4\pi r_{ed}^3/3)$. θ assumed to be 30°, is the contact angle between different particles. The selected contact angle is based on a 1998 publication that introduced this angle without providing a rationale. Numerous researchers have incorporated this contact angle into their models. Nonetheless, the specific value of the contact angle can influence the computation of microstructural properties. A 20% increase or decrease in the contact angle can lead to a corresponding 19% and 20% rise or fall in the results of $\lambda_{TPB,V}^{eff}$. Consequently, a comprehensive investigation into the validity of this contact angle assumption for the porous electrodes of PCECs is crucial for forthcoming research endeavours. Secondly, for mixed-protonic and electronic conducting (MPEC) materials, the TPBs can be extended to percolated double-phase boundaries (DPBs) [113]. Thus, this area-specific TPBs (m^2 m^{-3}), $\lambda_{TPB,A}^{eff}$, can be expressed by the following formulas [114]:

$$\lambda_{TPB,A}^{eff} = n_{MPEC}^{V} S_{por-MPEC} P_{MPEC}^{e} P_p \quad (2\text{-}6)$$

where P_p is the percolation probability for the proton-conducting phase. Since both MPEC and electrolyte particles can provide conducting pathways for protons, P_p is assumed to be 1. $S_{por-MPEC}$ (m^2) defines the area of MPEC particles exposed to the pore phase, shown as [114]:

$$\begin{aligned} S_{por-MPEC} = 2\pi r_{MPEC}^2 [2 - (1-\cos\theta_{MPEC}) Z_{MPEC,MPEC} \\ - (1-\cos\theta_{MPEC}) Z_{MPEC,el}] \end{aligned} \quad (2\text{-}7)$$

2.1.2 Effective conductivity

In the porous electrodes, the intrinsic conductivity of k phase, σ_k^0, should be corrected according to the following equation [115]:

$$\sigma_k^{eff} = \sigma_k^0[(1-\varepsilon)\phi_k P_k]^\zeta \tag{2-8}$$

where ε is the porosity, ζ signifies the Bruggeman factor (typically set to 1.5-3) [115], σ_k^{eff} is the effective conductivity (S m^{-1}).

2.1.3 Average pore diameter

The average pore diameter (m) is an important parameter of a porous medium, which can be calculated as [114]:

$$d_{pore} = \frac{4}{3}\left(\frac{\varepsilon}{1-\varepsilon}\right)\frac{1}{\phi_{ed}/r_{ed} + \phi_{el}/r_{el}} \tag{2-9}$$

Subsequently, the permeability of a porous medium (m^2) can be defined as [114]:

$$\kappa = \frac{\varepsilon^3 d_{pore}^2}{72\tau(1-\varepsilon)^2} \tag{2-10}$$

2.2 Charge transfer

The transport of electrons obeys Ohm's law associated with the charge continuity equations [116].

$$\nabla \cdot \boldsymbol{i}_{ed} = \nabla \cdot \left(-\sigma_{ed}^{eff} \nabla \varphi_{ed}\right) = -i_0 \lambda_{TPB}^{eff} \tag{2-11}$$

where $\boldsymbol{i_{ed}}$ represents the current vectors. However, proton-conducting electrolytes used in PCFCs such as BZY are mixed conducting materials. Therefore, a defect chemical model should be developed to deliver an accurate and realistic description of the transport of charged species within the electrolyte, which would be next reviewed.

2.2.1 Nernst-Planck-Poisson Model

The conservation equation of a mobile charged species through the electrolyte can be expressed as:

$$\frac{\partial c_i}{\partial t} + \nabla \cdot J_i = s_d \tag{2-12}$$

where c_i is the concentration of species i (mol m^{-3}); s_d is the source term for the defect species; J_i is the molar flux of species i (mol m^{-3} s^{-1}), which can be expressed by the Nernst-Planck equation [117]:

$$J_i = -D_i^{eff} \left(\nabla c_i + \frac{z_i F}{RT} c_i \nabla \varphi_{el} - \frac{3\,\beta_i [i]}{RT} \nabla \sigma_h\right) \tag{2-13}$$

Both diffusion and migration of charged species within the electrolyte are depicted in Eq. (2-13). Noteworthy, the third term on the right-hand side indicates the effect of stress on molar flux and is only considered when chemical expansion is considered. Where D_i^{eff} is the effective diffusion coefficient of charged species i (m^2 s^{-1}); F is the Faraday constant (96458.3 C mol^{-1}); φ_{el} stands for the electrostatic potential within the electrolyte (V). Its relationship with the local charge density can be described by the Poisson equation [118]:

$$\nabla \cdot \left(\varepsilon_{abs} \nabla \varphi_{el}\right) + F \sum_i z_i c_i = 0 \tag{2-14}$$

where ε_{abs} is the absolute permittivity of the membrane material, z_i is the number of charges carried by the species i. For species i, its current density (i_i) through the membrane can be derived based on the molar flux. Under the steady state, the external current density (i_{ex}) through the electrolyte surface is the sum of the current density of each species:

$$i_{ex} = F \sum_i z_i J_i = \sum_i i_i \tag{2-15}$$

2.2.2 Defect concentration

To solve the NPP model, the concentration of different defect species is required as a boundary condition. In this model, three defect incorporation reactions can take place between the gas phase and electrolyte phase under wet conditions.

$$0.5H_2 + O_O^{\cdot} \leftrightharpoons OH_O^{\cdot} \tag{2-16}$$

$$H_2O + O_O^{\times} + V_O^{\cdot\cdot} \leftrightharpoons 2OH_O^{\cdot} \tag{2-17}$$

$$0.5O_2 + O_O^{\times} + V_O^{\cdot\cdot} \leftrightharpoons 2O_O^{\cdot} \tag{2-18}$$

where $O_O^{\times}$, $OH_O^{\cdot}$, $V_O^{\cdot\cdot}$, $O_O^{\cdot}$ signify the lattice oxygen, proton defect, oxygen vacancy and oxygen-site polaron, respectively. The chemical reactions involving defects between the gas phases and the electrolyte material can impact the stability and overpotential of PCECs. For instance, the hydration reaction (Eq. 2-18) can alter the concentration of protonic defects within the electrolyte materials, subsequently influencing chemical expansion and the stress it induces. Consequently, the overall stability of the PCEC can be affected. Additionally, as these defect chemical reactions progress, the partial pressure of various gas phases within the PCEC undergoes changes, consequently impacting the overpotential of the PCEC. The oxygen-site polaron, which can react with the electrons and lead to current leakage, is considered the combination of electron holes and lattice oxygen. Accordingly, the rates of three defect chemical reactions can be expressed as follows:

$$r_1 = k_{f1} c_{H_2}^{0.5} c_{O_O^{\cdot}} - k_{b1} c_{OH_O^{\cdot}} \tag{2-19}$$

$$r_2 = k_{f2} c_{H_2O} c_{O_O^{\times}} c_{V_O^{\cdot\cdot}} - k_{b2} c_{OH_O^{\cdot}}^2 \tag{2-20}$$

$$r_3 = k_{f3} c_{o_2}^{0.5} c_{O_O^{\times}} c_{V_O^{\cdot\cdot}} - k_{b2} c_{O_O^{\cdot}}^2 \tag{2-21}$$

where k_f and k_b are the forward and backward reaction rate coefficients, respectively. The ratio of k_f to k_b equals the equilibrium constant for each reaction. The equilibrium of the above reactions can be written as:

$$K_{p,H_2} = \frac{[OH_O^{\cdot}]}{[O_O^{\cdot}]p_{H_2}^{0.5}} \tag{2-22}$$

$$K_{p,H_2O} = \frac{[OH_O^{\cdot}]^2}{[O_O^{\times}][V_O^{\cdot\cdot}]p_{H_2O}} \tag{2-23}$$

$$K_{p,O_2} = \frac{[O_O^{\cdot}]^2}{[O_O^{\times}][V_O^{\cdot\cdot}]p_{O_2}^{0.5}} \tag{2-24}$$

where p_i is the gas partial pressure of gas species i, $[X_B]$ is the molar concentration of defect species X_B. Its relationship with the molar volume of the electrolyte materials (V_m) and defect unit concentration ($[X_B]_L$) is shown as:

$$[X_B]_L = [X_B]V_m \tag{2-25}$$

In addition, the equilibrium constant can be thermodynamically determined via entropy change (ΔS°) and enthalpy change (ΔH°) of the defect reactions [117]:

$$K_{eq} = \exp\left(\frac{\Delta S^{\circ}}{R}\right) \cdot \exp\left(-\frac{\Delta H^{\circ}}{RT}\right) \tag{2-26}$$

Noteworthy, the data of entropy and enthalpy change of the different defect reactions can be found in Ref. [117]. In addition to the equilibrium relationships, the electroneutrality condition and oxygen-site conservation equation are necessary for obtaining the defect concentration in the electrolyte.

$$[OH_O^{\cdot}] + 2[V_O^{\cdot\cdot}] + [O_O^{\cdot}] - [Yb_{Zr}'] = 0 \tag{2-27}$$

$$[OH_O^{\cdot}] + [V_O^{\cdot\cdot}] + [O_O^{\cdot}] + [O_O^{\times}] = 3 \tag{2-28}$$

After obtaining the defect concentration, the conductivity of defect species i can be determined as:

$$\sigma_i = \frac{F^2}{RT} z_i^2 c_i D_i \tag{2-29}$$

$$D_i = D_i^0 \exp\left(-\frac{E_{act,d}}{RT}\right) \tag{2-30}$$

where D_i^0 is the pre-exponential factor of the diffusion coefficient, $E_{act,d}$ is the activation energy (J mol^{-1}) of the diffusion coefficient. The data on the diffusion coefficient can be found in Ref. [72]. Then, the total conductivity of the electrolyte phase can be written as:

$$\sigma_{el} = \sum_i \frac{F^2}{RT} z_i^2 c_i D_i \tag{2-31}$$

Noteworthy, the conductivity of the electrolyte phase needs to be corrected in the porous electrode according to the percolation theory shown in Eq. (2-8).

2.3 Electrochemistry

As shown in Figure 1.1 (a), when considering the role of defect species in electrochemical reactions, the anode and cathode electrochemical reactions can be written in the form of reduction reactions as follows:

$$O_2(g) + 4OH_O^{\cdot} + 4e^- = 2H_2O(g) + 4O_O^{\times} \tag{2-32}$$

$$2OH_O^{\cdot} + 2e^- = H_2(g) + 2O_O^{\times} \tag{2-33}$$

The Butler-Volmer equation can be implemented to describe the anodic and cathodic charge-transfer reaction rates as:

$$i_a = i_a^0\left[\exp\left(\frac{\alpha_a F \eta_{act,a}}{RT}\right) - \exp\left(\frac{-(1-\alpha_a) F \eta_{act,a}}{RT}\right)\right] \tag{2-34}$$

$$i_c = i_c^0\left[\exp\left(\frac{\alpha_c F \eta_{act,c}}{RT}\right) - \exp\left(\frac{-(1-\alpha_c) F \eta_{act,c}}{RT}\right)\right] \tag{2-35}$$

where $\alpha_{a/c}$ is the charge transfer coefficient for anodic/cathodic electrochemical reaction; $\eta_{act,a/c}$ is the anodic/cathodic activation overpotential (V); $i_{a,c}^0$ represents the anodic/cathodic exchange current density. In addition, the effects of defect species on the anodic/cathodic

exchange current density should also be considered. Hence, the expressions of $i_{a,c}^{0}$ can be written as [119]:

$$i_{0,a} = \gamma_{0,a} \exp\left(-\frac{E_{act,a}}{RT}\right)[OH_O^{\cdot}]^{\beta_a}[O_O^{\times}]^{1-\beta_a} p_{O_2}^{0.25} p_{H_2O} \tag{2-36}$$

$$i_{0,c} = \gamma_{0,c} \exp\left(-\frac{E_{act,c}}{RT}\right)[OH_O^{\cdot}]^{\beta_c}[O_O^{\times}]^{1-\beta_c} p_{H_2} \tag{2-37}$$

where $\gamma_{a/c}$ is the pre-exponential factor of anodic/cathodic exchange current density; $E_{act,a/c}$ represents the activation energy of anodic/cathodic exchange current density; p_i denotes the partial pressure of species i. The operating voltage (V_{op}) can be evaluated as:

$$V_{op} = E_{eq} + \eta_{act,a} + \eta_{act,c} + \eta_{ohm,a} + \eta_{ohm,c} + \eta_{ohm,ele} + \eta_{conc,a} + +\eta_{conc,c} \tag{2-38}$$

where η_{ohm} and η_{conc} are ohmic overpotential and concentration overpotential, respectively; E_{eq} is the equilibrium potential, which can be determined using Nernst equation [120]:

$$E_{eq} = -\frac{\Delta G^0}{nF} - \frac{RT}{nF}\ln\frac{a_{Red}}{a_{ox}} \tag{2-39}$$

where ΔG^0 is the standard Gibbs energy change (J mol^{-1}); n is number of charges transferred; R is universal gas constant (8.31446 J mol^{-1} K^{-1}); T is the absolute temperature (K); $a_{Red/ox}$ is the activity of reduced/oxidized species, respectively.

2.4 Mass and momentum transfer

The above-mentioned rate expressions are used to calculate the source terms added to the mass conservation equation, while Darcy's term modified Navier-Stokes equation is implemented to describe the momentum transport in the porous media [121]

$$\rho\nabla \cdot \boldsymbol{u} = Q_m = \sum y_i R_i \tag{2-40}$$

$$\frac{\rho}{\varepsilon}(\boldsymbol{u}\cdot\nabla)\cdot\frac{\boldsymbol{u}}{\varepsilon} = -\nabla P + \nabla\cdot\left[\frac{\mu}{\varepsilon}(\nabla\boldsymbol{u} + \nabla\boldsymbol{u}^T) - \frac{2}{3}\frac{\mu}{\varepsilon}(\nabla\cdot\boldsymbol{u})\right] - \left(\mu\kappa^{-1} + \frac{Q_m}{\varepsilon^2}\right)\boldsymbol{u} \tag{2-41}$$

where $\boldsymbol{u}$ is the velocity vector; ρ is the density (kg m^{-3}); μ is the viscosity (Pa s). Meanwhile, in the non-porous gas channel, the porosity is set as unity while Darcy's term is omitted [122]. The density as well as the viscosity of the gas mixtures are expressed as:

$$\rho = \frac{P}{RT}\sum_i \frac{\omega_i}{M_i} \tag{2-42}$$

$$\mu = \sum_i \frac{y_i \mu_i}{\sum_j y_j \varphi_{ij}} \tag{2-43}$$

$$\phi_{ij} = \frac{1}{\sqrt{8}}\left(1+\frac{M_i}{M_j}\right)^{-1/2}\left[1+\left(\frac{\mu_i}{\mu_j}\right)^{1/2}\left(\frac{M_j}{M_i}\right)^{1/4}\right]^2 \tag{2-44}$$

where ω_i is the mass fraction of each gas species; μ_i is the viscosity of each gas species; M_i is the molar mass of each gas species; φ_{ij} is the inter-collisional parameter [123]. The dust gas model is applied in this study to simulate molecular diffusion and Knudsen diffusion in porous media [124]. Noteworthy, the Knudsen diffusion of gas species is neglected in the flow channel.

$$\frac{\boldsymbol{N}_i}{D_{iK}^{eff}} + \sum_{j=1}^{n}\frac{y_j\boldsymbol{N}_i - y_i\boldsymbol{N}_j}{D_{ij}^{eff}} = -\frac{1}{RT}\left(P\nabla y_i + y_i\nabla P + y_i\nabla P\frac{kP}{D_{iK}^{eff}\mu}\right) \tag{2-45}$$

$$D_{iK}^{eff} = \frac{\varepsilon}{\tau}\frac{1}{3}d_{pore}\sqrt{\frac{8RT}{\pi M_i}} \tag{2-46}$$

$$D_{ij}^{eff} = \frac{\varepsilon}{\tau}\cdot D_{ij}^{0} \tag{2-47}$$

where $\boldsymbol{N}_i$ is the molar flux of each species (mol m^{-2} s^{-1}); D_{iK}^{eff} is the effective Knudsen diffusion coefficient of species i; τ is the tortuosity of the porous medium; D_{ij}^{eff} is the effective binary diffusion coefficient; D_{ij}^{0} is the binary molecular diffusion coefficient determined by a modified Chapman-Enskog relation [123,125–127]:

$$D_{ij}^{0} = \frac{0.042851 \times \left(\frac{1}{M_i} + \frac{1}{M_j}\right)^{-0.5} - 0.0098 \times T^{1.5}}{P\Omega_D \sigma_{ij}^2} \tag{2-48}$$

$$\Omega_D = A(T^*)^B + C\,exp(DT^*) + E\,exp(FT^*) + G\,exp(HT^*) \tag{2-49}$$

$$T^* = \frac{T}{\varepsilon_{ij}} \tag{2-50}$$

$$\varepsilon_{ij} = \sqrt{\varepsilon_i \varepsilon_j} \tag{2-51}$$

$$\sigma_{ij} = \frac{1}{2}(\sigma_i + \sigma_j) \tag{2-52}$$

where Ω_D is the temperature-dependent collision integral; T_b is the boiling temperature at the standard air pressure; A to H are the empirical constants that can be found in Refs [128,129].

2.5 Heat transfer

Both electrochemical reactions and chemical reactions could considerably influence the temperature field in the cell [100]. Meanwhile, based on Eq. (12)-(14), the reaction rates are intrinsically related to the temperature. Therefore, it is important to simulate the heat transport in channels and porous media. The energy conservation equation is expressed as [130]:

$$\rho C_p \boldsymbol{u} \nabla T + \nabla \cdot \left(-k_{eff} \nabla T\right) = Q_H \tag{2-53}$$

$$C_p = \sum_i y_i \cdot C_{p,i} \tag{2-54}$$

$$k_{eff} = \varepsilon \cdot k_g + (1 - \varepsilon) \cdot k_s \tag{2-55}$$

$$k_g = \sum_i y_i \cdot k_i \tag{2-56}$$

where C_p is the specific heat capacity (J kg^{-1} K^{-1}); k_{eff} is the effective thermal conductivity (W m^{-1} K^{-1}); k_s represent the solid phase heat conductivity, k_i denotes the fluid species thermal conductivity, Q_H represents the heat source or sink [131,132]. The source terms of reversible heat, irreversible heat and ohmic heat could be determined as listed [133]:

$$Q_{re} = (-T\Delta S) \cdot \frac{i}{nF} \tag{2-57}$$

$$Q_{ir} = \eta_{act} \cdot i \tag{2-58}$$

$$Q_{ohmic} = -(i \cdot \nabla \varphi) \tag{2-59}$$

where ΔS represents the change of entropy of the electrochemical reaction (J mol^{-1} K^{-1}). The heat transfer is simplified in a local-equilibrium model as it accounts for the PCEC operating under steady-state conditions. Essentially, this model implies that the difference between the local fluid and the solid material is relatively smaller during steady operation. The authors acknowledge that determining the effective thermal conductivity through the parallel model slightly deviates from the premise of a random packing sphere system. Thus, a future comparative analysis can be conducted to illustrate how the methods for calculating effective thermal conductivity impact the thermal properties of PCECs.

2.6 Mechanical model

To spatially solve the stress field within the PCEC, the equations describing the mechanical behaviour of the system must be implemented. These equations can reflect the various physical phenomena that contribute to the stress and strain within the PCEC. In this mechanical model, the total stain ($\boldsymbol{\varepsilon_{tot}}$) can be decomposed into four terms [134]:

$$\boldsymbol{\varepsilon_{tot}} = \boldsymbol{\varepsilon_{ela}} + \boldsymbol{\varepsilon_{therm}} + \boldsymbol{\varepsilon_{chem}} + \boldsymbol{\varepsilon_0} \tag{2-60}$$

where $\boldsymbol{\varepsilon_0}$, $\boldsymbol{\varepsilon_{ela}}$, $\boldsymbol{\varepsilon_{therm}}$, and $\boldsymbol{\varepsilon_{chem}}$ respectively denote the initial strain, elastic strain, thermal strain, and chemically induced strain. It is assumed that the coefficient of thermal expansion (CTE) is invariable to the change of temperature during the PCEC operation [135]. Therefore, the thermal strain can be expressed as follows:

$$\boldsymbol{\varepsilon_{therm}} = \alpha(T - T_{ref})\boldsymbol{I} \tag{2-61}$$

where α is the CTE of the material (K^{-1}), **I** is a unit tensor, T_{ref} represents the reference stress-free temperature. In this work, the reduction temperature is determined as the stress-free temperature. As mentioned before, when the hydration reaction occurs, the formation of protonic defects will lead to the lattice expansion in the material [48]. As a result, the chemically induced strain within the PCECs can describe how the strain is influenced by changes in the concentration of protonic defects [106]:

$$\boldsymbol{\varepsilon_{chem}} = \beta_{OH_O^{\cdot}}([OH_O^{\cdot}] - [OH_O^{\cdot}]_{ref})\boldsymbol{I} \tag{2-62}$$

where $[OH_O^{\cdot}]$ and $[OH_O^{\cdot}]_{ref}$ are respectively the local concentration of protonic defect (mol m^{-3}) and the reference concentration of protonic defect. $\beta_{OH_O^{\cdot}}$ represents the coefficient of chemical expansion (CCE, m^3 mol^{-1}), which is used to quantitatively describe the relationship between lattice expansion and the concentration of protonic defect. $\beta_{OH_O^{\cdot}}$ can be calculated as the product of the molar volume of electrolyte material (V_m) and the linear lattice CCE ($\beta^L_{OH_O^{\cdot}}$). Noteworthy, the CCE is also assumed to be temperature invariant during PCEC operation. Furthermore, the relationship between stress ($\boldsymbol{\sigma}$) and strain can be described as following according to Hooke's law [134]:

$$\boldsymbol{\sigma} = \boldsymbol{D}(\boldsymbol{\varepsilon_{tot}} - \boldsymbol{\varepsilon_{therm}} - \boldsymbol{\varepsilon_{chem}}) \tag{2-63}$$

where $\boldsymbol{D}$ stands for the elastic matrix. In addition, to solve the mechanical model, the mechanical properties of materials used in PCECs should be given. According to the composite sphere method, the bulk modulus (K_{com}, Pa) and shear modulus (G_{com}, Pa) of dense composite material can be calculated as [134,136]:

$$K_{com} = K_{el} + \frac{\phi_{ed}}{\frac{1}{K_{ed} - K_{el}} + \frac{3\phi_{el}}{3K_{el}} + 4G_{el}} \tag{2-64}$$

$$G_{com} = G_{el} + \frac{\phi_{ed}}{\frac{1}{G_{ed} - G_{el}} + \frac{6\phi_{el}(K_{el} + 2G_{el})}{5\left(G_{el}(3K_{el} + 4G_{el})\right)}} \tag{2-65}$$

where K_{el} and K_{ed} are the bulk modulus (Pa) of electrolyte material and electrode material, respectively. G_{el} and G_{ed} are the shear modulus of electrolyte material and electrode material, respectively. ϕ_{el} and ϕ_{ed} are the volume fraction of electrolyte material and electrode material, respectively. While the bulk modulus (K_i) and shear modulus (G_i) of an individual material (electrolyte or electrode) can be represented as the functions of Young's modulus (E_i, Pa) and Poisson ratio (ν_i) [136]:

$$K_i = \frac{E_i}{3(1 - 2\nu_i)} \tag{2-66}$$

$$G_i = \frac{E_i}{2(1 + \nu_i)} \tag{2-67}$$

In addition, in the porous media, the effective Young's modulus and effective shear modulus can be evaluated as [134]:

$$E_{eff} = \frac{E_0(1 - \varepsilon)^2}{1 + (2 - 3\nu_0)\varepsilon} \tag{2-68}$$

$$G_{eff} = \frac{G_0(1 - \varepsilon)^2}{1 + \frac{11 - 19\nu_0}{(4 + 4\nu_0)\varepsilon}} \tag{2-69}$$

where ε is the porosity of the material, E_0, ν_0, and G_0 are Young's modulus, Poisson ratio, and shear modulus of the dense material, respectively. The effective CTE of dense composite material can be formulated as [137]:

$$\alpha_{eff} = \alpha_{ed}\phi_{ed} + \frac{4G_{el}}{K_{el}} \frac{K_{el} - K_{ed}}{4G_{el} + 3K_{ed}} (\alpha_{el} - \alpha_{ed})\phi_{ed} \tag{2-70}$$

2.7 Design of Experiments (DOE) method

DOE is a method that systematically varies multiple factors between different levels (e.g., two levels in this research) to create combinations that can be tested and analysed to determine the main and interactive effects on the response variables of interest. This method produces structured and statistically informed outcomes, unlike the traditional one-factor-at-a-time (OFAT) approach, which could require many experiments to achieve the desired results. DOE can provide insight into how different factors affect the response variables with a small number of cases. This is because DOE uses a structured experimental design that ensures that each factor is varied systematically across the different treatments, which allows researchers to isolate the effects of each factor. In particular, in this work, a well-known Yates technique is implemented to perform a factorial design [138]. In addition to applying a systematic factorial design, DOE also employs analysis of variance (a statistical technique) to analyse the data. Then, it can quantify the impacts of different factors and identify the important factors. Thus, by carefully conducting a factorial design in DOE and performing statistical analysis of the results, valuable insights can be gained even with a limited number of cases. To gain a better understanding and learn about the DOE method, Refs [139,140] are highly recommended as they are excellent textbooks on the subject. Furthermore, additional literature utilizing the DOE method can be found in Refs [141,142]. These resources provide valuable insights and guidance on how to effectively conduct DOE and analyse data using the DOE method.

2.8 Deep neural network (DNN)

A deep neural network (DNN) is a type of machine learning algorithm that is modelled after the structure and function of the human brain. DNN contains multiple layers of neurons to process and transmit information [143]. The first layer is the input layer, which receives the data. The last layer is the output layer, which produces the desired output. The hidden layers in

between the input and output layers perform various computations on the data [144]. Although training DNN needs a large amount of data, it has a great capability to learn the complex relationships between input and output data. Furthermore, since solving the Multiphysics model is a time-consuming process, using DNN to develop a surrogate model of the Multiphysics model is capable of enhancing the computational efficiency [73]. Besides, the R-squared (R^2) and the Root-mean-square-error (RMSE) are used as the metrics for evaluating the performance of the DNN model [145]. R^2 is estimated by subtracting the ratio of the sum of squared residuals to the total sum of squares from one. RMSE is calculated by taking the square root of the mean of the squared differences between the predicted value and the actual value.

$$R^2 = 1 - \frac{SS_{res}}{SS_{tot}} = 1 - \frac{\sum(y_{real} - y_{pred})^2}{\sum(y_{real} - y_{mean})^2} \tag{2-71}$$

$$RMSE = \sqrt{\frac{1}{N}\sum(y_{real} - y_{pred})^2} \tag{2-72}$$

2.9 Global sensitivity analysis (GSA)

Before solving the multi-objective optimization problems, the trained DNN model is used to assist the global sensitivity analysis (GSA), which aims to identify the most influential input parameters that affect the output. The sensitivity of the DNN model output to changes in the input can be evaluated by GSA. Sobol sensitivity analysis (SSA), a variance-decomposition-based method, is adopted [146]. Assuming the output of a model can be written as Eq.(2-73), the SSA will decompose it into Eq.(2-74) [147]. In addition, the correspondingly decomposed variance of Y can be expressed as Eq.(2-75). In such a way, Sobol sensitivity indices (SI) can be determined as shown in Eqs.(2-77)-(2-79). The first-order SI indicates the contribution of an input parameter to the output variance without the interaction effects of other parameters.

The second-order SI indicates the contribution of interactions between two input parameters to the model output variance. The total contribution of an input parameter to the output can be represented by the total SI.

$$Y = f(X) = f(X_1, X_2, \dots, X_k) \tag{2-73}$$

$$Y = f_0 + \sum_{i=1}^{k} f_i(X_i) + \sum_{i=1}^{k} \sum_{j=i+1}^{k} f_{i,j}(X_i, X_j) + \cdots + f_{1,2,\dots,k}(X_1, X_2, \dots, X_k) \tag{2-74}$$

$$V(Y) = \sum_{i=1}^{k} V_i + \sum_{i=1}^{k} \sum_{j=i+1}^{k} V_{i,j} + \cdots + V_{1,2,\dots,k} \tag{2-75}$$

$$First - order: S_i = \frac{V_i}{V} \tag{2-76}$$

$$Second - order: S_{i,j} = \frac{V_{i,j}}{V} \tag{2-77}$$

$$Total: S_{tot,i} = \frac{V_i + \sum_{j=i+1}^{k} V_{i,j} + \cdots + V_{1,2,\dots,k}}{V} \tag{2-78}$$

2.10 Modelling assumptions

The main assumptions adopted in this work are listed as follows:

1) All the gas species involved in the PCEC operation are considered ideal and incompressible gases.
2) The porous electrodes are considered uniformly dispersed particles of both electrolyte and electrode materials.
3) The particle sizes of electrolyte and electrode materials are assumed to be the same.
4) The electrochemical reaction sites are uniformly distributed within the porous electrodes.
5) The electrolyte contains mobile charge carriers in the form of protonic defects, oxygen vacancies, and polarons.

6) All chemically induced strains are assumed to be caused by the change in the concentration of protonic defects.

7) During PCEC operation, both CTE and CCE are supposed to remain constant to temperature changes.

2.11 Model validations and boundary conditions

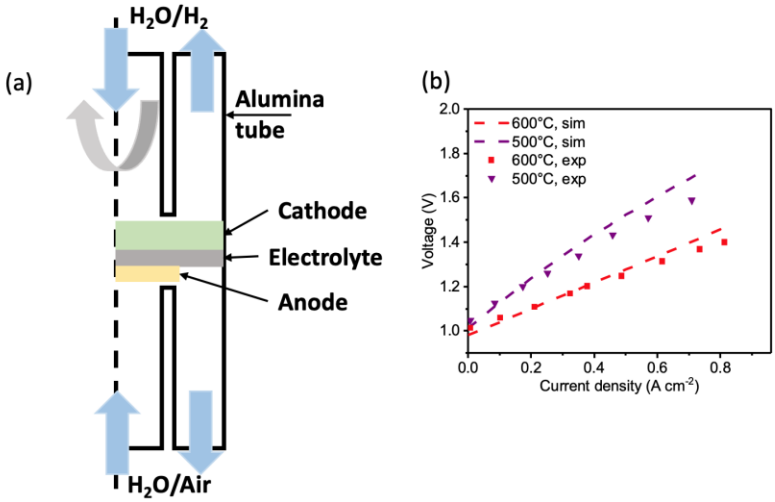

Figure 2.1 (a) the geometry of the 2D axisymmetric model for the button-cell PCEC; (b) the model validation.

The model validation is conducted based on a button-cell PCEC. Therefore, as shown in Figure 2.1 (a), a 2D axisymmetric model is first developed for a button-cell PCEC. The geometry information of the 2D axisymmetric model and boundary conditions used for the model validation are gathered in Table 2-1. In Figure 2.1 (b), the simulation data show a good agreement with the experimental data [148]. After validation, the PCEC geometry can be changed to planar or tubular as needed. In Table 2-1,the designation "Open boundary" signifies a boundary within the PCEC model where fluid variables, including velocity and pressure, are handled to freely enter or exit the boundary. In other words, the flow characteristics at this boundary are determined without enforcing specific constraints.

Table 2-1 Geometry information and boundary conditions of 2D axisymmetric model.

Descriptions	**Value**	**Unit**
Cathode thickness	490	μm
Anode thickness	20	μm
Electrolyte thickness	10	μm
$x_{an,inlet}$	Humidified air (10% H_2O)	
$x_{ca,inlet}$	97% H_2/3% H_2O	
$v_{an,inlet}$	300	SCCM
$v_{ca,inlet}$	64	SCCM
i_{op}	0-0.8	A cm^{-2}
P_{op}	1	atm
T_{op}	500-600	°C
Anode inlet	$x_{an,inlet}, v_{an,inlet}, T_{op}$	
Cathode inlet	$x_{ca,inlet}, v_{ca,inlet}, T_{op}$	
Anode upper-face	$i = i_{op}$	
Cathode upper-face	$\varphi_e = 0$	
Anode outlet	Open boundary	
Cathode outlet	Open boundary	
Other boundaries	Insulation/Wall	

Chapter 3 Effects of various operating parameters in a protonic ceramic electrolysis cell with considering current leakage

3.1 Introduction

To provide a comprehensive understanding of the main effects of various operating parameters and interactions between them on the electrochemical performance and faradaic efficiency of PCEC, a 2D numerical model is developed. The heat transfer and the transport processes of different charge carriers in the PCEC electrolyte are fully considered. The framework of this study is shown in Figure 3.1. More importantly, to explore the effects of different operating parameters on the PCEC performance, two methods are applied in this study: 1) the One-Factor-At-a-Time (OFAT) method; 2) the Design of Experiments (DOE). The OFAT method, where one factor or parameter is varied at a time while keeping all other factors constant, aims to study the effect of each factor on the outcome variable independently of other factors [149]. Although the OFAT method is easy to implement and can help researchers understand the effect of a factor, it cannot account for interactions between different factors, which may pose a significant impact on the outcome. The second method, DOE, can make up for the shortcomings of the OFAT, which is to consider the interactions between factors [140]. In addition, DOE can give the impact level of different operating parameters. Hence, the most important operating parameters can be identified. The present work combines the advantages of OFAT and DOE methods, thereby providing a more accurate understanding of the effects of six different operating parameters on the PCEC. Furthermore, the framework proposed in this study can be extended to other theoretical modelling of PCEC.

3.2 Modelling Methodology

3.2.1 Model geometry and boundary conditions

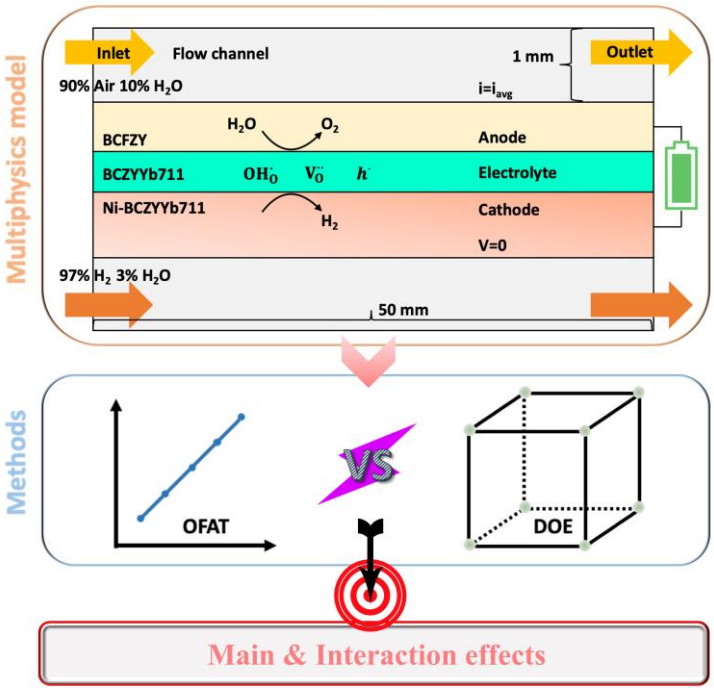

Figure 3.1 Schematics of the framework.

As illustrated in Figure 3.1, a 2D model is developed for a planar PCEC (active area: 5 × 5 cm^2). After the construction of the model, both OFAT and DOE approaches are implemented to investigate the effects of different operating parameters and the interactions between each other. The geometry information, model parameters, and boundary conditions of this model are gathered in Table 3-1. Mesh independence of the model is achieved.

Table 3-1 Geometry information, model parameters, and boundary conditions of planar PCEC.

Descriptions	Value/expression	Unit
Anode thickness	30	μm
Cathode thickness	400	μm
Electrolyte thickness	20	μm
Gas channel height (or depth)	1	mm
Out-of-Plane thickness	50	mm

Cell length	50	mm
ε_{an}	0.4	1
ε_{ca}	0.4	1
τ_{an}	3	1
τ_{ca}	3	1
P_{op}	1	atm
T_{op}	600	°C
$r_{particle}$	0.5	μm
$\phi_{an/ca}$	0.6	1
ζ	1.5	1
β_a	0.5	1
β_c	0.3	1
$E_{act,a}$	130000	J mol^{-1}
$E_{act,c}$	120000	J mol^{-1}
$x_{an,inlet}$	Air/10% H_2O	
$x_{ca,inlet}$	H_2/5% H_2O	
$v_{an,inlet}$	1.03×10^{-4}	kg s^{-1}
$v_{ca,inlet}$	1.03×10^{-5}	kg s^{-1}
i_{op}	0.1-0.9	A cm^{-2}
P_{op}	1	atm
T_{op}	500-600	°C
Anode inlet	$x_{an,inlet}, v_{an,inlet}, T_{op}$	
Cathode inlet	$x_{ca,inlet}, v_{ca,inlet}, T_{op}$	
Anode upper-face	$i = i_{op}$	
Cathode upper-face	$\varphi_e = 0$	
Anode outlet	Open boundary	
Cathode outlet	Open boundary	

Other boundaries	Insulation/Wall

3.2.2 DOE

As listed in Table 3-2, a full 2^4 factorial design is implemented in this study. Four factors are chosen: the cathode inlet steam fraction (xc_in, denoted as A), the anode inlet steam fraction (xa_in, denoted as B), the cathode inlet flow rate (vc_in, denoted as C) and the anode inlet flow rate (va_in, denoted as D). Two levels, i.e., high level (coded as 1) and low level (coded as 0), are assigned to each factor. The high level and low level of each parameter are summarized in Table 3-3. Hence, a total of 16 treatments are included. Three replications are performed to ensure the precision of the data. Additionally, three important responses are recorded, namely, applied voltage, temperature gradient and FE.

Table 3-2 The list of a 2^4 factorial design.

ID	A, xc_in	B, xa_in	C, vc_in	D, va_in	Treatment combination
1	0	0	0	0	(1)
2	1	0	0	0	A
3	0	1	0	0	B
4	1	1	0	0	AB
5	0	0	1	0	C
6	1	0	1	0	AC
7	0	1	1	0	BC
8	1	1	1	0	ABC
9	0	0	0	1	D
10	1	0	0	1	AD
11	0	1	0	1	BD
12	1	1	0	1	ABD
13	0	0	1	1	CD
14	1	0	1	1	ACD

15	0	1	1	1	BCD
16	1	1	1	1	ABCD

Table 3-3 The high-level and low-level of each parameter.

Parameters (unit)	High-level	Low-level
A, xc_in (1)	0.05	0.45
B, xa_in (1)	0.1	0.5
C, vc_in (kg s^{-1})	8.38×10^{-7}	1.47×10^{-6}
D, va_in (kg s^{-1})	6.19×10^{-5}	1.24×10^{-4}

3.3 Results and discussions

3.3.1 OFAT

3.3.1.1 Effects of current density and operating temperature

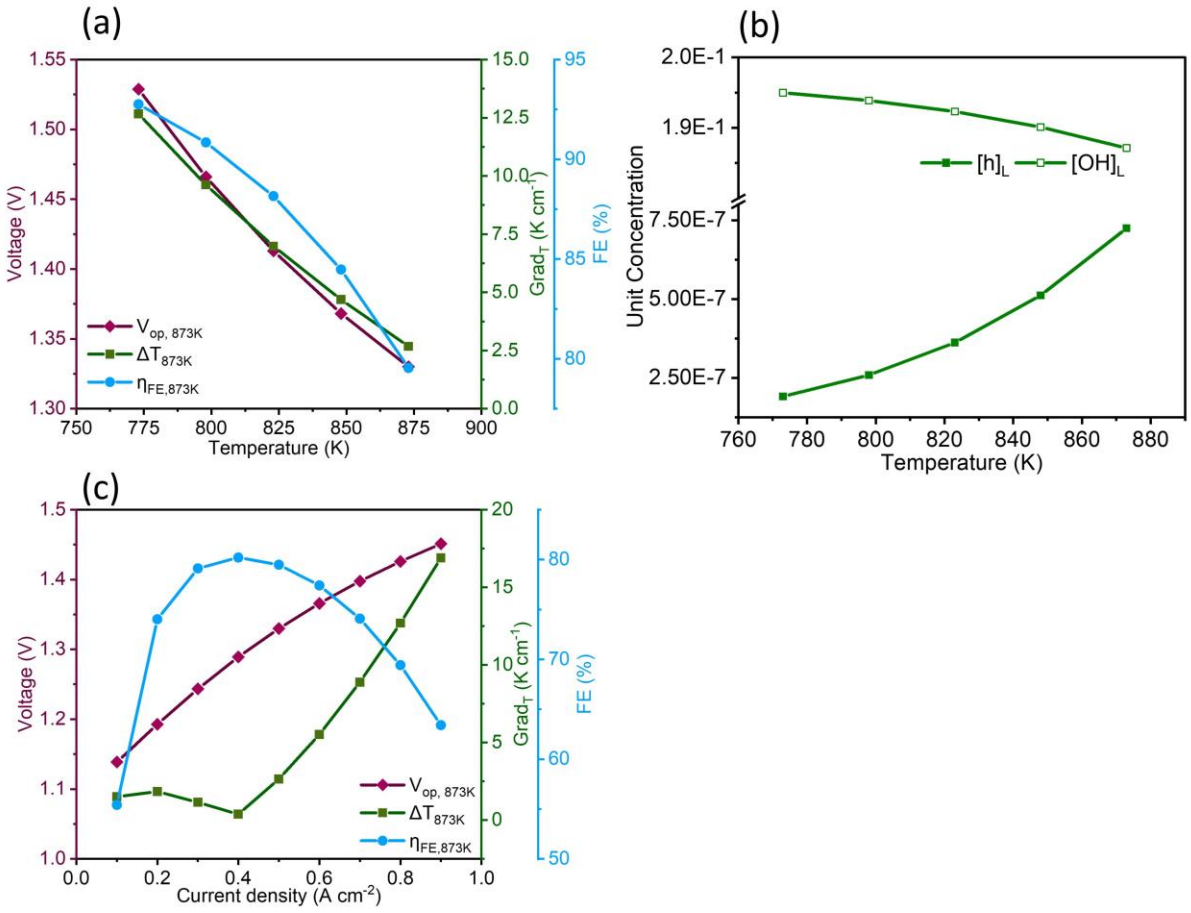

Figure 3.2 Effects of working temperature on (a) the voltage, FE and temperature gradient, on (b) unit concentration of different charge carriers; effects of current density on (c) the voltage,

FE and temperature gradient.

In Figure 3.2 (a), with the increase of working temperature, both applied voltage and temperature gradient decrease monotonically. The FE also shows the same trend as the change in working temperature. This can be explained by the results exhibited in Figure 3.2 (b), where $[h^{\cdot}]_L$ is nearly tripled and $[OH^{\cdot}]_L$ decreases by around 4% as the working temperature increases from 773 K to 873 K. $[h]_L$ represents the concentration of electronic hole in lattice unit. Electronic holes can react with electrons, which is why current leakage occurs. The molar flux of the electronic hole is proportional to the $[h]_L$. Thus, the sensitivity of $[h]_L$ to working temperature (Figure 3.2 (b)) is equivalent to the sensitivity of leakage current to working temperature, which is in turn equivalent to the sensitivity of FE to working temperature. Additionally, as shown in Figure 3.2 (b), the $[h]_L$ increases with increasing working temperature, indicating that the leakage current increases as well. Therefore, the FE will decrease with increasing working temperature at 0.5 A cm^{-2}. In Figure 3.2 (c), as expected, the applied voltage increases gradually with the increase of current density. The FE increases sharply with the initial increase of current density, which is consistent with the previously reported data in Ref. [62]. The peak FE of 82% is obtained at a current density of 0.4 A cm^{-2}. However, the FE of PCEC decreases with increasing current density and is approximately 62.5% when the current density is 0.9 A cm^{-2}. This observation of the present model is contrary to the data reported in Ref. [62] because the heat transfer within the PCEC is accounted for in this work. Noteworthy, in this work, the temperature gradient within the cell is defined as the maximum temperature minus the minimum temperature, then divided by the length of the whole cell. Hence, the temperature gradient is consistently positive. Before reaching the thermal-neutral voltage (TNV), the heat adsorbed by the steam electrolysis reaction is greater than the ohmic heat and the polarization heat. Therefore, the PCEC is in endothermic mode when the voltage is < TNV. At 0 A cm^{-2}, the temperature gradient should be zero (no heat

generated or adsorbed). At 0.1 A cm^{-2}, the temperature gradient increases to 1.4 K cm^{-1} (endothermic). At 0.4 A cm^{-2}, the temperature gradient decreases to 0 K cm^{-1} (TNV=1.28 V). Hence, as the current density increases, the temperature gradient initially increases then decreases before reaching the TNV. Additionally, with a further increase in the current density, the generated ohmic heat and polarization heat surpass the electrolytic adsorbed heat, making PCEC in the exothermic operation mode. Therefore, the temperature gradient increases again after the current density is higher than 0.4 A cm^{-2}. In addition, this steep increase in temperature gradient can be explained by the calculation of different types of heat. For instance, the electrochemical reaction heat can be calculated based on Eq. 2-58, while the ohmic heat can be calculated based on Eq. 2-60. The $\nabla\varphi$ can be simplified as the product of current density and ohmic resistance. In other words, the electrochemical reaction heat shows a first-order relationship with the current density, while the ohmic heat shows a second-order relationship with the current density. Therefore, as the current density increases, the steeper increase in temperature gradient can be attributed to the increase in the ohmic heat.

3.3.1.2 Effects of inlet flow rate

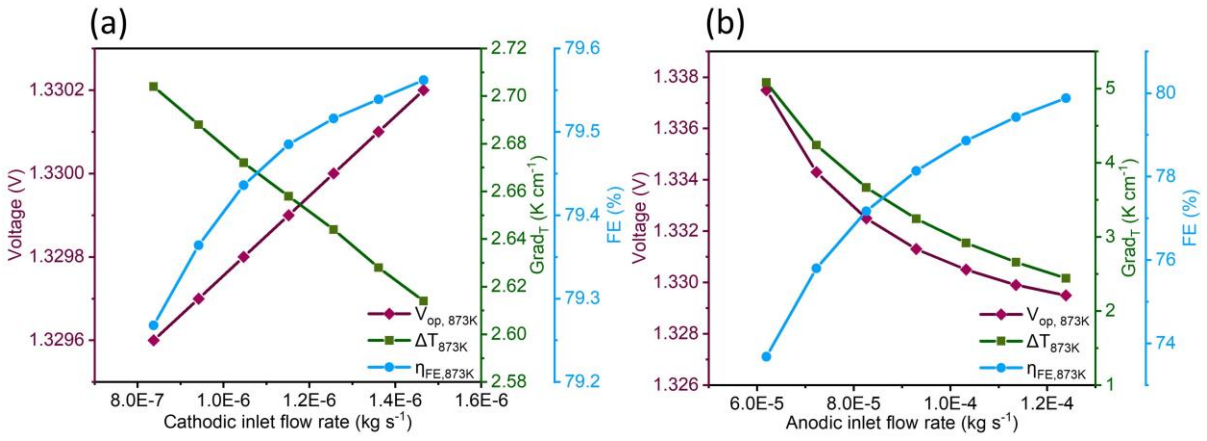

Figure 3.3 Effects of cathode inlet flow rate on (a) the voltage, FE and temperature gradient; effects of anode inlet flow rate on (b) the voltage, FE and temperature gradient.

Since either an increase in the anode inlet flow rate or in the cathodic inlet flow rate can remove the heat from the PCEC, the temperature gradient decreases monotonically as expected (Figure

3.3 (a) and (b)). Correspondingly, the FE increases with increasing inlet flow rate either in the anode or in the cathode. Although the applied voltage increases with the increase of the cathode inlet flow rate, the increase is negligible (< 0.04%) (Figure 3.3 (a)). As the anode inlet flow rate increases, the concentration of reactants within the electrode can be maintained at a higher level, which can reduce the concentration polarization effect and lead to a decrease in applied voltage. However, its effect on the applied voltage is negligible. When the anode inlet flow is doubled, the applied voltage only increases by about 0.6%.

3.3.1.3 Effects of inlet steam fraction

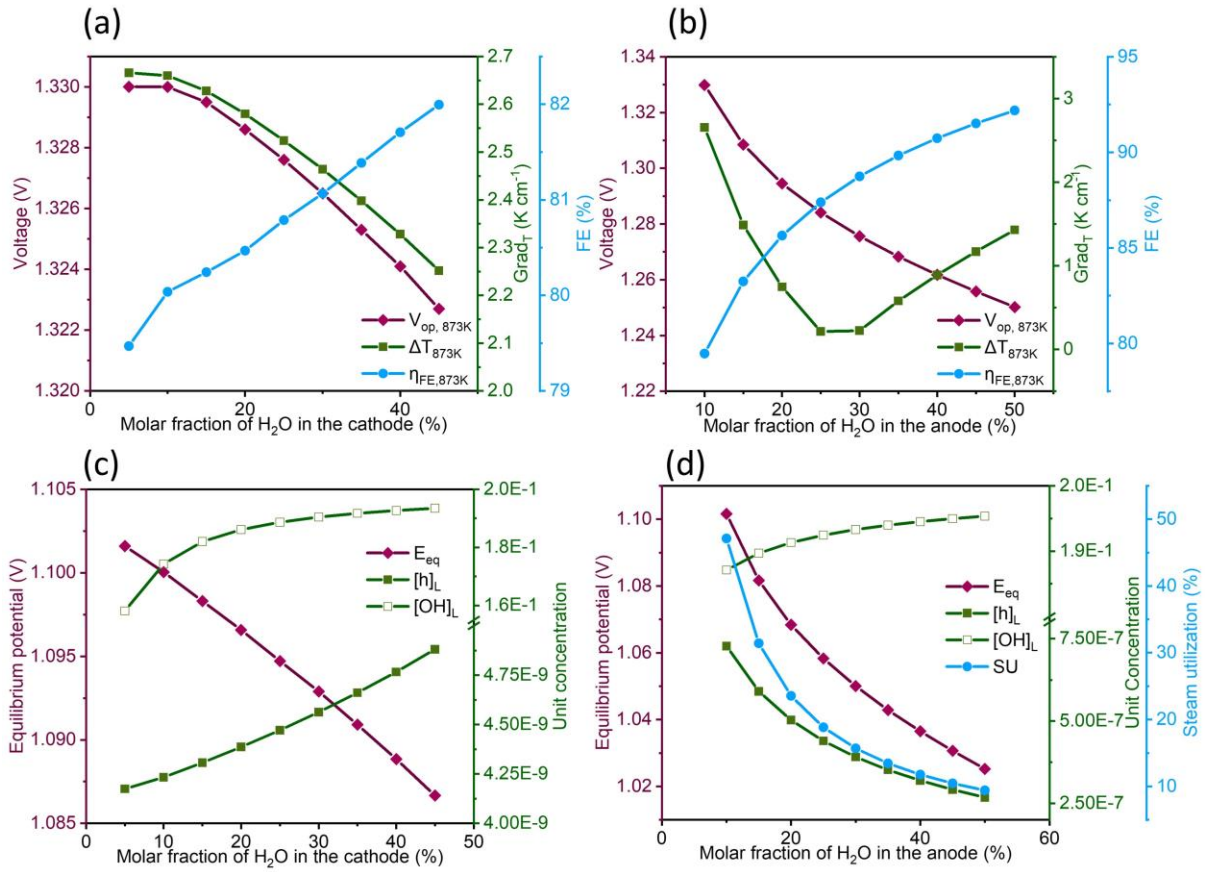

Figure 3.4 Effects of cathode inlet steam fraction on (a) the voltage, FE and temperature gradient, on (c) the equilibrium potential and unit concentration of different charge carriers; effects of anode inlet steam fraction on (b) the voltage, FE and temperature gradient, on (d) the equilibrium potential, the unit concentration of different charge carriers and steam utilization.

With an increase in the cathode inlet steam fraction, the applied voltage decreases continuously (Figure 3.4 (a)). The increased cathode inlet steam fraction leads to a reduction in the partial pressure of H_2, leading to a decrease in the equilibrium potential of PCEC (Figure 3.4 (c)). As the anodic inlet steam fraction increases, the overpotential of PCEC decreases as well. In addition, since the anodic inlet steam fraction increases, the composition of gas phases at the anode side of PCEC varies, which should pose an impact on the mass transfer at the anode side. In addition, the concentration overpotential of PCEC also indicates a decrease with the increasing anodic inlet steam fraction. It is also found that the temperature gradient decreases slightly as the cathode inlet steam fraction increases. Furthermore, the enhanced moist environment in the cathode substantially promotes the formation of proton defects even if the formation of holes is slightly improved as well. Consequently, the FE increases with increasing cathode inlet steam molar fraction. Besides, the applied voltage also decreases with the increase of the anode inlet steam fraction (Figure 3.4 (b)). The increased anode inlet steam fraction can increase the partial pressure of H_2O within the PCEC, resulting in a decrease in the equilibrium potential (Figure 3.4 (d)). In Figure 3.4 (b), when the anode inlet steam fraction increases to 20%, the applied voltage approaches TNV, thereby making the temperature gradient in the cell equal to zero. Subsequently, with a further increase in anode steam fraction, the applied voltage becomes smaller than TNV, making the endothermic operation of PCEC. Furthermore, the increased anode inlet steam fraction can strongly suppress the formation of holes since the partial pressure of oxygen in the anode is reduced (Figure 3.4 (d)). Considering both temperature and defect concentration effects, the FE can be enhanced by increasing the anode steam molar fraction. Nevertheless, it is worth noting that although increasing the anode inlet steam fraction is an effective way to reduce the temperature gradient and improve FE, the steam utilization is remarkably reduced (Figure 3.4 (d)). This is detrimental to the overall energy efficiency of PCEC. Moreover, if the anode inlet steam fraction is increased, it will result in

the dilution of produced hydrogen. This means that a separation process must be implemented to obtain pure hydrogen, and this additional step can decrease the overall efficiency of the system and increase its cost. Therefore, it is crucial to exercise careful control over the cathode inlet steam fraction from the perspective of the entire PCEC system.

3.3.2 DOE

3.3.2.1 Effects of different treatments on the operating voltage

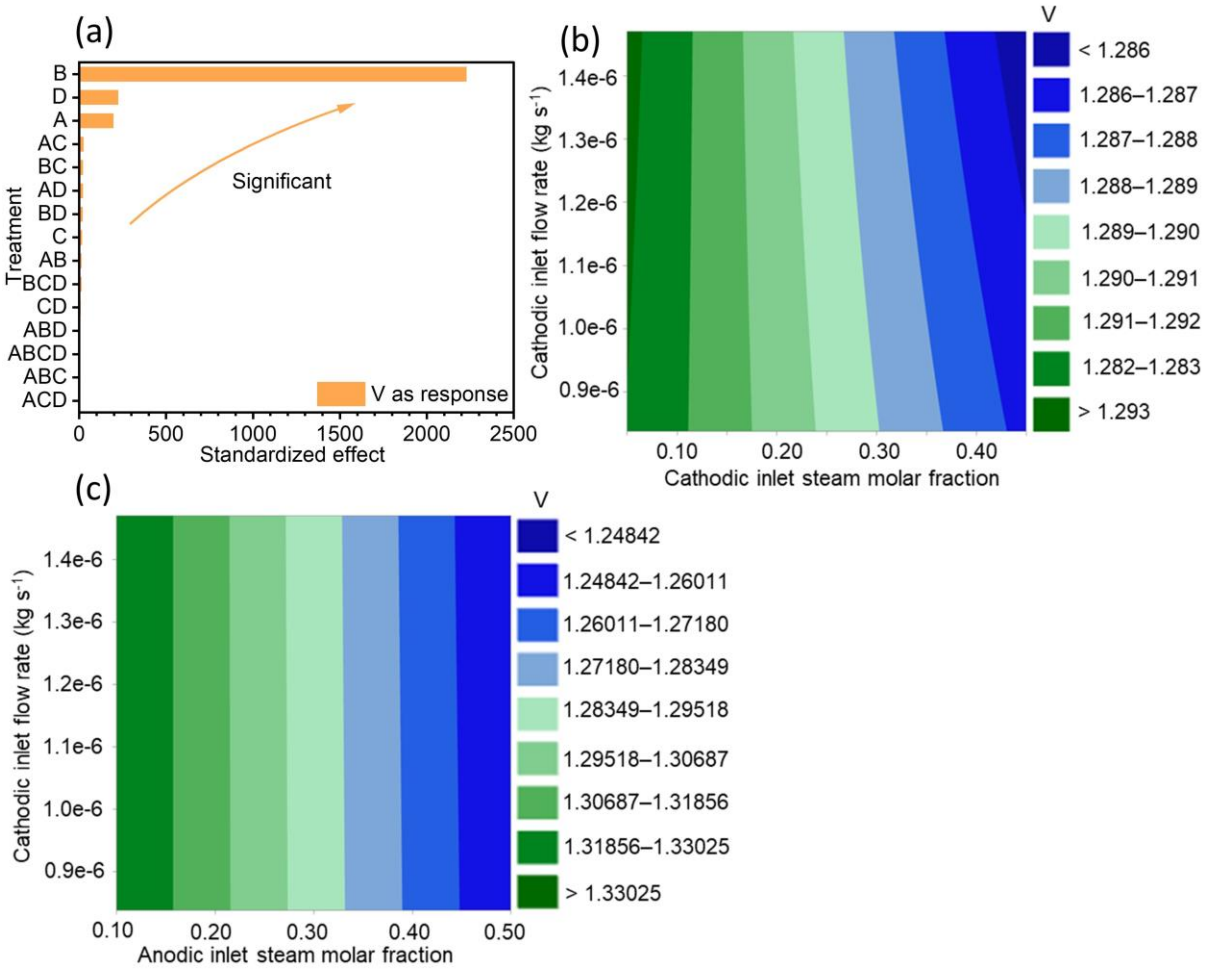

Figure 3.5 When the applied voltage is the response: (a) standardized effects of different parameters' treatments, contour maps of interactions between (b) cathode inlet flow rate and cathode inlet steam fraction, between (c) cathode inlet flow rate and anode inlet steam fraction.

Figure 3.5 (a) shows the order of different parameters based on their importance. The most important factor to the applied voltage is the anode inlet steam fraction. Additionally, the top five important treatments are: B > D > A > AC > BC. Figure 3.5 (b) and (c) demonstrate the

contour map of AC and BC interaction effects, respectively. In Figure 3.5 (b), it can be found that, compared to the main effect of cathode inlet steam fraction, the main effect of cathode inlet flow rate is negligible. Furthermore, the interaction of AC on the applied voltage tends to increase the voltage when the cathode inlet steam fraction is < 0.18, whereas the opposite effect is observed when the cathode inlet steam fraction is > 0.18. This opposite effect becomes more remarkable as the cathode inlet steam fraction increases. In Figure 3.5 (c), the interaction of BC is considerably weaker than that of AC.

The effect of a factor on a response variable is divided into two types: 1) If the response variable increases with the increase of the factor, its effect is positive; 2) If the response variable decreases with the increase of the factor, its effect is negative. Therefore, according to the impact types of different factors, it is possible to qualitatively understand how different factors affect the performance of PCEC. Moreover, under the practical PCEC operation, when the current density is fixed, reducing the applied voltage can be one of the optimization goals for saving electric power. Therefore, understanding the negative impact of different parameters on the applied voltage is also important for planning PCEC operational strategies. As listed in Table 3-4, the anode inlet steam fraction exhibits the most negative effect on the applied voltage. In other words, when reducing the applied voltage is the goal, then increasing the anode inlet steam fraction can be the most effective tactic. The standardized effect of anode inlet flow rate and cathode inlet steam molar fraction is significantly less than that of anode inlet steam molar fraction. Additionally, although the negative of the anode inlet flow rate is not as important as the inlet steam molar fraction, the interaction effects of AC and BC cannot be ignored.

Table 3-4 Order of different treatments.

Cases	**Order of different treatments**
Negative impacts on the applied voltage	B > D > A > AC > BC > AD > C > AB > CD

Negative impacts on the temperature gradient	B > D > C > ABD > BCD > A > ABCD > AC
Positive impacts on the FE	B > D > A > BCD > C > ABD > ABC

3.3.2.2 Effects of different treatments on the temperature gradient

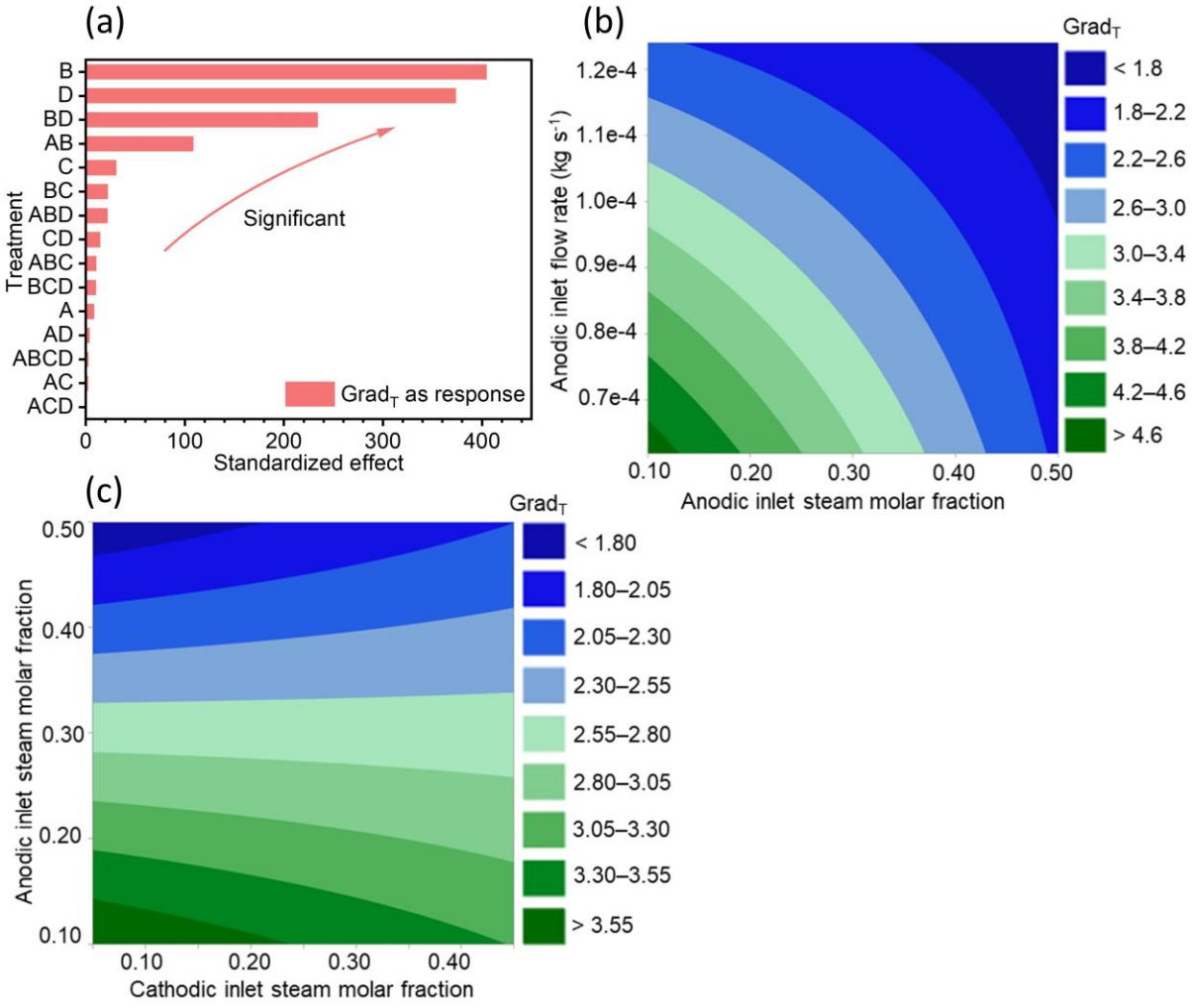

Figure 3.6 When the temperature gradient is the response: (a) standardized effects of different parameters' treatments, contour maps of interactions between (b) anode inlet flow rate and anode inlet steam fraction, between (c) anode steam fraction and cathode inlet steam fraction.

In Figure 3.6 (a), the anode inlet steam molar fraction is still the most significant factor, when the temperature gradient is the response. The top five important treatments are: B > D > BD > AB > C. In Figure 6 (b), it can also demonstrate that the main effects of anode inlet flow rate and anode inlet steam fraction are comparable. While the interaction of BD is more substantial with increasing anode inlet steam fraction. In Figure 3.6 (c), the main effect of the anode inlet steam fraction is more significant than that of the cathode inlet steam fraction. When the anode inlet steam fraction is < 0.3, the interaction of AB on the temperature gradient tends to reduce the temperature gradient. However, the opposite interaction effect is observed when the anode inlet steam fraction is > 0.3. Furthermore, to sustain the robust performance of the PCEC and promote the life span, reducing the temperature gradient can be an optimization target [150]. Table 3-4 shows that the anode inlet steam fraction exhibits the most negative effect on the temperature gradient. Additionally, the second effective parameter is the anode inlet steam fraction.

3.3.2.3 Effects of different treatments on faradaic efficiency

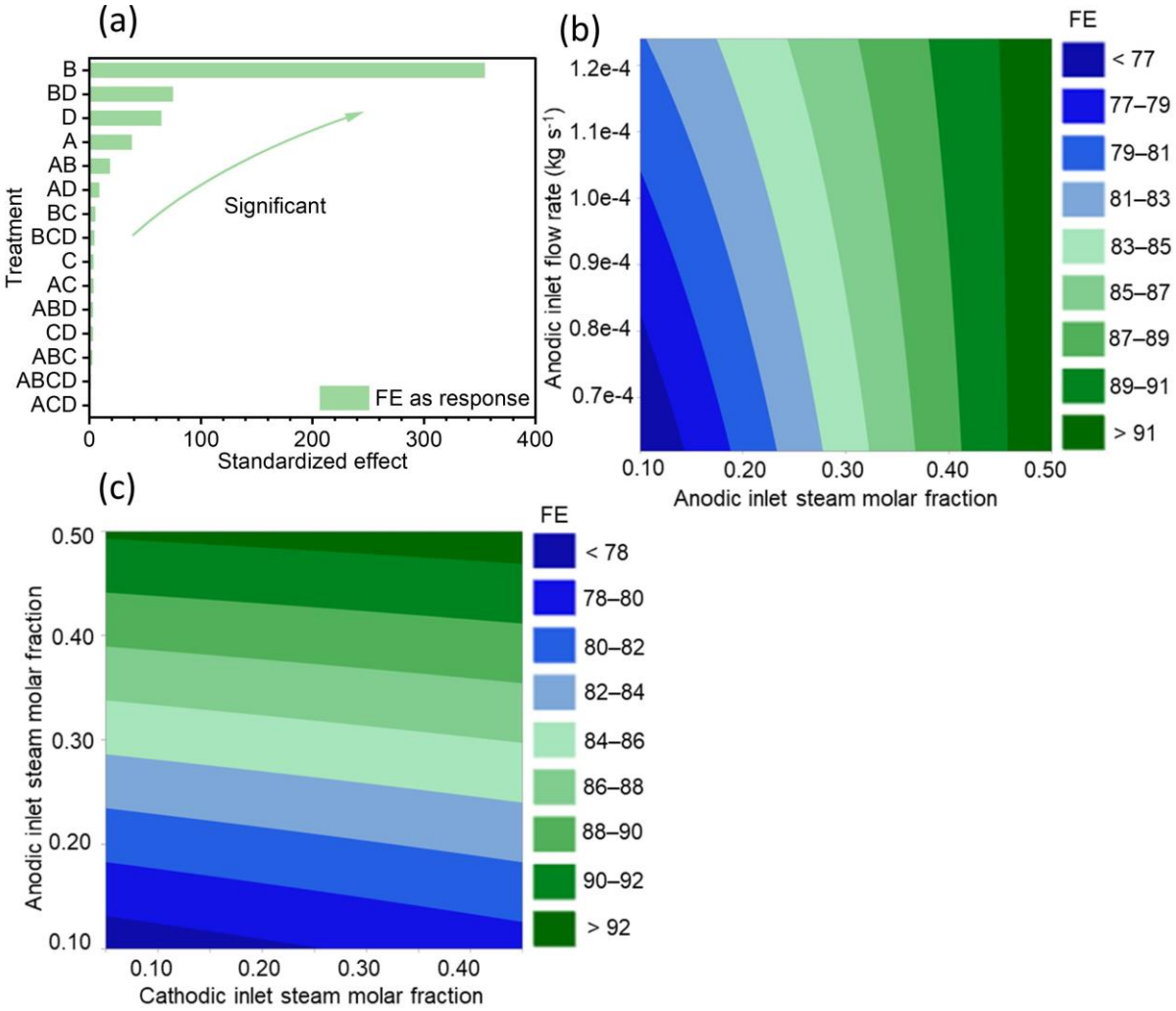

Figure 3.7 When FE is the response: (a) standardized effects of different parameters' treatments, contour maps of interactions between (b) anode inlet flow rate and cathode inlet steam fraction, between (c) anode inlet steam fraction and cathode inlet steam fraction.

Figure 3.7 (a) shows that, when the FE is the response, the most important factor is still the anode inlet steam fraction. The top five important treatments are: B > BD > D > A > AB. It is worth noting that the standardized effects of the anode inlet steam fraction are more than four times that of the second important treatment (interaction of BD). Consequently, it indicates that the effect of the anode inlet steam fraction on the FE is dominant. In Figure 3.7 (b), the interaction of BD is more significant under a low anode inlet steam fraction than that under a high anode inlet steam fraction. In Figure 3.7 (c), the interaction of AB is evidently weaker than that of BD. To enhance the energy efficiency of PCEC, the FE can also be an optimization

goal. The treatments with a positive effect on the FE are summarized in Table 3-4. The anode inlet steam fraction possesses the most important impact on maximizing the FE of PCEC. Furthermore, the second effective parameter is the anode inlet steam fraction.

3.4 Conclusions

A 2D model is developed for a PCEC to investigate the main effects of various operating parameters and interactions between them on the applied voltage, FE and temperature gradients. Furthermore, a framework combining the 2D numerical model, OFAT method and DOE method is constructed.

By using the OFAT method, the peak FE of 82% is obtained at 600 °C and a current density of 0.4 A cm^{-2}. The temperature gradient of the cell decreases with the increase of the inlet flow rate, while the FE shows the opposite trend. The applied voltage and temperature gradient decrease with increasing inlet steam fraction, while FE increases continuously. In addition, by analysing DOE results, the anode inlet steam fraction/flow rate is found to be the most significant factor. The interaction between the cathode inlet steam fraction and the cathode inlet flow rate is found to be important to the operating voltage. The interaction between the anode inlet steam fraction and the anode inlet flow rate is found to be significant to the temperature gradient or FE. In summary, the main contribution of this study is the development of a framework to combine the numerical model with OFAT and DOE. Such a framework can provide deep insights into the effects and interactions of different parameters. Moreover, the significant parameters and interactions can be identified, thereby enhancing the understanding of PCEC.

Chapter 4 An electro-thermo-chemo-mechanical model to account for both thermal and chemical expansions in a protonic ceramic electrolysis cell

4.1 Introduction

Although the mechanical analysis of PCECs is limited, many studies on the mechanical analysis of SOECs have emphasized the importance of understanding how various parameters affect the mechanical behaviour of SOECs, as it can help researchers improve the design of SOECs and optimize their operation [98–101]. With this knowledge, a more rational operation strategy can be developed to play a crucial role in enhancing the durability and stability of the PCEC system. Therefore, it is also essential to perform a mechanical analysis of PCEC, which can provide a comprehensive view of the mechanical behaviour of PCEC by considering both thermal and chemical expansion.

As illustrated in Figure 4.1, the present study proposes a framework. Firstly, the electro-thermo-chemo-mechanical model is developed for PCEC with the consideration of thermal and chemical expansion. Secondly, the DOE method is applied to gain a more comprehensive understanding of how each parameter affects the mechanical behaviour of PCECs. Hence, the main effects of each parameter on PCECs and the interaction effects between parameters can be unveiled by using the DOE method. Adopting this practice in other numerical studies of PCECs can contribute to the advancement of this technology and the realization of a carbon-free society in the future.

4.2 Modelling methodology

4.2.1 Model geometry and boundary conditions

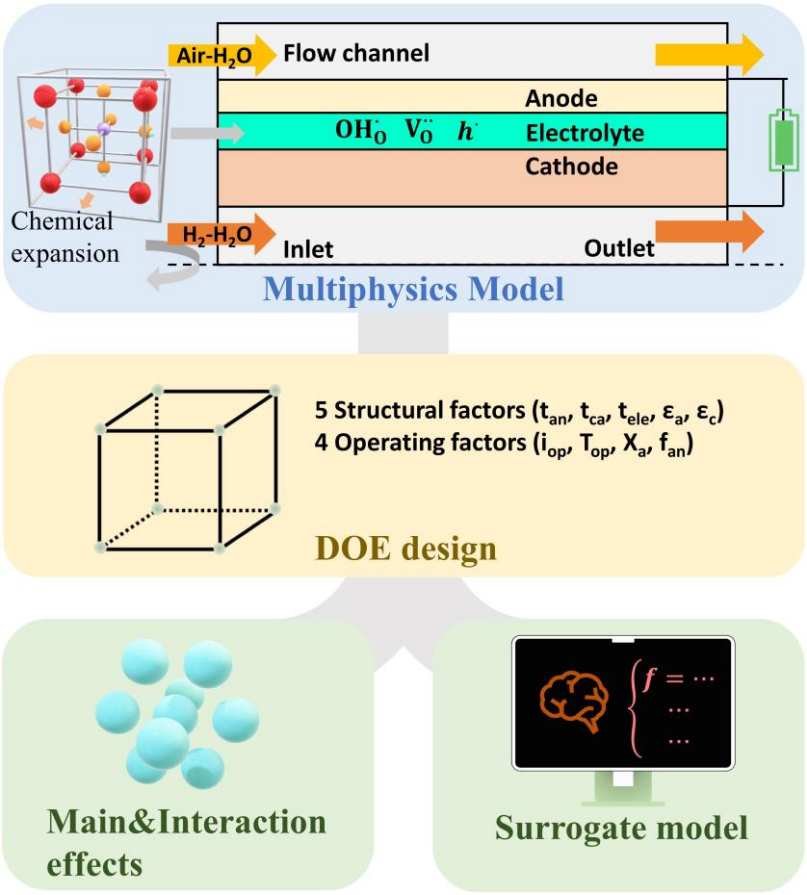

Figure 4.1 Framework of DOE-assisted numerical study of PCEC.

Figure 4.1 illustrates the geometry of the model, which showcases a 2D axisymmetric tubular PCEC. The geometry information, boundary conditions and other parameters adopted in this 2D model are summarized in Table 4-1.

Table 4-1 Geometry information and model parameters of the 2D tubular PCEC model [94,134,167–169].

Parameters	Value	Unit
t_a	30	μm
t_c	400	μm
t_{ele}	20	μm
l_{cell}	3	cm

t_{cha}	3	mm
$\beta_{OH_O^{\cdot}}$	9.75×10^{-7}	$m^3\ mol^{-1}$
V_m	5.13×10^{-5}	$m^3\ mol^{-1}$
$\beta^L_{OH_O^{\cdot}}$	0.019	1
T_{ref}	700	°C
E_{ele}	165	GPa
E_{ca}	171	GPa
E_{an}	140	GPa
ν_{ele}	0.3	1
ν_{ca}	0.31	1
ν_{an}	0.3	1
$x_{an,inlet}$	Air/10% H_2O	
$x_{ca,inlet}$	H_2/3% H_2O	
$v_{an,inlet}$	4.15×10^{-6}	$kg\ s^{-1}$
$v_{ca,inlet}$	6.93×10^{-8}	$kg\ s^{-1}$
i_{op}	0.4-0.7	$A\ cm^{-2}$
P_{op}	1	atm
T_{op}	500-600	°C
Anode inlet	$x_{an,inlet}, v_{an,inlet}, T_{op}$	
Cathode inlet	$x_{ca,inlet}, v_{ca,inlet}, T_{op}$	
Anode upper-face	$i = i_{op}$	
Cathode upper-face	$\varphi_e = 0$	
Anode outlet	Open boundary	
Cathode outlet	Open boundary	
Other boundaries	Insulation/Wall	

4.2.2 DOE

In this study, a series of numerical investigations on PCECs are systematically designed using the DOE approach. A 1/16 2^9-factorial design is performed. The study focuses on nine parameters, comprising five structural parameters and four operating parameters, which are chosen as the variables of interest: cathode thickness (t_c, represented by A), anode thickness (t_a, represented by B), electrolyte thickness (t_{ele}, represented by C), operating current density (I_{op}, represented by D), operating temperature (T_{op}, represented by E), anode steam molar fraction (X_a, represented by F), anode inlet flow rate (f_{an}, represented by G), cathode porosity (ε_a, represented by H) and anode porosity (ε_c, represented by J). Each of the nine selected parameters is assigned two levels, a high level (encoded as 1) and a low level (encoded as -1), resulting in a total of 32 treatments. To ensure the accuracy of the data, each treatment is calculated three times. Table 4-2 illustrates all the treatments considered in the factorial design. The high level and low level of each variable are listed in Table 4-3.

Table 4-2 Treatments of factorial design.

ID	A, t_c	B, t_a	C, t_{ele}	D, I_{op}	E, T_{op}	F, X_a	G, f_{an}	H, ε_c	J, ε_a
1	-1	1	-1	-1	-1	-1	1	-1	-1
2	-1	-1	1	1	-1	1	1	-1	-1
3	1	-1	-1	-1	-1	1	-1	-1	-1
4	1	1	1	-1	-1	1	1	1	-1
5	-1	-1	-1	-1	1	-1	-1	-1	-1
6	-1	-1	1	-1	-1	-1	-1	1	-1
7	1	1	1	1	-1	-1	-1	-1	-1
8	-1	-1	-1	-1	-1	1	1	1	1
9	1	-1	-1	1	1	1	-1	-1	1
10	1	-1	1	1	1	-1	1	-1	-1
11	-1	-1	-1	1	-1	-1	-1	-1	1

12	1	1	1	-1	1	-1	-1	-1	1
13	-1	1	-1	1	1	-1	1	-1	1
14	1	-1	-1	-1	1	-1	1	1	1
15	-1	1	1	-1	-1	1	-1	-1	1
16	1	-1	1	1	-1	1	-1	1	1
17	1	1	-1	1	1	-1	-1	1	-1
18	-1	1	1	1	-1	-1	1	1	1
19	1	-1	1	-1	1	1	-1	1	-1
20	1	-1	1	-1	-1	-1	1	-1	1
21	-1	-1	1	1	1	-1	-1	1	1
22	1	1	1	1	1	1	1	1	1
23	1	1	-1	-1	1	1	1	-1	-1
24	-1	1	1	1	1	1	-1	-1	-1
25	1	1	-1	1	-1	1	1	-1	1
26	1	1	-1	-1	-1	-1	-1	1	1
27	-1	-1	-1	1	1	1	1	1	-1
28	1	-1	-1	1	-1	-1	1	1	-1
29	-1	1	-1	-1	1	1	-1	1	1
30	-1	1	1	-1	1	-1	1	1	-1
31	-1	1	-1	1	-1	1	-1	1	-1
32	-1	-1	1	-1	1	1	1	-1	1

Table 4-3 The high level and low level of each parameter.

Parameters (unit)	**High level**	**Low level**
A, t_c (μm)	400	500
B, t_a (μm)	40	30
C, t_{ele} (μm)	30	20
D, I_{op} (A cm^{-2})	0.6	0.4
E, T_{op} (°C)	600	500

F (1)	0.4	0.1
G ($\times 10^{-6}$ kg s^{-1})	6.23	4.15
H (1)	0.6	0.4
J (1)	0.6	0.4

4.3 Results and discussions

4.3.1 Parametric studies

4.3.1.1 Effects of current density

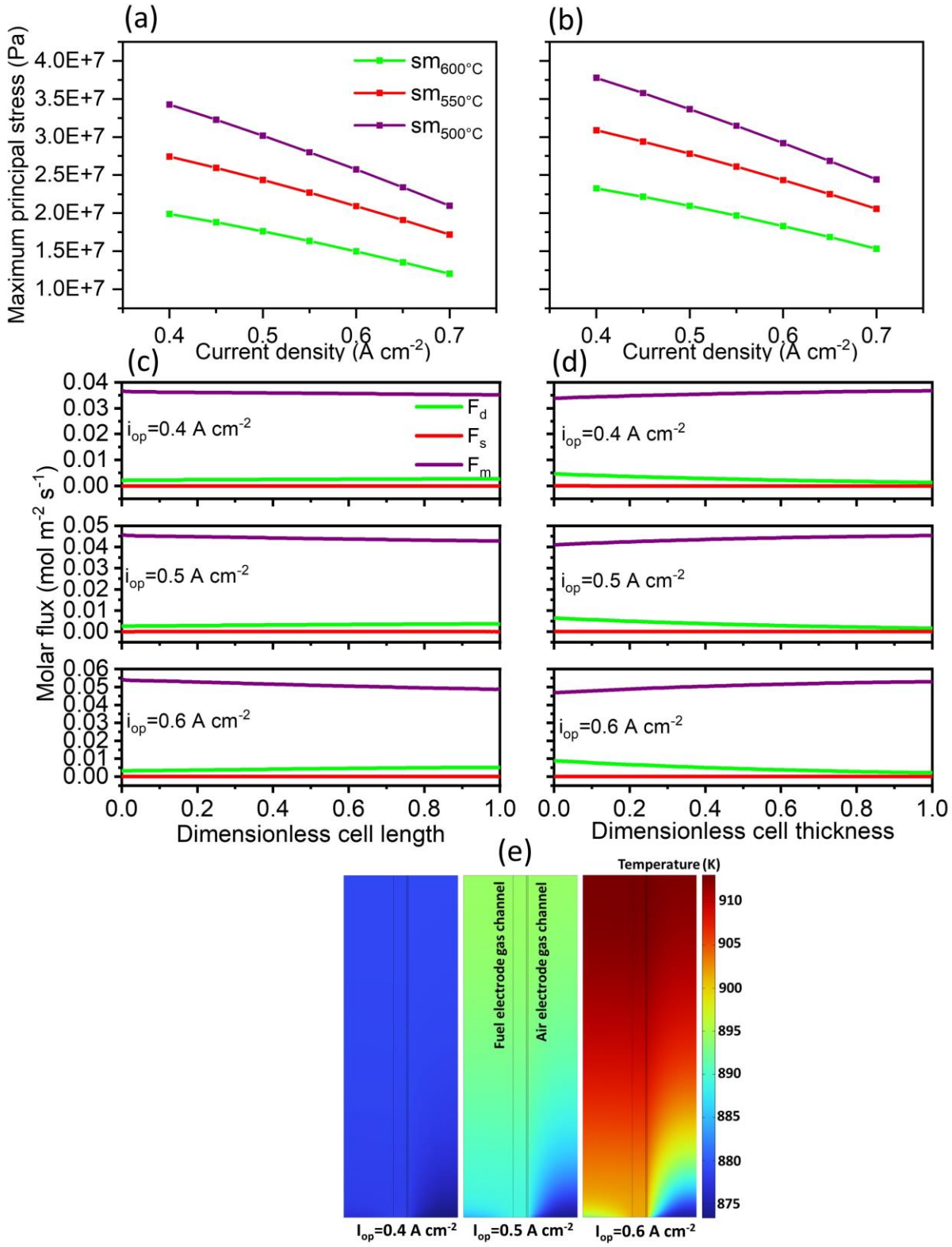

Figure 4.2 The effects of current density on the (a) maximum principal stress without considering chemical expansion; (b) maximum principal stress with considering chemical expansion; molar flux of protonic defects within the electrolyte with the consideration of chemical expansion (c) along the dimensionless cell length and (d) along the dimensionless cell thickness, Fd: diffusive molar flux, Fm: migrative molar flux, Fs: stress-induced molar flux; (e) temperature distribution with considering chemical expansion.

In Figure 4.2 (a) and (b), the maximum principal stress decreases with an increase in current density, regardless of whether the mechanical model accounts for chemical expansion. This can be explained by Figure 4.2 (d), which illustrates the temperature distribution in the PCEC. With an increase in current density, the generated heat also increases, resulting in a rise in the average temperature of the PCEC. Eq. (2-61), which defines the thermal strain, suggests that as the temperature in the PCEC approaches the reference stress-free temperature, the thermal strain should decrease, resulting in a decrease in thermal stress. Since the reference stress-free temperature defined in this work is the reduction temperature (T_{ref} = 700 °C), the thermal stress decreases as the temperature in the PCEC approaches T_{ref}. Therefore, the current density and operating temperature of PCEC should be well-controlled to ensure good electrolysis performance as well as mechanical integrity. The average temperature within the PCEC should not deviate too far from the reference temperature, otherwise high thermal stress may result. Furthermore, a comparison of Figure 4.2 (a) and (b) reveals that the impact of considering chemical expansion on the maximum principal stress becomes more prominent as the operating temperature increases. For example, at 0.4 A cm^{-2}, when the operating temperature increases from 500 °C to 600 °C, the difference between maximum principal stresses (with/without considering the chemical expansion) increases from 10.2% to 16.9%. This observation may suggest that, as the operating temperature rises, the effect of chemical expansion on the mechanical robustness of PCEC becomes increasingly significant. In addition, it is also found that increasing current density leads to a more serious chemical expansion. At 500 °C, as the current density increases from 0.4 A cm^{-2} to 0.5 A cm^{-2}, the chemically induced

stress is enhanced by 13.2%. Hence, the chemical expansion is sensitive to both operating temperature and current density.

In Figure 4.2 (c) and (d), the migrative molar flux of protonic defect within the electrolyte is enhanced significantly with the increase of current density. As the current density increases from 0.4 A cm^{-2} to 0.6 A cm^{-2}, the migrative molar flux increases by 42.9%. This can be attributed to that the current density can significantly change the electrochemical potential distribution. In addition, it demonstrates that electromigration dominates the transfer process of proton defects in the electrolyte. However, the magnitude of stress-induced molar flux of proton defect, as illustrated in both Figure 4.2 (c) and (d), is negligible not only along the dimensionless cell length but also along the dimensionless cell thickness. In other words, while the stress distribution in PCEC can impact the transport of protonic defects (based on Eq. (2-13)), its influence is insignificant when compared to diffusion and electromigration.

4.3.1.2 Effects of anode inlet flow rate

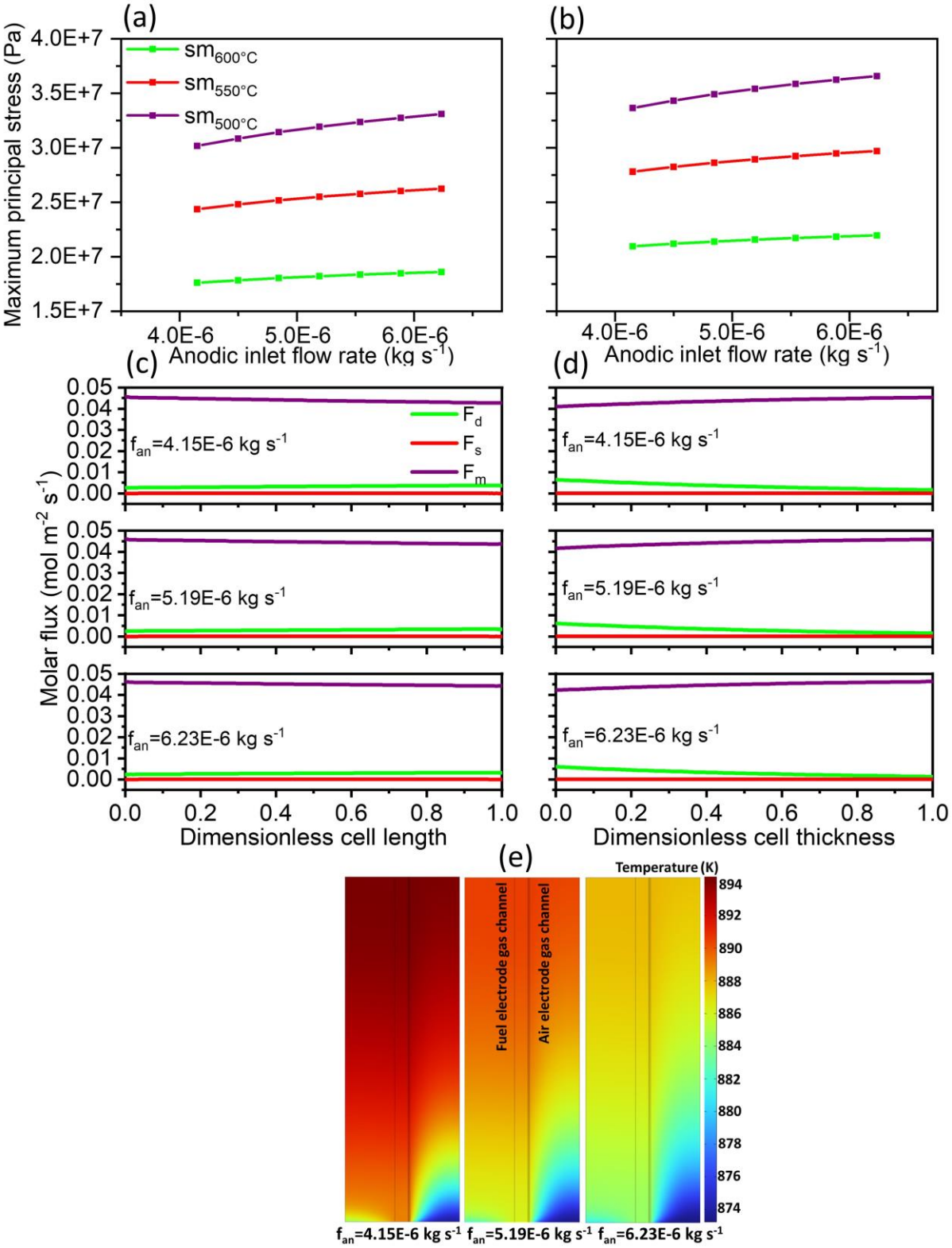

Figure 4.3 The effects of anode inlet flow rate on the (a) maximum principal stress without considering chemical expansion; (b) maximum principal stress with the consideration of chemical expansion; (c) molar flux of protonic defects within the electrolyte with the consideration of chemical expansion (c) along the dimensionless cell length and (d) along the

dimensionless cell thickness; (e) temperature distribution with the consideration of chemical expansion.

Figure 4.3 (a) and (b) show that the maximum principal stress exhibits a positive correlation with an increase in the anode inlet flow rate. This observation can be explained by referring to Figure 4.3 (e). As the anode flow rate increases, more heat is removed from the PCEC, leading to a decrease in the average temperature of the PCEC. Moreover, such an effect of anode inlet flow rate on the maximum principal stress can be mitigated with the increase of operating temperature. For example, when the anode inlet flow rate increases by 50%, the maximum principal stress of PCEC reduces from 8.7 % at 500 °C to 4.8% at 600 °C. Therefore, this can suggest that the anode inlet flow rate poses a trivial effect on the mechanical behaviour of a PCEC. In addition, comparing Figure 4.3 (a) and (b), results show that with the increase of anode inlet flow rate, the effect of chemically induced stress on the maximum principal stress is slightly alleviated. When the anode inlet flow rate increases from 4.15×10^{-6} kg s^{-1} to 6.23×10^{-6} kg s^{-1} at 600 °C, the difference between maximum principal stresses decreases from 19.0% to 18.1%, which also indicates that the chemical expansion is insensitive to changes in the anode inlet flow rate. Besides, as shown in both Figure 4.3 (c) and (d), the effects of anode inlet flow rate on the transport process of protonic defects within the electrolyte are also negligible.

4.3.1.3 Effects of anode inlet steam fraction

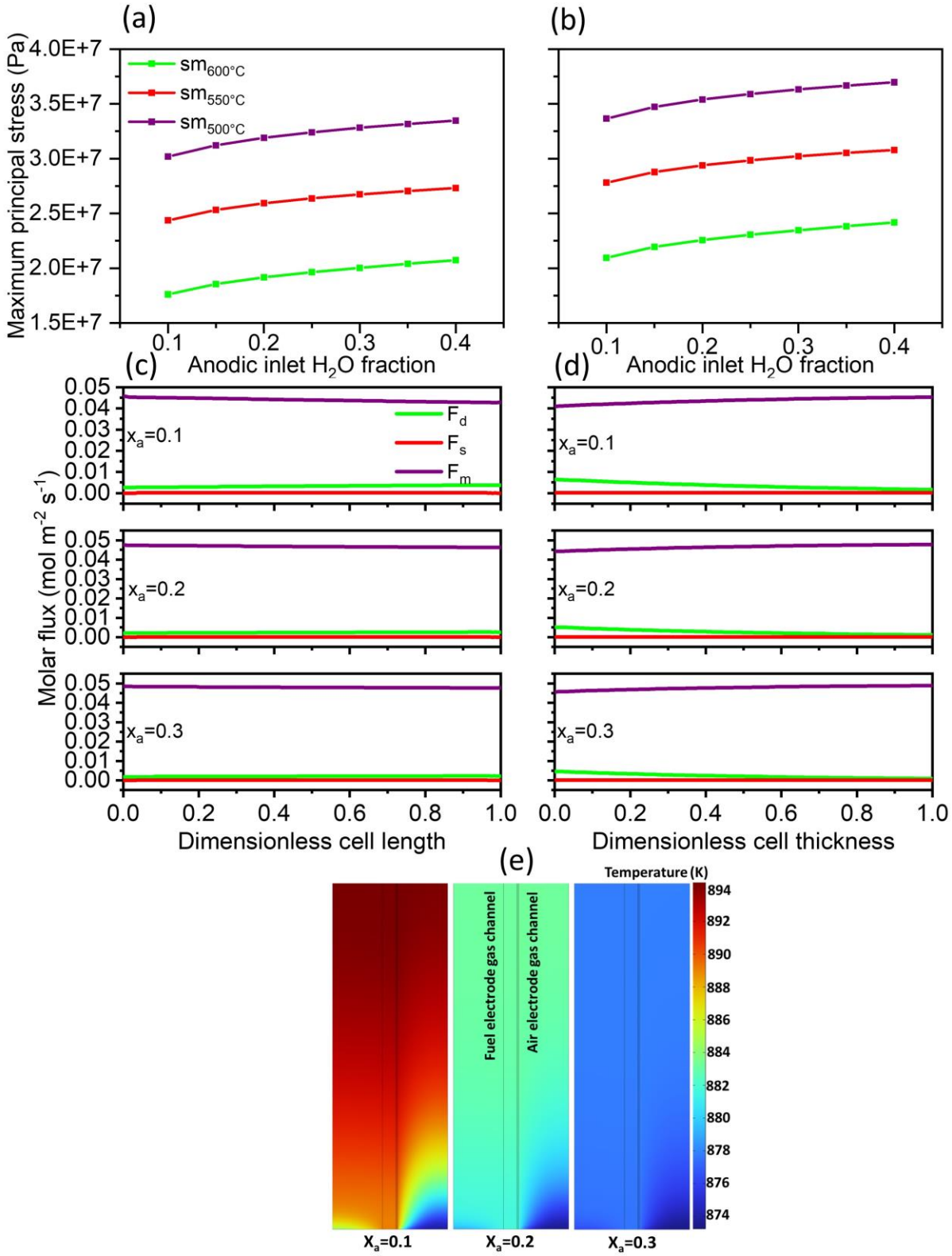

Figure 4.4 The effects of anode inlet steam fraction on the (a) maximum principal stress without considering chemical expansion; (b) maximum principal stress with the consideration of chemical expansion; molar flux of protonic defects within the electrolyte with the consideration of chemical expansion (c) along the dimensionless cell length and (d) along the dimensionless

cell thickness; (e) temperature distribution with the consideration of chemical expansion.

Similar to the effects of anode inlet flow rate, the increase in the anode inlet steam fraction can lead to an increase in the maximum principal stress, which is demonstrated in both Figure 4.4 (a) and (b). By examining Figure 4.4 (e), it is shown that as the anode inlet steam fraction increases, the average temperature of the PCEC deviates further from the reference stress-free temperature. However, such an effect of anode inlet steam fraction on the maximum principal stress can be enhanced by increasing the operating temperature. In Figure 4.4 (b), when the anode inlet H_2O fraction increases from 0.1 to 0.4, the maximum principal stress increases by 9.9% at 500 °C while increasing by 15.4% at 600 °C. Consequently, increasing the anode inlet steam fraction can contribute to the stress build-up in the PCEC. In addition, by comparing Figure 4.4 (a) and (b), it can be observed that when the chemical expansion is considered, the increase in the maximum principal stress diminishes as the anode inlet steam fraction increases. For example, when the anode inlet steam fraction varies from 0.1 to 0.4 at 600 °C, the increase in the maximum principal stress reduces from 19.0% to 16.6%. Therefore, the anode inlet steam fraction is an important operating factor to affect both the electrochemical and mechanical performance of PCECs. In Figure 4.4 (d), it is found that the changes in various types of protonic defect's molar flux along the dimensionless cell thickness are insignificant in response to changes in the anode inlet steam fraction. In Figure 4.4 (c), it can be observed that while the stress-induced molar flux remains unchanged, the diffusive and migrative molar fluxes exhibit slight variations with an increase in the anode inlet steam fraction. More specifically, as the anode inlet steam fraction increases, the diffusive molar flux of proton defect near the PCEC outlet slightly reduces while the migrative molar flux in the same region demonstrates a minute increase. In other words, the increase in the anode inlet steam fraction results in a more even distribution of both the diffusive and migrative molar fluxes across the dimensionless cell length. One possible reason for this observation could be that due to the

reduced temperature gradient within the PCEC, as shown in Figure 4.4 (e), the electrostatic potential and the concentration of protonic defects within the electrolyte are more uniformly distributed.

4.3.2 DOE results

4.3.2.1 Effects of different treatments

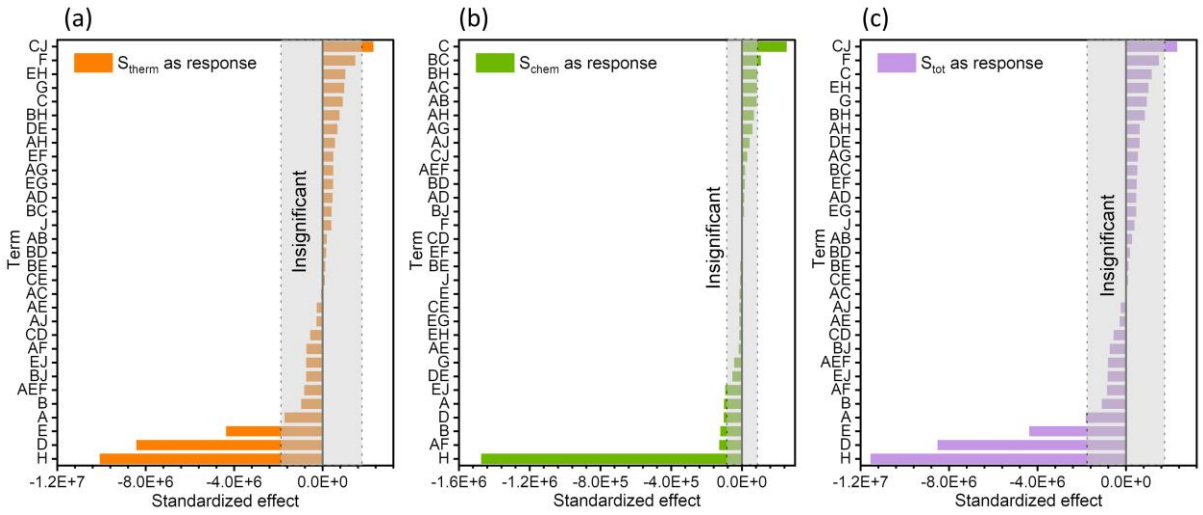

Figure 4.5 The standardized effects of different treatments on (a) thermal stress; (b) chemically induced stress; (c) total stress.

As shown in Figure 4.5, the standardized effects of different treatments are quantified. It is also worth mentioning that several treatments covered by the grey region are found to have no significant impact on the different responses. The significant treatments that are identified have different effects: if the standardized effect of a treatment is a positive value, then the response will increase with an increase in the treatment, and vice versa. In addition, the order of absolute value of different significant treatments is listed in Table 4-4, in which only the treatments with positive values are marked.

Table 4-4 The order of significant treatments.

Response	Order of significant treatments
Thermal stress	H > D > E > CJ (+)

Chemically induced stress	H > C (+) > AF > B > BC > D > A > EJ
Total stress	H > D > E > CJ (+) > A

It shows that the cathode porosity (H) is the most important parameter for different responses. Furthermore, since the effect value of cathode porosity is negative, the stress of PCECs can be significantly reduced by using a more porous cathode. The treatments with positive effect values are electrolyte thickness (C) and its interaction with anode porosity (J). Increasing electrolyte thickness can enhance chemical expansion, while the interaction between anode porosity and electrolyte thickness can contribute to the stress build-up in the PCECs. Figure 4.6 (a) and (e) show the interaction effect on the thermal stress and total stress, respectively. The effects of this interaction on thermal and total stress vary widely. Regarding thermal stress (Figure 4.6 (a)), the interaction has different effects on stress in the different regions, though its overall effect is positive. In contrast, for total stress (Figure 4.6 (e)), the positive effect of the interaction between anode porosity and electrolyte thickness is observed in all regions. Besides, the current density (D) and operating temperature (E) are the most important operating parameters for both thermal and total stress. The first four important parameters for both thermal stress and total stress are the same, which indicates that thermal stress is the dominant contributor to the overall stress of the PCECs.

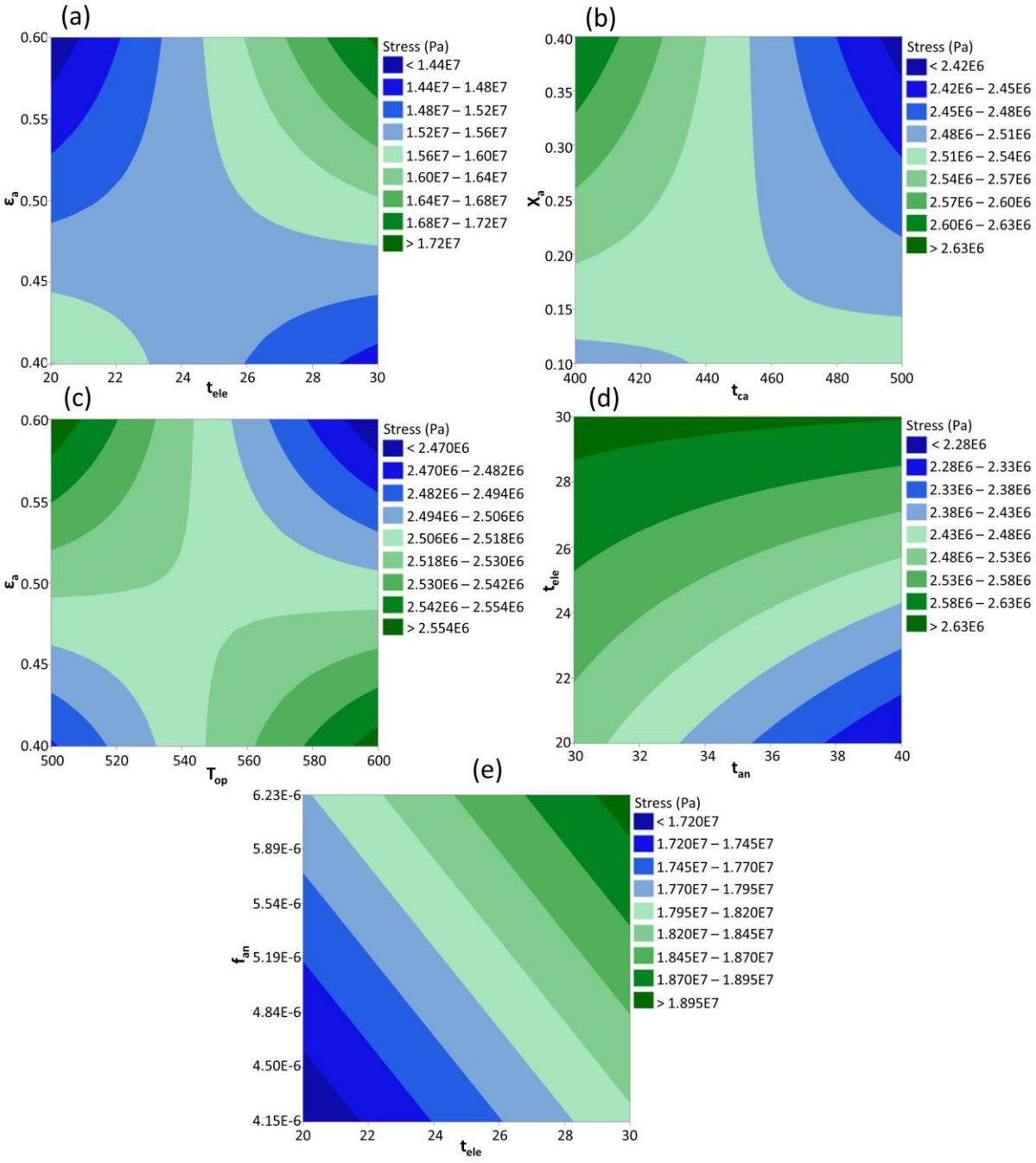

Figure 4.6 (a) the interaction between electrolyte thickness and anode porosity on the thermal stress; (b) the interaction between cathode thickness and anode inlet steam fraction on the chemically-induced stress; (c) the interaction between operating temperature and anode porosity on the chemically-induced stress; (d) the interaction between anode thickness and electrolyte thickness on the chemically-induced stress; (e) the interaction between electrolyte thickness and anode inlet flow rate on the total stress.

The current density is the most important operating parameter to the chemically induced stress.

However, it is worth noting that the interaction (Figure 4.6 (b)) between cathode thickness (A) and anode inlet steam fraction (F) and the interaction (Figure 4.6 (c)) operating temperature (E)

and anode porosity (J) are also important. The two contour plots (Figure 4.6 (b) and (c)) indicate that the bottom-left and top-right corners are the locations where lower chemically induced stresses can be achieved. Figure 4.6 (d) shows how a negative effect factor (anode thickness) interacts with a positive effect factor (electrolyte thickness). Based on the above analysis, the cathode porosity, current density, and operating temperature are the most significant parameters of the stresses in PCECs. To enhance the mechanical integrity of PCECs, these parameters should be well-controlled. However, it is worth noting that although increasing cathode porosity can reduce the stress and enhance the gas diffusion in the porous electrode, it may also cause a decrease in the conductivity as well as the number of electrochemically active sites [163].

4.3.2.2 Surrogate models

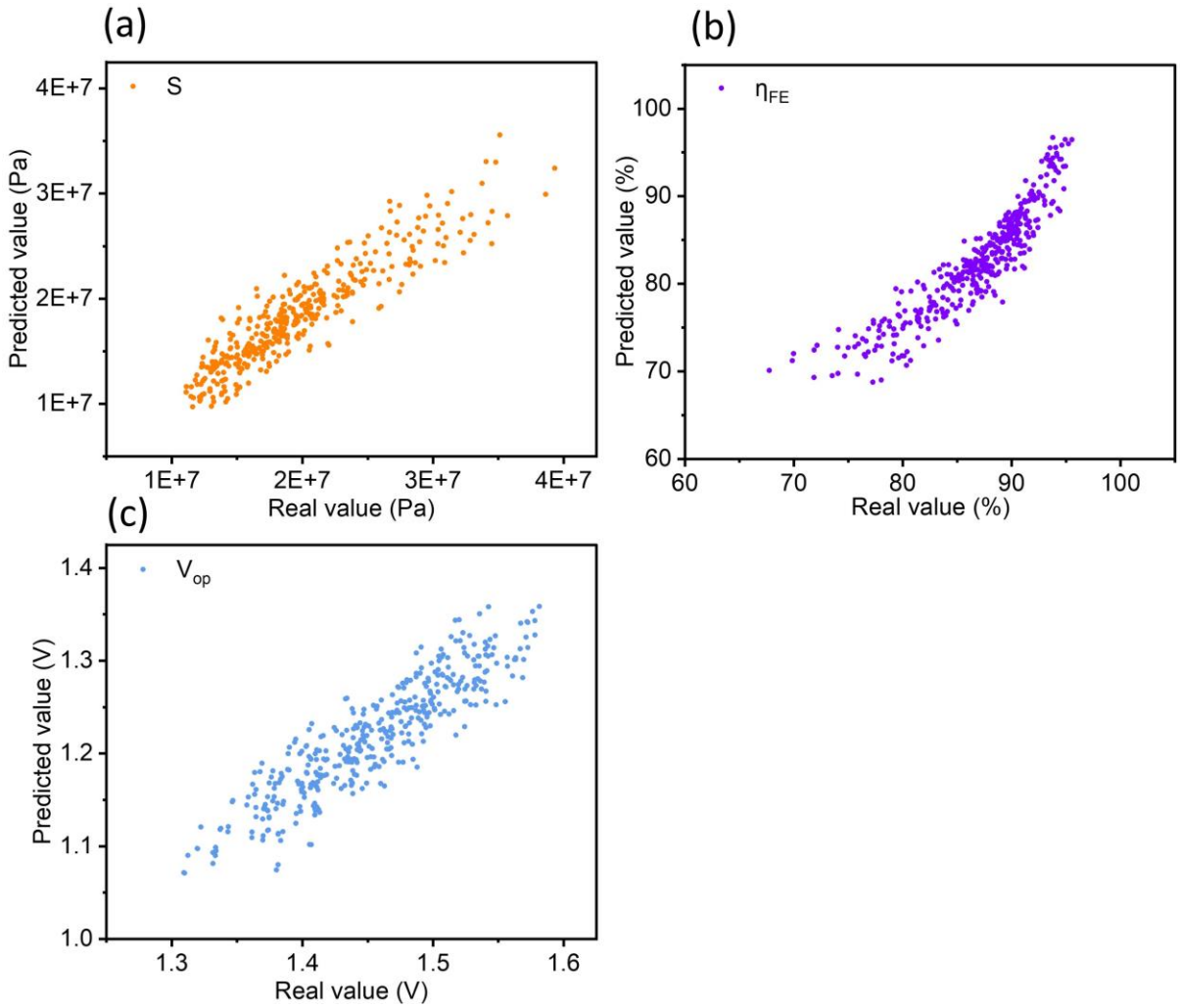

Figure 4.7 The performance of surrogate models derived from DOE results on the (a) stress; (b) faradaic efficiency; (c) operating voltage.

DOE can statistically identify the relationship between the independent variables and the dependent variables. This relationship can be mathematically expressed in terms of an equation, which can be subsequently applied as a surrogate model for predicting the performance of PCECs. Furthermore, this surrogate model is interpretable since 1) it quantitatively demonstrates the effects of different independent variables on the dependent variable; 2) it also shows quantitatively how combinations of different independent variables affect the dependent variable. Nine parameters are the independent variables, while the three responses are the dependent variables. In addition, to evaluate the predictive performance of the interpretable

surrogate models, four steps are taken as follows: 1) randomly generate 4096 points according to the range of factor values specified in Table 4-3; 2) randomly select 400 points from generated points; 3) use 400 points as the input of Multiphysics model and surrogate models to obtain the solutions, respectively; 4) calculate the R^2.

Table 4-5 The expressions of surrogate models.

Outputs	**Expressions**	**R^2**
Stress	$2.62 \times 10^8 - 2.08 \times 10^5 * t_c - 8.36 \times 10^5 * t_a - 1.26 \times 10^6 * t_{ele} - 8.84 \times 10^7 * I_{op} - 2.19 \times 10^5 * T_{op} - 2.50 \times 10^8 * x_a - 2.93 \times 10^4 * f_{an} - 1.70 \times 10^8 * \varepsilon_c + 2.48 \times 10^7 * \varepsilon_a + 522.7 * t_c * t_a + 48.91 * t_c * t_{ele} + 4.49 \times 10^4 * t_c * I_{op} + 212.1 * t_c * T_{op} + 5.29 \times 10^5 * t_c * x_a + 35.36 * t_c * f_{an} + 6.10 \times 10^4 * t_c * \varepsilon_c - 2.23 \times 10^4 * t_c * \varepsilon_a + 9.94 \times 10^3 * t_a * t_{ele} + 1.66 \times 10^5 * t_a * I_{op} + 191.4 * t_a * T_{op} + 8.37 \times 10^5 * t_a * \varepsilon_c - 7.24 \times 10^5 * t_a * \varepsilon_a - 5.40 \times 10^5 * t_{ele} * I_{op} + 157.6 * t_{ele} * T_{op} + 2.31 \times 10^6 * t_{ele} * \varepsilon_a + 6.06 \times 10^4 * I_{op} * T_{op} + 5.10 \times 10^5 * T_{op} * x_a + 29.91 * T_{op} * f_{an} + 1.01 \times 10^5 * T_{op} * \varepsilon_c - 8.23 \times 10^4 * T_{op} * \varepsilon_a - 1.06 \times 10^3 * t_c * T_{op} * x_a$	0.85
η_{FE}	$218.1 - 6.77 \times 10^{-2} * t_c + 1.113 * t_a + 2.91 \times 10^{-1} * t_{ele} - 112.7 * I_{op} - 1.01 \times 10^{-1} * T_{op} - 40.84 * \mathrm{x_a} - 2.01 \times 10^{-3} * f_{an} + 65.87 * \varepsilon_c - 203.4 * \varepsilon_a - 4.59 \times 10^{-3} * t_c * t_a + 1.22 \times 10^{-3} * t_c * t_{ele} + 3.08 \times 10^{-2} * t_c * I_{op} - 2.60 \times 10^{-5} * t_c * T_{op} - 0.117 * t_c * \mathrm{x_a} + 5.80 \times 10^{-5} * t_c * f_{an} - 0.051 * t_c * \varepsilon_a + 0.335 * t_c * \varepsilon_a - 1.66 \times 10^{-3} * t_a * t_{ele} + 0.379 * t_a * I_{op} - 7.42 \times 10^{-4} * t_a * T_{op} + 0.116 * t_a * \varepsilon_c + 2.134 * t_a * \varepsilon_a - 0.273 * t_{ele} * I_{op} - 1.61 \times 10^{-4} * t_{ele} * T_{op} - 1.287 * t_{ele} * \varepsilon_a + 0.0942 * I_{op} * T_{op} + 0.172 * T_{op} * \mathrm{x_a} - 1.90 \times 10^{-5} * T_{op} * f_{an} - 0.116 * T_{op} * \varepsilon_c - 2.00 \times 10^{-3} * T_{op} * \varepsilon_a + 1.74 \times 10^{-4} * t_c * T_{op} * \mathrm{x_a}$	0.83

V_{op}	$-4.213 + 0.0113 * t_c - 2.15 \times 10^{-3} * t_a + 2.80 \times 10^{-3} * t_{ele} - 0.784 * I_{op} + 0.0115 * T_{op} + 20.34 * x_a - 2.29 \times 10^{-4} * f_{an} + 0.0919 * \varepsilon_c + 0.920 * \varepsilon_a + 4 \times 10^{-6} * t_c * t_a - 5 \times 10^{-6} * t_c * t_{ele} + 2.84 \times 10^{-4} * t_c * I_{op} - 2.20 \times 10^{-5} * t_c * T_{op} - 0.0455 * t_c * x_a + 2.30 \times 10^{-5} * t_c * \varepsilon_c + 6.92 \times 10^{-4} * t_c * \varepsilon_a + 5.80 \times 10^{-5} * t_a * t_{ele} + 3.02 \times 10^{-3} * t_a * I_{op} + 2.00 \times 10^{-6} * t_a * T_{op} + 2.21 \times 10^{-3} * t_a * \varepsilon_c - 0.0103 * t_a * \varepsilon_a - 3.32 \times 10^{-3} * t_{ele} * I_{op} + 4.00 \times 10^{-6} * t_{ele} * T_{op} - 5.94 \times 10^{-4} * t_{ele} * pc - 7.24 \times 10^{-4} * I_{op} * T_{op} - 0.038 * T_{op} * x_a - 1.66 \times 10^{-4} * T_{op} * \varepsilon_c - 1.55 \times 10^{-3} * T_{op} * \varepsilon_a + 8.30 \times 10^{-5} * t_c * T_{op} * x_a$	0.82

Figure 4.7 illustrates the good capabilities of surrogate models in the prediction of stress, faradaic efficiency, and operating voltage. The expressions of surrogate models are summarized in Table 4-5. Hence, these interpretable surrogate models are useful for assisting in the optimization of PCECs. On one hand, unlike the 2D Multiphysics model of PCEC, the calculations required for these surrogate models are computationally inexpensive. Therefore, the optimization work of PCECs can be sped up. On the other hand, generating these surrogate models from DOE results is a simple process, unlike machine learning methods which require a large amount of data points for training. Consequently, DOE is a simple but effective method, which can also be extended to other modelling studies of PCECs.

4.4 Conclusions

In this work, an electro-thermo-chemo-mechanical model is developed to provide a comprehensive mechanical understanding of PCEC during the operation, in which both thermal expansion and chemical expansion are considered. Significantly, a framework, integrating a Multiphysics model and the DOE method, is proposed in this study to enable statistically-designed numerical investigations on PCECs. The effects of nine parameters and the interactions between them are systematically investigated in this study.

It is discovered that including chemical expansion in the mechanical model leads to a higher stress level in PCECs. However, thermal stress still dominates under various operating conditions. Furthermore, the primary route of transport for protonic defects within the electrolyte is electromigration. The effects of stress distribution on the transport of protonic defects can be disregarded under different operating conditions. Cathode porosity is identified as the most important parameter affecting the mechanical stress of PCEC. The most critical operating factors are current density and operating temperature. The results also show that chemical-induced stress can be enhanced by using a thicker electrolyte. Another output of the proposed framework is the interpretable surrogate models derived from DOE results. The R^2 calculation indicates that the surrogate models perform well in predicting the electrochemical and mechanical performance of PCECs. Therefore, the surrogate models can be further applied to the future optimization work of PCECs.

Overall, this study demonstrates that the chemical expansion of the electrolyte material should be considered in the mechanical analysis of PCECs. Incorporating this phenomenon can result in more realistic simulation outcomes. Moreover, the framework proposed in this study can help researchers systematically design their numerical studies and provide a simple and effective way to analyse the simulation outcomes.

Chapter 5 Multi-objective optimization of a protonic ceramic electrolysis cell with the consideration of current leakage

5.1 Introduction

As the previous section concluded, adjusting the operating parameters of PCEC can be an effective and simple way to improve the FE of PCEC [151]. For example, it is found that the FE tends to be lower at a higher operating temperature. Therefore, the operating temperature can be a useful parameter to adjust the FE. In addition, the gas species composition at the anode also has a significant influence on the FE. Furthermore, an optimal FE can be found with the increase of current density. Therefore, it is of great importance to understand the influence of various operating parameters on the FE. However, some PCEC performance metrics will be weakened when aiming to improve FE. Specifically, although lowering the operating temperature can improve the FE, it can also bring undesired consequences, such as low hydrogen production rate (low current density) and high electrical power demand (high operating voltage) [152,153]. In other words, FE can conflict with other PCEC performance metrics. Therefore, in addition to adjusting various operating parameters to improve FE, it has considerable practical importance to devote optimization efforts to trade-off between FE, current density, and voltage.

To perform such a multi-objective optimization in PCEC, a framework depicted in Figure 5.1 is proposed in this study. In the first step, a 2D Multiphysics model which fully considers the mass/momentum/heat/electrochemical processes and the current leakage phenomena in the PCEC is developed. Noteworthy, the development of this 2D Multiphysics model has been described in the previous section. Next, the Multiphysics model is used to generate a dataset that will be used to train a DNN-based model. DNN model can accurately reproduce the Multiphysics model results [77,78]. DNN model will play an important role in the multi-

objective optimization process because it consumes less computation time than the Multiphysics model, thereby speeding up the optimization process [77,78]. It is worth noting that before the multi-objective optimization process, the DNN model is also used to accelerate the GSA, aiming to evaluate the sensitivity of the output to changes in different operating parameters. In the final step, the set of solutions obtained from the multi-objective optimization process is weighed to determine the best trade-off design point [154]. The present study proposes an efficient and time-saving framework to accelerate the solution of the multi-objective optimization problem in PCECs. Importantly, this method can be extended to other multi-objective optimization problems in PCECs. Furthermore, the optimal trade-off point identified in this study can be a useful reference to guide the PCEC operation.

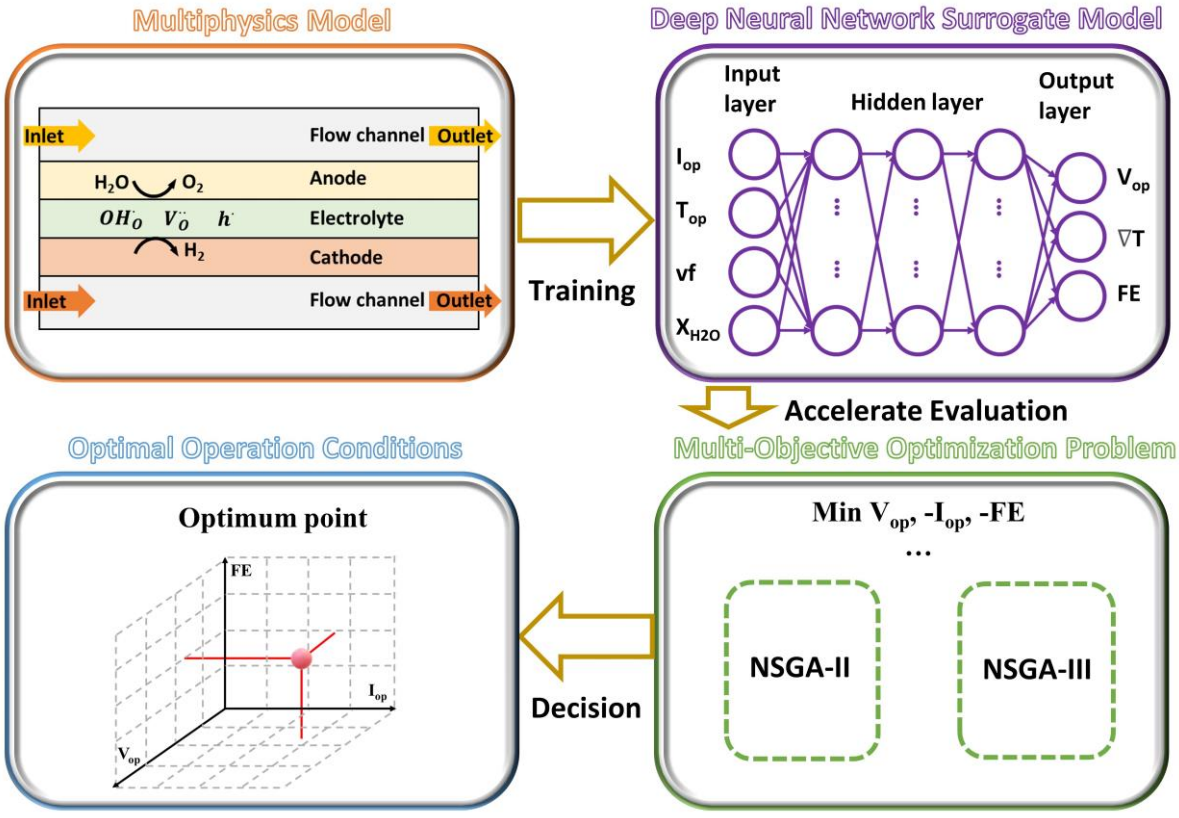

Figure 5.1 The framework for solving the multi-objective optimization problem in PCECs.

5.2 Modelling methodology

5.2.1 DNN

In the present work, a DNN model with three hidden layers is developed, as shown in Figure 5.1. The input and output layers respectively consist of four input neurons and three output neurons. Four operating parameters are selected to be the inputs: 1) the operating current density, I_{op}; 2) the operating temperature, T_{op}; 3) the anode inlet flow rate, vf; 4) the anode inlet steam fraction, X_{H2O}. Noteworthy, the operating parameters at the anode side are selected since they are more important than that at the cathode side according to the conclusions from the previous section. Three performance indicators of PCEC are selected as the outcome of the output layer: 1) the operating voltage, V_{op}); 2) the maximum temperature gradient, ∇T); 3) the Faraday efficiency, FE). To generate the data for training the DNN model, a total of 3450 solutions are generated from the 2D Multiphysics model. Subsequently, a matrix of 3450 × 7 datasets is constructed, which is further randomly split into a training set and a testing set with a ratio of 0.8:0.2.

5.2.2 Multi-objective optimization algorithm

There are three objectives: 1) minimizing the operating voltage (V_{op}); 2) maximizing the Faraday efficiency (FE); 3) maximizing the current density (I_{op}). In addition, a maximum temperature gradient (∇T) of 10 K cm^{-1} is set as the constraint. The range of various parameters is summarized in Table 5-1. Thereafter, the multi-objective problem of this work can be formulated as:

$$\begin{aligned} &\min\{V_{op}, -FE, -I_{op}\} \\ &s.t.: \nabla T \leq \nabla T_{max} \end{aligned} \tag{1}$$

$$Bounds: \begin{cases} I_{op,min} \le I_{op} \le I_{op,max} \\ T_{op,min} \le T_{op} \le T_{op,max} \\ vf_{min} \le vf \le vf_{max} \\ X_{H_2O,min} \le X_{H_2O} \le X_{H_2O,max} \\ SU_{min} \le SU \le SU_{max} \end{cases}$$

Table 5-1 Range of different parameters.

Parameters	**Lower limit**	**Upper limit**
∇T (K cm^{-1})	-	10
I_{op} (A cm^{-2})	0.3	0.8
T_{op} (°C)	400	600
$vf \times 10^6$ (kg s^{-1})	8.259	82.59
X_{H_2O}	0.1	0.9
SU (%)	50	90

The Non-dominated Sorting Genetic Algorithm II (NSGA-II) and NSGA-III are used in solving the multi-objective optimization problem. NSGA-III is an extension of NSGA-II aimed at tackling a large number of objectives (≥ 3) more efficiently than NSGA-II [155]. Details of NSGA-II and NSGA-II can be found in Refs. [155–158]. First, the NSGA-II is used for solving the three-objective optimization problem. Second, the NSGA-III is applied to solve the same three-objective optimization problem. Third, the Technique for Order Preference by Similarity to an Ideal Solution (TOPSIS) is applied to identify the optimal trade-off points from the Pareto sets obtained from the NGSA-II and NSGA-III [159]. Some other literature using TOPSIS can be found in Refs [160–162]. It is worth noting that three different weight combinations are used for identifying the optimum design points (Table 5-2).

Table 5-2 Three weights combinations.

Weights	**Point**	**V_{op}**	**FE**	**I_{op}**
W1	A	0.3	0.3	0.4
W2	B	0.3	0.4	0.3

W3	C	0.4	0.3	0.3

5.2.3 Performance of DNN model

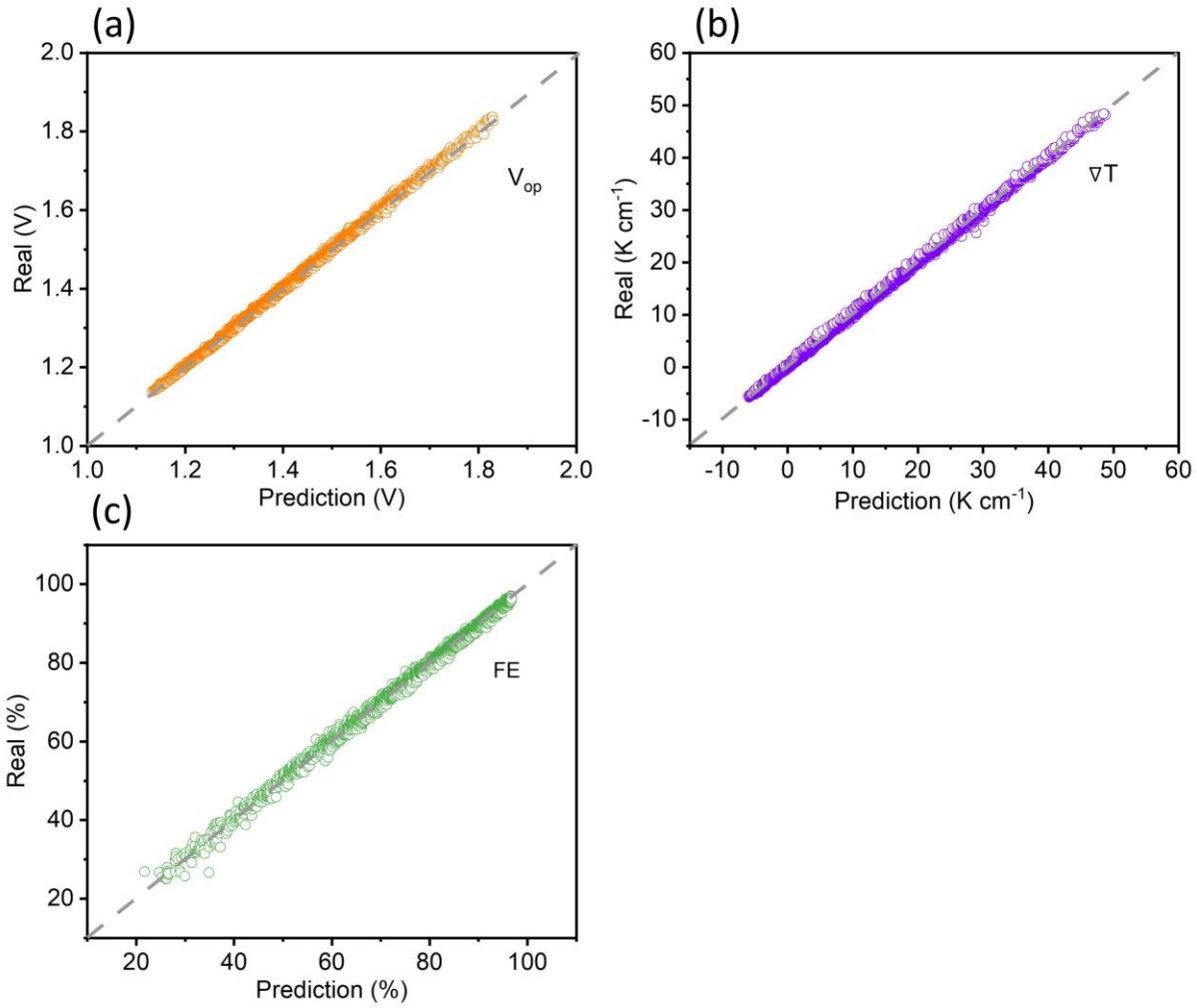

Figure 5.2 Performance of the DNN model on (a) the applied voltage; (b) the maximum temperature gradient; (c) the FE.

The performance of the DNN model is shown in Figure 5.2, where the DNN model predicted results are compared with the Multiphysics results. In addition, the R^2 and RMSE results of the DNN model are listed in Table 5-3. The DNN model shows a good capability to predict different outcomes and can serve as the surrogate model of the 2D Multiphysics model.

Table 5-3 R^2 and RMSE of DNN model.

Metrics	**V**	**∇T**	**FE**
R^2	0.998	0.992	0.998

RMSE	0.039	0.053	0.035

5.3 Results and discussions

5.3.1 GSA results

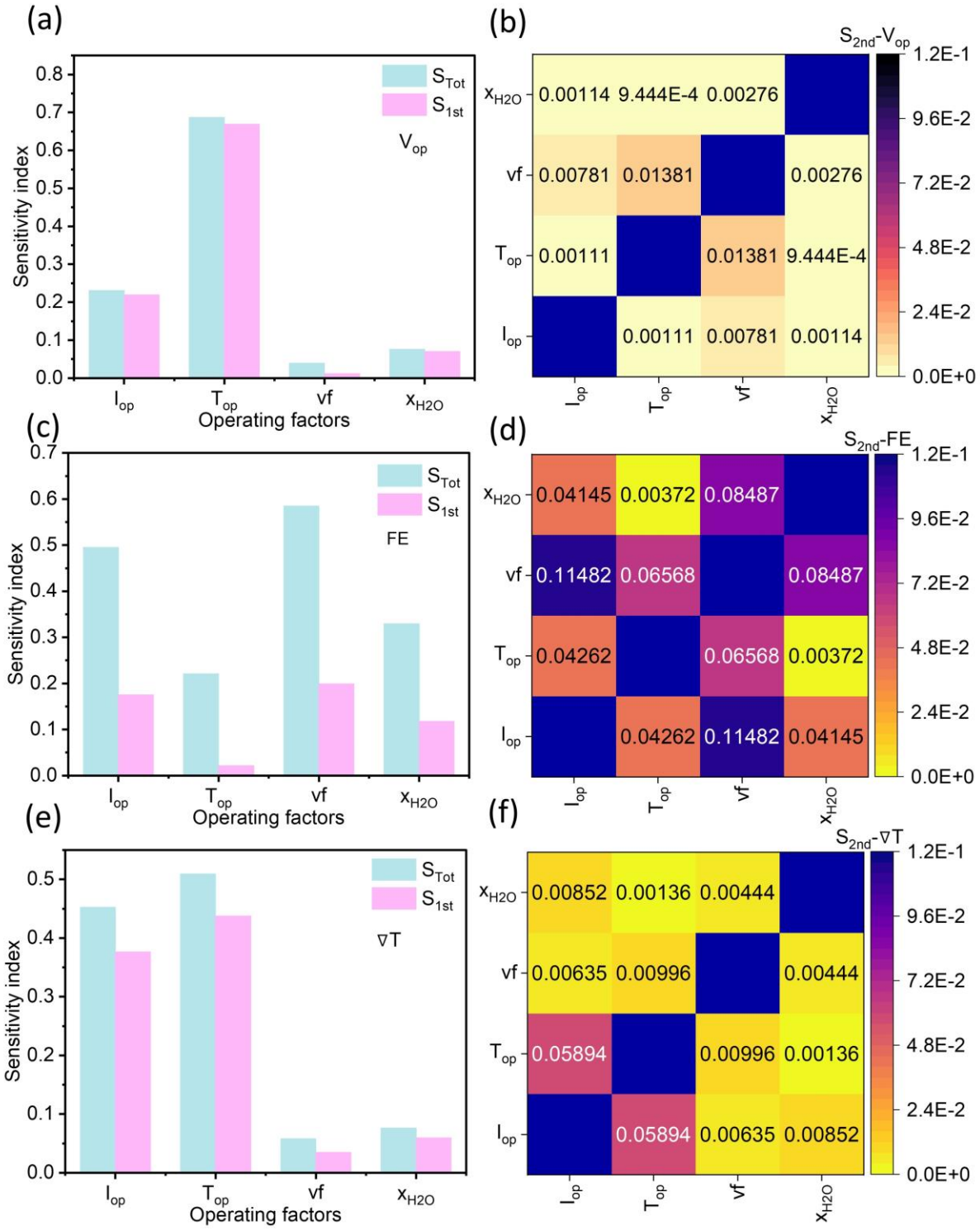

Figure 5.3 When V_{op} is the output: (a) first-order SIs and total SIs of different parameters, (b)

second-order SIs between parameters; When FE is the output: (c) first-order SIs and total SIs of different parameters, (d) second-order SIs between parameters; When ∇T is the output: (e) first-order SIs and total SIs of different parameters, (f) second-order SIs between parameters.

In Figure 5.3 (a), the working temperature shows the most significant impact on the V_{op}, while the anode inlet flow rate is the most insignificant factor to V_{op}. Although the current density is the second important factor, its total SI is less than one-third of the total SI of the working temperature. Figure 5.3 (b) can explain why the total SI of the anode inlet flow rate is larger than its first-order SIs in Figure 5.3 (a). In Figure 5.3 (c), when the FE is the outcome, it is evidently that the anode inlet flow rate has the highest first-order SI, followed by the current density. The same order can also be found in the total SI. However, the total SIs of the current density and the anode inlet flow rate are substantially larger than their first-order SIs. When the maximum temperature gradient is the output parameter, the operating temperature and the current density are two of the most important factors (Figure 5.3 (e)).

5.3.2 Parametric studies

5.3.2.1 Effects of current density

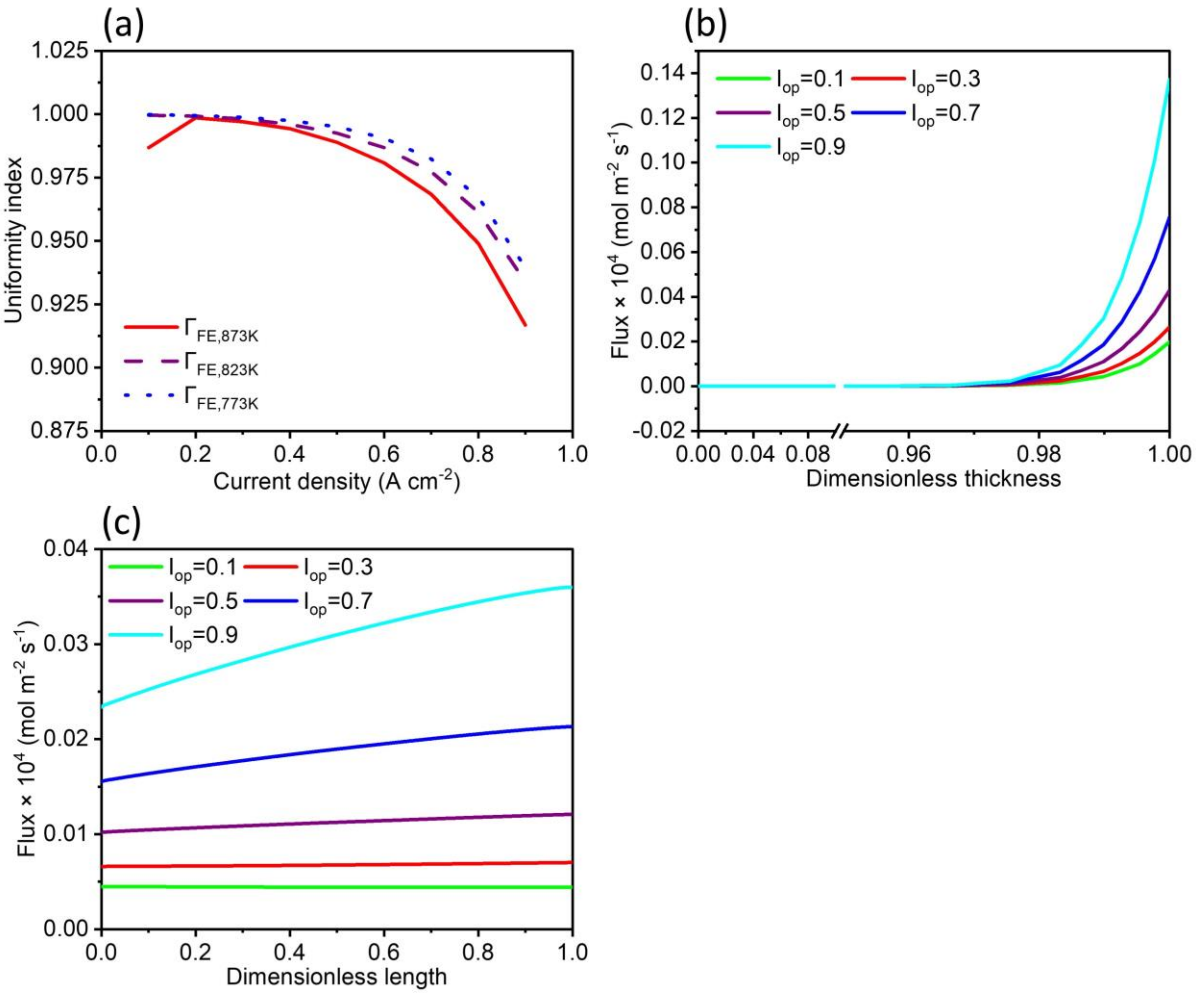

Figure 5.4 Effects of current density on the (a) uniformity of FE; (b) the transport flux of electron-hole along the dimensionless cell thickness at 873 K; (c) the transport flux of electron-hole along the dimensionless cell length at 873 K.

In this work, to quantitatively evaluate the uniformity of FE distribution, a uniformity index of FE (Γ_{FE}) is introduced as [163]:

$$\Gamma_{FE} = 1 - \sqrt{\frac{1}{n} \cdot \left(\sum_{i=1}^{n} \frac{FE_i - \overline{FE}}{\overline{FE}} \right)^2} \quad (2)$$

Where n is the number of nodes in the computational domain, $\overline{FE}$ is the mean of FE. When the current density increases from 0.1 A cm^{-2} to 0.2 A cm^{-2}, the Γ_{FE} increases by around 1.3% at

873 K (Figure 5.4 (a)). However, with a further increase in current density, the temperature gradient increases, leading to a reduction in Γ_{FE}. Furthermore, when the current density is fixed, Γ_{FE} of PCEC tends to be higher at a lower operating temperature. In Figure 5.4 (b) and (c), the electron-hole transport flux along the thickness is considerably larger than that along the cell length. The enhanced transport flux should be mainly attributed to the change in the partial pressure. Noteworthy, in Figure 5.4 (c), no notable change can be found in the flux at 0.1 A cm^{-2}. However, the flux increases by about 40% from inlet to outlet at 0.9 A cm^{-2}, leading to a more non-uniform distribution of FE. From the analysis, the current density is an important factor to affect the FE and electrochemical performance of PCEC. In the practical operation, the current density should be well controlled to make PCEC exhibit higher FE.

5.3.2.2 Effects of anode inlet flow rate

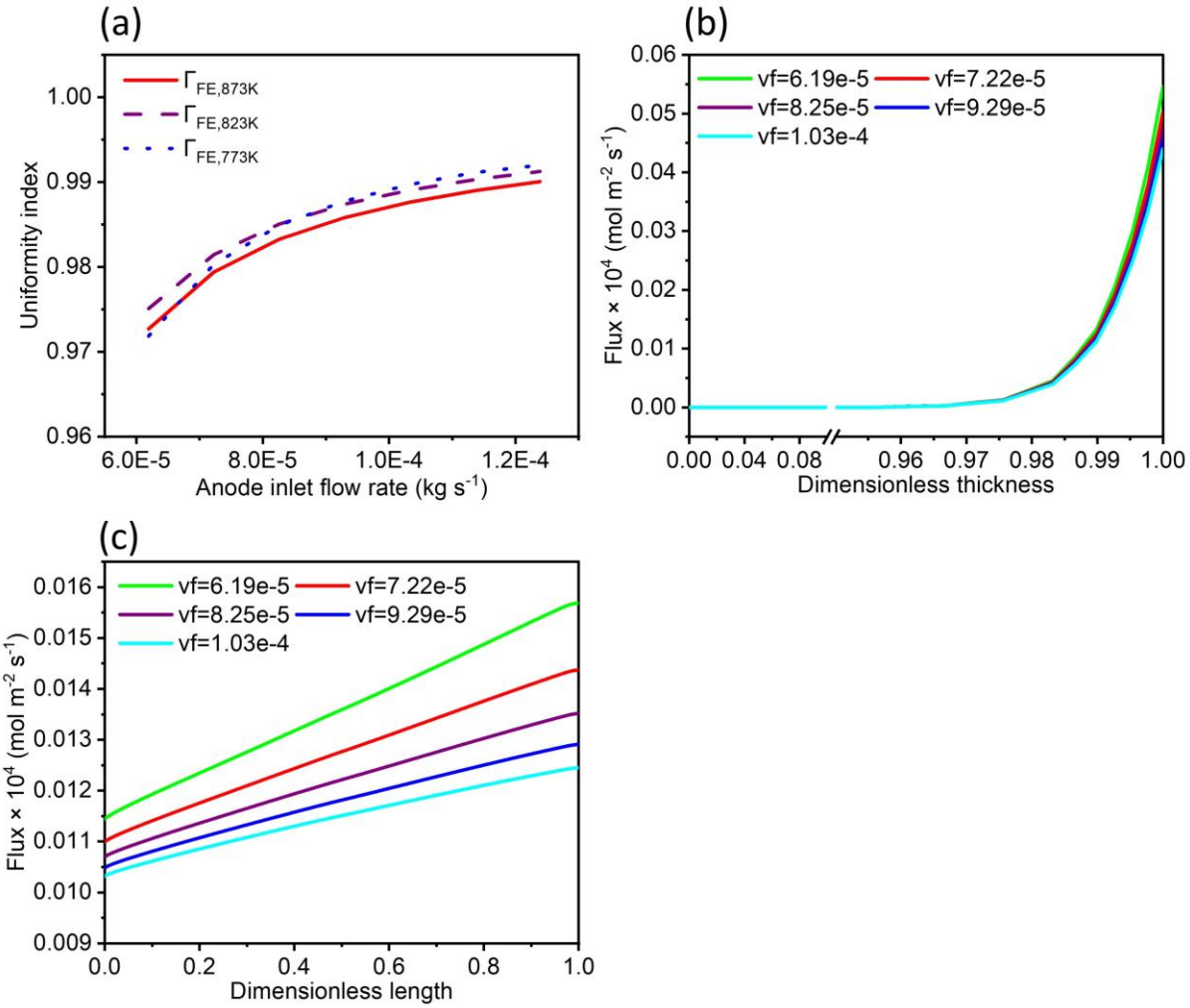

Figure 5.5 Effects of anode inlet flow rate on the (a) uniformity of FE at 0.5 A cm^{-2}; (b) the transport flux of electron-hole along the dimensionless cell thickness at 873 K 0.5 A cm^{-2}; (c) the transport flux of electron-hole along the dimensionless cell length at 873 K 0.5 A cm^{-2}.

In Figure 5.5 (b), the Γ_{FE} of PCEC is higher at a higher anode inlet flow rate. However, as the anode inlet flow rate increases, such a positive effect of the anode inlet flow rate on the Γ_{FE} becomes negligible. From Figure 5.5 (b) and (c), it can be observed that the transport flux along the cell length is more sensitive to the change in the anode inlet flow rate than that along the cell thickness. As the anode inlet flow rate increases, the flux decreases, thereby favouring the enhancement of FE. Moreover, when the anode inlet flow rate is varied from 6.19×10^{-5} kg s^{-1} to 1.03×10^{-4} kg s^{-1}, the flux increase from inlet to outlet is reduced by 16% (Figure 5.5 (c)), which is favourable to the improvement of Γ_{FE}. Although increasing the anode inlet flow rate

can be a potential operating strategy to enhance the FE, it can also decrease the steam utilization of PCEC.

5.3.2.3 Effects of anode inlet steam fraction

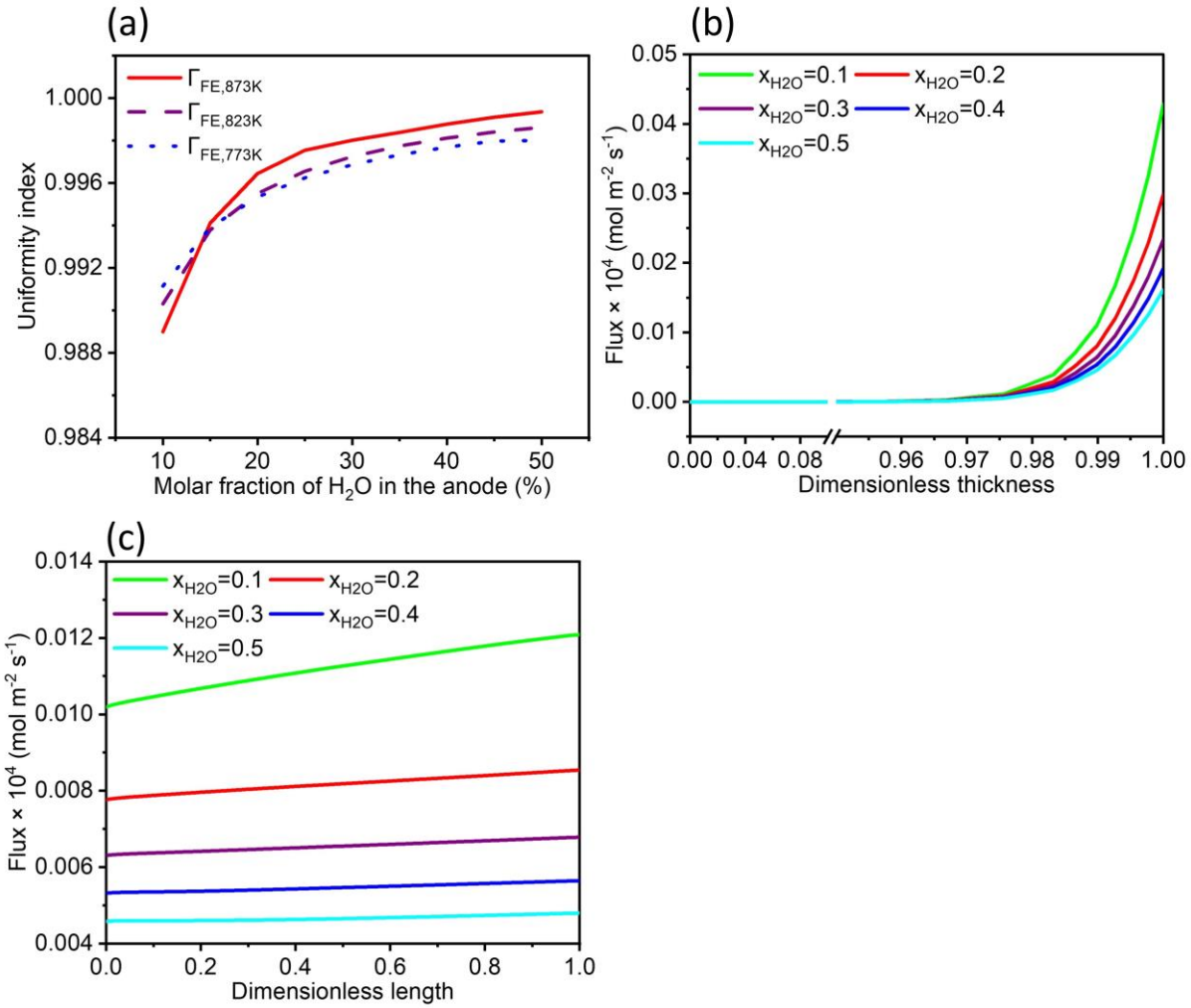

Figure 5.6 Effects of anode inlet steam fraction on the (a) uniformity of FE at 0.5 A cm^{-2}; (b) the transport flux of electron-hole along the dimensionless cell thickness at 873 K 0.5 A cm^{-2}; (c) the transport flux of electron-hole along the dimensionless cell length at 873 K 0.5 A cm^{-2}.

In Figure 5.6 (a), the Γ_{FE} of PCEC increases monotonously with the increase of cathode inlet steam fraction. Increasing the anode inlet steam fraction is equivalent to increasing the anode inlet steam partial pressure. In addition, since the inlet flow at the anode is a steam-air mixture, the oxygen partial pressure can be considerably reduced with the increase of the anode inlet steam fraction. Therefore, the formation of electron-hole can be suppressed, thereby improving

the FE. This is also demonstrated in Figure 5.6 (b) and (c). With the increase of anode inlet steam fraction, the transport flux of electron-hole is reduced not only along the cell thickness but also along the cell length. Furthermore, in Figure 5.6 (c), the variation in the transport flux of electron-hole from inlet to outlet decreases with the increase of anode inlet steam fraction, which also implies an increase in the Γ_{FE}. However, such an effect also weakens accordingly. Based on the above analysis, the increasing anode inlet steam fraction can pose a positive impact on enhancing the FE. Nevertheless, simply increasing the anode inlet steam fraction could also present some drawbacks. For example, the steam utilization should decrease with increasing anode inlet steam fraction. As a result, the anode inlet steam fraction is an important operating parameter to PCEC performance and should be well adjusted.

5.4 Multi-objective optimization results

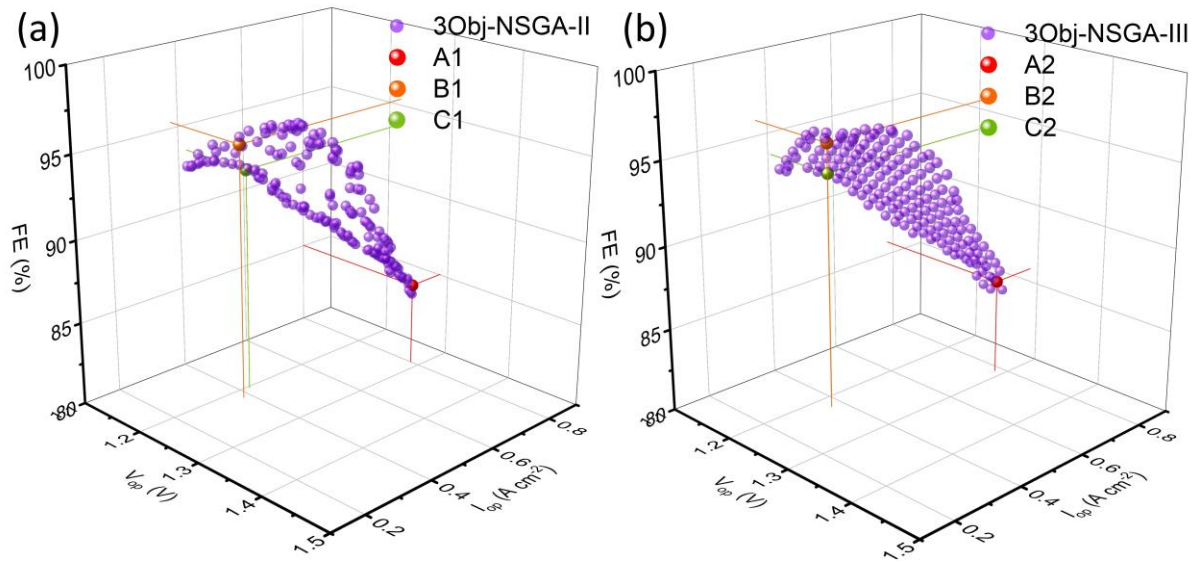

Figure 5.7 (a) Three-objective optimization problem solved by NSGA-II; (b) Three-objective optimization problem solved by NSGA-III.

After the multi-objective optimization process, a total of 336 non-dominated points is obtained. The objective spaces attained by NSGA-II and NSGA-III are similar. However, the non-dominated points determined by NSGA-III are more evenly distributed in the space, since NSGA-III uses a reference point-based method that allows NSGA-III to provides a more

diverse set of solutions than NSGA-II [157]. Besides, the TOPSIS method is applied to find trade-off optimal points out of all obtained non-dominated solutions, which are also shown in Figure 5.7. Noteworthy, three different weight combinations (Table 5-3) are used in the TOPSIS decision process. For example, when W1 is assigned to each objective function, the optimal points, A1 and A2, can be determined by the TOPSIS method on the NSGA-II and NSGA-III results, respectively. The details of different optimal points are listed in Table 5-4. At different weights, the difference between the optimal points of NSGA-II and NSGA-III is quite small. However, when applying the TOPSIS method to pick the optimal points from the entire solution set, including all non-dominated points obtained from NSGA-II and NSGA-III, the optimal points at different weights are in the NSGA-III solution set.

Table 5-4 The optimal trade-off points.

Algorithms	**Points**	**V_{op} (V)**	**FE (%)**	**I_{op} (A cm^{-2})**	**T_{op} (°C)**	**vf × 10^6 (kg s^{-1})**	**x_{H2O}**
	A1	1.288	85.04	0.800	599.99	15.00	0.900
NSGA-II	B1	1.217	95.35	0.380	576.880	8.27	0.899
	C1	1.203	93.46	0.425	599.728	8.87	0.899
	A2	1.288	85.82	0.780	599.05	17.51	0.899
NSGA-III	B2	1.222	95.92	0.367	566.877	8.29	0.900
	C2	1.198	93.66	0.409	599.460	8.30	0.900

The analysis of Table 5-4 reveals a consistent trend wherein the inlet steam fraction at various optimal points is all around 0.9. This observation underscores that maintaining a higher steam

fraction is conducive not only to enhancing electrochemical performance but also to improving Faradaic efficiency [164]. Notably, when current density and applied voltage are prioritized, the corresponding temperature is at least 20 °C higher compared to the scenario where Faradaic efficiency takes precedence. This emphasizes the pivotal role of temperature control in practical operations for achieving a delicate balance between electrochemical performance and FE. The observed tendency for the inlet flow rate to be lower under conditions where FE and voltage are the primary objectives can be attributed to constraints imposed by steam utilization. Although the steam utilization is limited to 50%-90% in this work, another study on SOEC system optimization use a fixed steam utilization of 40% [165]. The optimal current density attained in their work is only around 0.1 A cm^{-2}, a value deemed relatively small for a high-temperature electrolysis cell [165]. While another study also indicates the optimized current density in a SOEC system should be less than 0.2 A cm^{-2}. The difference between the current work and previous study on the optimized current density could be from the fact that this study is focused on the cell-level, while the previous study operates at the system level, taking into consideration factors such as cost and exergy efficiency. Therefore, it underscores that the optimization work of this study is not exhaustive, indicating the need for future optimization efforts on a PCEC system scale. Furthermore, a major advantage of PCEC over low-temperature electrolysis cells lies in its higher current density, thereby delivering a higher hydrogen production rate. Given this consideration, points B and C may not be as ideal as point A due to their lower current density, potentially limiting their ability to fully exploit the advantages of PCEC. Consequently, points A1 and A2 are recommended as the optimal choices for the practical operation of PCEC. In addition, the base working conditions of PCEC operation are outlined in the Boundary Conditions section. When comparing PCEC in the base case to PCEC under the optimal condition, there is an 8% improvement in electrochemical performance. Notably, the improvement in FE exceeds 20% under the optimal condition. It

suggests that the optimal condition has a pronounced impact on the efficiency of the electrochemical processes within the PCEC. Another noteworthy observation is that the voltages in points B and C are both less than the TNV, suggesting that the PCEC is operating in an endothermic mode. In contrast, for point A, the voltage is approximately equal to TNV. Hence, it shows that achieving thermo-neutral operation in PCEC can be considered as a strategic means to attain a balanced compromise between hydrogen production capability and FE. Noteworthy, realizing thermo-neutral operation is also an important target in other SOEC studies [166]. For example, in ref [76], it stated that achieving thermo-neutral operation of electrolysis cells can mitigate thermal failures and prolong service life. The study further reports that an increase in steam fraction in electrolysis cells is conducive to thermo-neutral operation, a finding analogous to the results presented in the current work. However, it must be acknowledged that the multi-objective optimization of PCEC with the consideration of FE is still a relatively limited area of study. In the future, more optimization study should be done in a PCEC system level.

5.5 Conclusions

To achieve a trade-off between the electrochemical performance and faradaic efficiency of PCEC, a framework connecting the Multiphysics model and the DNN model is proposed. The Multiphysics model is used to train the DNN model. The DNN model is further used as a surrogate model to speed up the solution of multi-objective optimization problems. The applied voltage, FE, and current density are the objective targets. After the multi-objective optimization process, the TOPSIS method is implemented to pick the optimal design point out of all non-dominated solutions generated by the NSGA-II and NSGA-III algorithms.

In the parametric studies, it is found that with the increase of current density, the uniformity of FE decreases, while the transport of electronic holes within the electrolyte material is improved.

The transport flux of the electronic hole along the cell thickness is significantly larger than that along the cell length. In addition, it is found that the transport flux of the electronic hole along the cell length is more sensitive to the variation in the anode inlet flow rate than that along the cell thickness. Increasing the anode inlet steam fraction can pose a positive effect on suppressing the transport flux of the electronic hole, thereby enhancing the FE. The distribution of NSGA-III non-dominated solutions in space is found to be more diverse than NSGA-II non-dominated solutions. Moreover, three different weight combinations are used in the TOPSIS decision process. Therefore, a total of 6 optimal trade-off points is selected from the NSGA-II and NSGA-III results. Compared to the case where voltage or FE is a highly weighted target, the optimum points obtained with a current density as the main objective can make good use of the advantage of PCEC over low-temperature electrolysis cells.

Overall, the identified optimal points can provide a reference for the practical operation of PCEC. In addition, this study also exhibits the essential role of the DNN model in solving the multi-objective optimization problem. More importantly, the framework proposed in this study can be further applied to other multi-objective optimization problems in PCECs.

Chapter 6 Conclusions and Suggestions for Future Research

6.1 Conclusions

PCEC is a promising electrochemical technology to realize large-scale hydrogen production in the future. However, the intrinsic mixed-conducting property of electrolytes used in PCEC leads to the current leakage phenomenon, which significantly inhibits the performance of PCEC. Additionally, the chemical expansion phenomenon in the electrolyte also raises important concerns regarding the mechanical integrity of PCECs during operation. Therefore, numerical models combined with the DOE method or machine learning method are developed for understanding those phenomena in PCEC.

A series of parametric studies are conducted to investigate the effects of various operating parameters. Results show that when the heat transfer is considered, an optimal FE can be found with the increase in the current density. As the current density increases, the uniformity of FE decreases, while the transport of electronic holes within the electrolyte material is improved. The transport flux of the electronic hole along the cell thickness is significantly larger than that along the cell length. As the inlet flow rate increases, the temperature gradient of the cell decreases, while the FE shows the opposite trend. In addition, the transport flux of the electronic hole along the cell length is more sensitive to the variation in the anode inlet flow rate than that along the cell thickness. The applied voltage and temperature gradient both decrease with increasing inlet steam fraction, while FE increases continuously. Increasing the anode inlet steam fraction can also pose a positive effect on suppressing the transport flux of the electronic hole. In the optimization work of PCEC, operating voltage, current density and FE are selected as targets. The optimal operating conditions are determined with a current density as the main objective. Furthermore, it also discovers that the consideration of chemical expansion can lead to a higher stress level in PCECs. However, thermal stress still dominates

under various operating conditions. Besides, DOE results indicate the operating parameters at the anode side are more important than those at the cathode side. DOE results also suggest that cathode porosity is the most important parameter of the stress level. Additionally, current density and operating temperature are found to be the most important operating factors to the stress level of PCEC during the operation.

Overall, current leakage and chemical expansion are important phenomena that affect PCEC performance. The understanding of these phenomena can be enhanced through guidance from numerical models. Furthermore, this study shows that operating and structural parameters can effectively control and mitigate these problems, which is of great significance for the future operation and manufacturing of PCECs.

6.2 Suggestions for Future Research

Although this study considers the detailed transport of carriers in the electrolyte, the models developed are all two-dimensional. Therefore, 3D numerical models should be developed in the future to consider the transport of carriers in the electrolyte in two different scales:

The first is a 3D numerical model at the electrode scale. The 3D porous electrode structure should be reconstructed as the computational domain. Since the defect chemical reactions and electrochemical reactions are coupled with each other, the detailed reaction kinetics of the defect chemical reactions as well as the electrochemical reactions can be well-investigated. In addition, since the defect chemical reactions as well as electrochemical reactions are heterogeneous processes, the effects of the reaction active area in the electrode on the reactions should be explored. The electrode-scale 3D model will provide a fundamental understanding of the defect chemistry and electrochemistry in the PCEC. The second is a 3D numerical model at the cell or stack scale. The effects of other components such as interconnectors and sealants on the performance of PCEC can be considered. Novel thermal management strategies or stack

designs can be proposed to further enhance the performance of PCEC. Importantly, the dynamic behaviour such as the long-term degradation of PCEC can be evaluated through stack scale models. In this regard, some advancing operating strategies or designs can be further developed to extend the life of PCEC.

Moreover, the potential of artificial intelligence (AI) in advancing PCEC development should not be overlooked. On the one hand, there is the opportunity to develop specialized AI tools that can conduct high-throughput screening of materials. These tools aim to identify electrolyte materials with low electronic hole conductivity, expediting the search for optimal materials. Therefore, the faradaic efficiency of PCEC can be intrinsically improved. Additionally, as more experimental data on materials becomes available in the future, generative AI models can be developed. These models have the capability to reverse-engineer and propose material designs based on the specific requirements provided by users. On the other hand, AI can also contribute to simplifying complex numerical models. By identifying and focusing on the most important properties of interest to the user, AI techniques can streamline the numerical calculations involved, resulting in significant computational savings. Additionally, AI tools can play a vital role in connecting models at different scales, enabling a seamless integration of information across various levels of detail and complexity. This integration enhances the understanding of PCEC and aids in the development of comprehensive models. Overall, AI has immense potential to revolutionize PCEC research and accelerate advancements in the field.

References

[1] Fawzy S, Osman AI, Doran J, Rooney DW. Strategies for mitigation of climate change: a review. Environmental Chemistry Letters 2020;18:2069–94. https://doi.org/10.1007/s10311-020-01059-w.

[2] Gaulin N, Le Billon P. Climate change and fossil fuel production cuts: assessing global supply-side constraints and policy implications. Climate Policy 2020;20:888–901. https://doi.org/10.1080/14693062.2020.1725409.

[3] Rahimi E, Rabiee A, Aghaei J, Muttaqi KM, Esmaeel Nezhad A. On the management of wind power intermittency. Renewable and Sustainable Energy Reviews 2013;28:643–53. https://doi.org/10.1016/j.rser.2013.08.034.

[4] Ren G, Wan J, Liu J, Yu D, Söder L. Analysis of wind power intermittency based on historical wind power data. Energy 2018;150:482–92. https://doi.org/10.1016/j.energy.2018.02.142.

[5] Luo Z, Wang X, Wen H, Pei A. Hydrogen production from offshore wind power in South China. International Journal of Hydrogen Energy 2022;47:24558–68. https://doi.org/10.1016/j.ijhydene.2022.03.162.

[6] Rosen MA, Koohi-Fayegh S. The prospects for hydrogen as an energy carrier: an overview of hydrogen energy and hydrogen energy systems. Energy, Ecology and Environment 2016;1:10–29. https://doi.org/10.1007/s40974-016-0005-z.

[7] Sharaf OZ, Orhan MF. An overview of fuel cell technology: Fundamentals and applications. Renewable and Sustainable Energy Reviews 2014;32:810–53. https://doi.org/10.1016/j.rser.2014.01.012.

[8] Li Z, Zhang H, Xu H, Xuan J. Advancing the multiscale understanding on solid oxide electrolysis cells via modelling approaches: A review. Renewable and Sustainable Energy Reviews 2021;141:110863. https://doi.org/10.1016/j.rser.2021.110863.

[9] Hu L, Lindbergh G, Lagergren C. Performance and Durability of the Molten Carbonate Electrolysis Cell and the Reversible Molten Carbonate Fuel Cell. J Phys Chem C 2016;120:13427–33. https://doi.org/10.1021/acs.jpcc.6b04417.

[10] Wu H, Li Z, Ji D, Liu Y, Li L, Yuan D, et al. One-pot synthesis of nanostructured carbon materials from carbon dioxide via electrolysis in molten carbonate salts. Carbon 2016;106:208–17. https://doi.org/10.1016/j.carbon.2016.05.031.

[11] Coors WG. Protonic ceramic fuel cells for high-efficiency operation with methane. Journal of Power Sources 2003;118:150–6. https://doi.org/10.1016/S0378-7753(03)00072-7.

[12] Ji H-I, Lee J-H, Son J-W, Yoon KJ, Yang S, Kim B-K. Protonic ceramic electrolysis cells for fuel production: a brief review. Journal of the Korean Ceramic Society 2020;57:480–94. https://doi.org/10.1007/s43207-020-00059-4.

[13] Medvedev D. Trends in research and development of protonic ceramic electrolysis cells. International Journal of Hydrogen Energy 2019;44:26711–40. https://doi.org/10.1016/j.ijhydene.2019.08.130.

[14] Lei L, Zhang J, Yuan Z, Liu J, Ni M, Chen F. Progress Report on Proton Conducting Solid Oxide Electrolysis Cells. Adv Funct Mater 2019;29:1903805. https://doi.org/10.1002/adfm.201903805.

[15] Yao P, Yu H, Ding Z, Liu Y, Lu J, Lavorgna M, et al. Review on Polymer-Based Composite Electrolytes for Lithium Batteries. Front Chem 2019;7:522. https://doi.org/10.3389/fchem.2019.00522.

[16] Zhang W, Hu YH. Progress in proton-conducting oxides as electrolytes for low-temperature solid oxide fuel cells: From materials to devices. Energy Science & Engineering 2021;9:984–1011. https://doi.org/10.1002/ese3.886.

[17] Bello IT, Zhai S, He Q, Cheng C, Dai Y, Chen B, et al. Materials development and prospective for protonic ceramic fuel cells. International Journal of Energy Research 2022;46:2212–40. https://doi.org/10.1002/er.7371.

[18] Guan D, Wang B, Zhang J, Shi R, Jiao K, Li L, et al. Hydrogen society: from present to future. Energy & Environmental Science 2023. https://doi.org/10.1039/D3EE02695G.

[19] Matsui T, Kishida R, Kim J-Y, Muroyama H, Eguchi K. Performance Deterioration of Ni–YSZ Anode Induced by Electrochemically Generated Steam in Solid Oxide Fuel Cells. J Electrochem Soc 2010;157:B776. https://doi.org/10.1149/1.3336830.

[20] Wu W, Ding H, Zhang Y, Ding Y, Katiyar P, Majumdar PK, et al. 3D Self-Architectured Steam Electrode Enabled Efficient and Durable Hydrogen Production in a Proton-Conducting Solid Oxide Electrolysis Cell at Temperatures Lower Than 600 °C. Advanced Science 2018;5:1800360. https://doi.org/10.1002/advs.201800360.

[21] Chen K, Jiang SP. Review—Materials Degradation of Solid Oxide Electrolysis Cells. J Electrochem Soc 2016;163:F3070. https://doi.org/10.1149/2.0101611jes.

[22] Monaco F, Hubert M, Vulliet J, Montinaro D, Ouweltjes JP, Cloetens P, et al. Impact of Microstructure and Polarization on the Degradation of Ni-YSZ Electrode: An Experimental and Modeling Approach. ECS Trans 2019;91:653. https://doi.org/10.1149/09101.0653ecst.

[23] Lay-Grindler E, Laurencin J, Villanova J, Cloetens P, Bleuet P, Mansuy A, et al. Degradation study by 3D reconstruction of a nickel–yttria stabilized zirconia cathode after high temperature steam electrolysis operation. Journal of Power Sources 2014;269:927–36. https://doi.org/10.1016/j.jpowsour.2014.07.066.

[24] Yu J, Men HJ, Qu YM, Tian N. Performance of Ni-Fe bimetal based cathode for intermediate temperature solid oxide electrolysis cell. Solid State Ionics 2020;346:115203. https://doi.org/10.1016/j.ssi.2019.115203.

[25] Li N, Keane M, Mahapatra MK, Singh P. Mitigation of the delamination of LSM anode in solid oxide electrolysis cells using manganese-modified YSZ. International Journal of Hydrogen Energy 2013;38:6298–303. https://doi.org/10.1016/j.ijhydene.2013.03.036.

[26] Keane M, Mahapatra MK, Verma A, Singh P. LSM–YSZ interactions and anode delamination in solid oxide electrolysis cells. International Journal of Hydrogen Energy 2012;37:16776–85. https://doi.org/10.1016/j.ijhydene.2012.08.104.

[27] Khan MS, Xu X, Knibbe R, Rehman A ur, Li Z, Yago AJ, et al. New Insights into the Degradation Behavior of Air Electrodes during Solid Oxide Electrolysis and Reversible Solid Oxide Cell Operation. Energy Technology 2020;8:2000241. https://doi.org/10.1002/ente.202000241.

[28] Ma L, Priya P, Aluru NR. A Multiscale Model for Electrochemical Reactions in LSCF Based Solid Oxide Cells. J Electrochem Soc 2018;165:F1232. https://doi.org/10.1149/2.0921814jes.

[29] Virkar AV. Mechanism of oxygen electrode delamination in solid oxide electrolyzer cells. International Journal of Hydrogen Energy 2010;35:9527–43. https://doi.org/10.1016/j.ijhydene.2010.06.058.

[30] Zhang Y, Chen K, Xia C, Jiang SP, Ni M. A model for the delamination kinetics of La0.8Sr0.2MnO3 oxygen electrodes of solid oxide electrolysis cells. International Journal of Hydrogen Energy 2012;37:13914–20. https://doi.org/10.1016/j.ijhydene.2012.07.062.

[31] Sohal MS, O'Brien JE, Stoots CM, Hartvigsen JJ, Larsen D, Elangovan S, et al. Critical Causes of Degradation in Integrated Laboratory Scale Cells during High Temperature Electrolysis. Idaho National Lab; 2009. https://doi.org/10.2172/961923.

[32] Vøllestad E, Strandbakke R, Tarach M, Catalán-Martínez D, Fontaine M-L, Beeaff D, et al. Mixed proton and electron conducting double perovskite anodes for stable and efficient

tubular proton ceramic electrolysers. Nature Materials 2019;18:752–9. https://doi.org/10.1038/s41563-019-0388-2.

[33] Duan C, Kee R, Zhu H, Sullivan N, Zhu L, Bian L, et al. Highly efficient reversible protonic ceramic electrochemical cells for power generation and fuel production. Nature Energy 2019;4:230–40. https://doi.org/10.1038/s41560-019-0333-2.

[34] Ren R, Sun J, Wang G, Xu C, Qiao J, Sun W, et al. Rational design of Sr2Fe1.5Mo0.4Y0.1O6-δ oxygen electrode with triple conduction for hydrogen production in protonic ceramic electrolysis cell. Separation and Purification Technology 2022;299:121780. https://doi.org/10.1016/j.seppur.2022.121780.

[35] Choi S, C. Davenport T, M. Haile S. Protonic ceramic electrochemical cells for hydrogen production and electricity generation: exceptional reversibility, stability, and demonstrated faradaic efficiency. Energy & Environmental Science 2019;12:206–15. https://doi.org/10.1039/C8EE02865F.

[36] Zhou Y, Liu E, Chen Y, Liu Y, Zhang L, Zhang W, et al. An Active and Robust Air Electrode for Reversible Protonic Ceramic Electrochemical Cells. ACS Energy Letters 2021;6:1511–20. https://doi.org/10.1021/acsenergylett.1c00432.

[37] Ding H, Wu W, Jiang C, Ding Y, Bian W, Hu B, et al. Self-sustainable protonic ceramic electrochemical cells using a triple conducting electrode for hydrogen and power production. Nature Communications 2020;11:1907. https://doi.org/10.1038/s41467-020-15677-z.

[38] Ruiz Diaz DF, Valenzuela E, Wang Y. A component-level model of polymer electrolyte membrane electrolysis cells for hydrogen production. Applied Energy 2022;321:119398. https://doi.org/10.1016/j.apenergy.2022.119398.

[39] Yang G, Yu S, Kang Z, Dohrmann Y, Bender G, Pivovar BS, et al. A novel PEMEC with 3D printed non-conductive bipolar plate for low-cost hydrogen production from water

electrolysis. Energy Conversion and Management 2019;182:108–16. https://doi.org/10.1016/j.enconman.2018.12.046.

[40] Shi H, Su C, Ran R, Cao J, Shao Z. Electrolyte materials for intermediate-temperature solid oxide fuel cells. Progress in Natural Science: Materials International 2020;30:764–74. https://doi.org/10.1016/j.pnsc.2020.09.003.

[41] Chen M, Chen D, Wang K, Xu Q. Densification and electrical conducting behavior of BaZr0.9Y0.1O3-δ proton conducting ceramics with NiO additive. Journal of Alloys and Compounds 2019;781:857–65. https://doi.org/10.1016/j.jallcom.2018.12.090.

[42] Shimada H, Yamaguchi T, Sumi H, Yamaguchi Y, Nomura K, Mizutani Y, et al. A key for achieving higher open-circuit voltage in protonic ceramic fuel cells: lowering interfacial electrode polarization. ACS Applied Energy Materials 2018;2:587–97. https://doi.org/10.1021/acsaem.8b01617.

[43] Tsvetkov D, Ivanov I, Malyshkin D, Sereda V, Zuev A. Thermoelectric Behavior of BaZr0.9Y0.1O3−d Proton Conducting Electrolyte. Membranes 2019;9:120. https://doi.org/10.3390/membranes9090120.

[44] Kreuer KD. On the development of proton conducting materials for technological applications. Solid State Ionics 1997;97:1–15. https://doi.org/10.1016/S0167-2738(97)00082-9.

[45] Kreuer KD. On the development of proton conducting polymer membranes for hydrogen and methanol fuel cells. Journal of Membrane Science 2001;185:29–39. https://doi.org/10.1016/S0376-7388(00)00632-3.

[46] Kreuer KD. Proton-Conducting Oxides. Annu Rev Mater Res 2003;33:333–59. https://doi.org/10.1146/annurev.matsci.33.022802.091825.

[47] Kim J, Sengodan S, Kim S, Kwon O, Bu Y, Kim G. Proton conducting oxides: A review of materials and applications for renewable energy conversion and storage. Renewable

and Sustainable Energy Reviews 2019;109:606–18. https://doi.org/10.1016/j.rser.2019.04.042.

[48] Han D, Toyoura K, Uda T. Protonated BaZr0.8Y0.2O3−δ: Impact of Hydration on Electrochemical Conductivity and Local Crystal Structure. ACS Appl Energy Mater 2021;4:1666–76. https://doi.org/10.1021/acsaem.0c02832.

[49] Chen M, Zhou M, Liu Z, Liu J. A comparative investigation on protonic ceramic fuel cell electrolytes BaZr0.8Y0.2O3-δ and BaZr0.1Ce0.7Y0.2O3-δ with NiO as sintering aid. Ceramics International 2022;48:17208–16. https://doi.org/10.1016/j.ceramint.2022.02.278.

[50] Guo Y, Lin Y, Ran R, Shao Z. Zirconium doping effect on the performance of proton-conducting BaZryCe0.8−yY0.2O3−δ (0.0≤y≤0.8) for fuel cell applications. Journal of Power Sources 2009;193:400–7. https://doi.org/10.1016/j.jpowsour.2009.03.044.

[51] Xiao J, Sun W, Zhu Z, Tao Z, Liu W. Fabrication and characterization of anode-supported dense BaZr0.8Y0.2O3−δ electrolyte membranes by a dip-coating process. Materials Letters 2012;73:198–201. https://doi.org/10.1016/j.matlet.2012.01.032.

[52] Lei L, Zhang J, Guan R, Liu J, Chen F, Tao Z. Energy storage and hydrogen production by proton conducting solid oxide electrolysis cells with a novel heterogeneous design. Energy Conversion and Management 2020;218:113044. https://doi.org/10.1016/j.enconman.2020.113044.

[53] Matsuo H, Nakane K, Matsuzaki Y, Otomo J. Effect of lanthanum tungstate hole-blocking layer for improvement of energy efficiency in anode-supported protonic ceramic fuel cells. Journal of the Ceramic Society of Japan 2021;129:147–53. https://doi.org/10.2109/jcersj2.20204.

[54] Matsuo H, Nakane K, Matsuzaki Y, Otomo J. Improvement of Energy Efficiency in Anode-Supported Proton Ceramic Fuel Cells By Lanthanum Tungstate Hole Blocking

Layer. Meet Abstr 2020;MA2020-02:2634. https://doi.org/10.1149/MA2020-02402634mtgabs.

[55] Matsuzaki Y, Tachikawa Y, Baba Y, Sato K, Iinuma H, Kojo G, et al. Leakage Current and Chemical Potential Profile in Proton-Conducting Bi-Layered Solid Oxide Electrolyte with BZY and Hole-Blocking Layers. ECS Trans 2019;91:1009. https://doi.org/10.1149/09101.1009ecst.

[56] Jin X, Shoukry Y. Current Leakage and Faradaic Efficiency Simulation of Proton-Conducting Solid Oxide Electrolysis Cells. ECS Transactions 2023;111:1159. https://doi.org/10.1149/11106.1159ecst.

[57] Ni M, Leung MKH, Leung DYC. Electrochemical modeling of hydrogen production by proton-conducting solid oxide steam electrolyzer. International Journal of Hydrogen Energy 2008;33:4040–7. https://doi.org/10.1016/j.ijhydene.2008.05.065.

[58] Dumortier M, Sanchez J, Keddam M, Lacroix O. Theoretical considerations on the modelling of transport in a three-phase electrode and application to a proton conducting solid oxide electrolysis cell. International Journal of Hydrogen Energy 2012;37:11579–94. https://doi.org/10.1016/j.ijhydene.2012.05.023.

[59] Chen B, Xu H, Sun Q, Zhang H, Tan P, Cai W, et al. Syngas/power cogeneration from proton conducting solid oxide fuel cells assisted by dry methane reforming: A thermal-electrochemical modelling study. Energy Conversion and Management 2018;167:37–44. https://doi.org/10.1016/j.enconman.2018.04.078.

[60] Zhang J-H, Lei L-B, Liu D, Zhao F-Y, Ni M, Chen F. Mathematical modeling of a proton-conducting solid oxide fuel cell with current leakage. Journal of Power Sources 2018;400:333–40. https://doi.org/10.1016/j.jpowsour.2018.08.038.

[61] Kee RJ, Zhu H, Hildenbrand BW, Vøllestad E, Sanders MD, O'Hayre RP. Modeling the Steady-State and Transient Response of Polarized and Non-Polarized Proton-Conducting

Doped-Perovskite Membranes. J Electrochem Soc 2013;160:F290. https://doi.org/10.1149/2.016304jes.

[62] Zhu H, Kee RJ. Membrane polarization in mixed-conducting ceramic fuel cells and electrolyzers. International Journal of Hydrogen Energy 2016;41:2931–43. https://doi.org/10.1016/j.ijhydene.2015.10.100.

[63] Zhu H, Ricote S, Duan C, O'Hayre RP, Kee RJ. Defect Chemistry and Transport within Dense BaCe0.7Zr0.1Y0.1Yb0.1O3 − δ (BCZYYb) Proton-Conducting Membranes. Journal of The Electrochemical Society 2018;165:F845. https://doi.org/10.1149/2.1091810jes.

[64] Priya P, Aluru NR. A multiscale framework to predict electrochemical characteristics of yttrium doped Barium Zirconate based solid oxide cells. Journal of Power Sources 2021;481:228969. https://doi.org/10.1016/j.jpowsour.2020.228969.

[65] Putilov LP, Tsidilkovski VI. Improving the performance of protonic ceramic fuel cells and electrolyzers: The role of acceptor impurities in oxide membranes. Energy Conversion and Management 2022;267:115826. https://doi.org/10.1016/j.enconman.2022.115826.

[66] Virkar AV. Transport through mixed proton, oxygen ion and electron (hole) conductors: Goldman–Hodgkin–Katz-type equation. Journal of Power Sources 2009;194:753–62. https://doi.org/10.1016/j.jpowsour.2009.06.007.

[67] Ortiz-Corrales JA, Matsuo H, Otomo J. Design and Modeling of Proton-Conducting Bilayer Electrolytes Using a Nernst-Planck-Poisson Formulation. ECS Transactions 2021;103:1763. https://doi.org/10.1149/10301.1763ecst.

[68] Otomo J, Yamate S, Ortiz-Corrales JA. Bilayer Cell Model and System Design of Highly Efficient Protonic Ceramic Fuel Cells. ECS Transactions 2023;111:1075. https://doi.org/10.1149/11106.1075ecst.

[69] Lei L, Mo Y, Huang Y, Qiu R, Tian Z, Wang J, et al. Revealing and quantifying the role of oxygen-ionic current in proton-conducting solid oxide fuel cells: A modeling study. Energy 2023;276:127575. https://doi.org/10.1016/j.energy.2023.127575.

[70] Dhanasekaran A, Subramanian Y, Omeiza LA, Raj V, Yassin HPHM, Sa MA, et al. Computational Fluid Dynamics for Protonic Ceramic Fuel Cell Stack Modeling: A Brief Review. Energies 2023;16:208. https://doi.org/10.3390/en16010208.

[71] Putilov LP, Tsidilkovski VI, Demin AK. Revealing the effect of the cell voltage and external conditions on the characteristics of protonic ceramic fuel cells. Journal of Materials Chemistry A 2020;8:12641–56. https://doi.org/10.1039/D0TA03935G.

[72] Zhu H, Ricote S, Duan C, O'Hayre RP, Tsvetkov DS, Kee RJ. Defect Incorporation and Transport within Dense BaZr0.8Y0.2O3−δ (BZY20) Proton-Conducting Membranes. Journal of The Electrochemical Society 2018;165:F581. https://doi.org/10.1149/2.0161809jes.

[73] Xu H, Ma J, Tan P, Chen B, Wu Z, Zhang Y, et al. Towards online optimisation of solid oxide fuel cell performance: Combining deep learning with multi-physics simulation. Energy and AI 2020;1:100003. https://doi.org/10.1016/j.egyai.2020.100003.

[74] Subotić V, Eibl M, Hochenauer C. Artificial intelligence for time-efficient prediction and optimization of solid oxide fuel cell performances. Energy Conversion and Management 2021;230:113764. https://doi.org/10.1016/j.enconman.2020.113764.

[75] Cheng S-J, Li W-K, Chang T-J, Hsu C-H. Data-Driven Prognostics of the SOFC System Based on Dynamic Neural Network Models. Energies 2021;14:5841. https://doi.org/10.3390/en14185841.

[76] Xu H, Ma J, Tan P, Wu Z, Zhang Y, Ni M, et al. Enabling thermal-neutral electrolysis for CO2-to-fuel conversions with a hybrid deep learning strategy. Energy Conversion and Management 2021;230:113827. https://doi.org/10.1016/j.enconman.2021.113827.

[77] Ding R, Yin W, Cheng G, Chen Y, Wang J, Wang R, et al. Boosting the optimization of membrane electrode assembly in proton exchange membrane fuel cells guided by explainable artificial intelligence. Energy and AI 2021;5:100098. https://doi.org/10.1016/j.egyai.2021.100098.

[78] Ding R, Zhang S, Chen Y, Rui Z, Hua K, Wu Y, et al. Application of Machine Learning in Optimizing Proton Exchange Membrane Fuel Cells: A Review. Energy and AI 2022;9:100170. https://doi.org/10.1016/j.egyai.2022.100170.

[79] İskenderoğlu FC, Baltacioğlu MK, Demir MH, Baldinelli A, Barelli L, Bidini G. Comparison of support vector regression and random forest algorithms for estimating the SOFC output voltage by considering hydrogen flow rates. International Journal of Hydrogen Energy 2020;45:35023–38. https://doi.org/10.1016/j.ijhydene.2020.07.265.

[80] Chen J, Sun S, Chen Y, Zhang H, Lu Z. Study on Model Evolution Method Based on the Hybrid Modeling Technology With Support Vector Machine for an SOFC-GT System. Journal of Electrochemical Energy Conversion and Storage 2022;20. https://doi.org/10.1115/1.4054847.

[81] Ming W, Sun P, Zhang Z, Qiu W, Du J, Li X, et al. A systematic review of machine learning methods applied to fuel cells in performance evaluation, durability prediction, and application monitoring. International Journal of Hydrogen Energy 2023;48:5197–228. https://doi.org/10.1016/j.ijhydene.2022.10.261.

[82] Su D, Zheng J, Ma J, Dong Z, Chen Z, Qin Y. Application of Machine Learning in Fuel Cell Research. Energies 2023;16:4390. https://doi.org/10.3390/en16114390.

[83] Han I-S, Chung C-B. Performance prediction and analysis of a PEM fuel cell operating on pure oxygen using data-driven models: A comparison of artificial neural network and support vector machine. International Journal of Hydrogen Energy 2016;41:10202–11. https://doi.org/10.1016/j.ijhydene.2016.04.247.

[84] Chauhan V, Mortazavi M, Benner JZ, Santamaria AD. Two-phase flow characterization in PEM fuel cells using machine learning. Energy Reports 2020;6:2713–9. https://doi.org/10.1016/j.egyr.2020.09.037.

[85] Legala A, Zhao J, Li X. Machine learning modeling for proton exchange membrane fuel cell performance. Energy and AI 2022;10:100183. https://doi.org/10.1016/j.egyai.2022.100183.

[86] Song S, Xiong X, Wu X, Xue Z. Modeling the SOFC by BP neural network algorithm. International Journal of Hydrogen Energy 2021;46:20065–77. https://doi.org/10.1016/j.ijhydene.2021.03.132.

[87] Ramadhani F, Hussain MA, Mokhlis H, Hajimolana S. Optimization strategies for Solid Oxide Fuel Cell (SOFC) application: A literature survey. Renewable and Sustainable Energy Reviews 2017;76:460–84. https://doi.org/10.1016/j.rser.2017.03.052.

[88] Cui Y, Geng Z, Zhu Q, Han Y. Review: Multi-objective optimization methods and application in energy saving. Energy 2017;125:681–704. https://doi.org/10.1016/j.energy.2017.02.174.

[89] Ru N, Jianhua Y. A GA and Particle Swarm Optimization based hybrid algorithm. 2008 IEEE Congress on Evolutionary Computation (IEEE World Congress on Computational Intelligence), 2008, p. 1047–50. https://doi.org/10.1109/CEC.2008.4630925.

[90] Wang D, Tan D, Liu L. Particle swarm optimization algorithm: an overview. Soft Computing 2018;22:387–408. https://doi.org/10.1007/s00500-016-2474-6.

[91] Safari S, Hajilounezhad T, Ehyaei MA. Multi-objective optimization of solid oxide fuel cell/gas turbine combined heat and power system: A comparison between particle swarm and genetic algorithms. International Journal of Energy Research 2020;44:9001–20. https://doi.org/10.1002/er.5610.

[92] Han D, Hatada N, Uda T. Chemical Expansion of Yttrium-Doped Barium Zirconate and Correlation with Proton Concentration and Conductivity. Journal of the American Ceramic Society 2016;99:3745–53. https://doi.org/10.1111/jace.14377.

[93] Eisele S, M. Draber F, Grieshammer S. The effect of ionic defect interactions on the hydration of yttrium-doped barium zirconate. Physical Chemistry Chemical Physics 2021;23:4882–91. https://doi.org/10.1039/D0CP06587K.

[94] Chen T, Jing Y, Anderson LO, Leonard K, Matsumoto H, Aluru N, et al. Toward Durable Protonic Ceramic Cells: Hydration-Induced Chemical Expansion Correlates with Symmetry in the Y-Doped BaZrO3–BaCeO3 Solid Solution. The Journal of Physical Chemistry C 2021;125:26216–28. https://doi.org/10.1021/acs.jpcc.1c08334.

[95] Zvonareva I, Fu X-Z, Medvedev D, Shao Z. Electrochemistry and energy conversion features of protonic ceramic cells with mixed ionic-electronic electrolytes. Energy & Environmental Science 2022;15:439–65. https://doi.org/10.1039/D1EE03109K.

[96] Zvonareva IA, Starostin GN, Akopian MT, Murashkina AA, Fu X-Z, Medvedev DA. Thermal and chemical expansion behavior of hydrated barium stannate materials. Ceramics International 2023;49:21923–31. https://doi.org/10.1016/j.ceramint.2023.04.016.

[97] Bishop SR, Duncan KL, Wachsman ED. Defect equilibria and chemical expansion in non-stoichiometric undoped and gadolinium-doped cerium oxide. Electrochimica Acta 2009;54:1436–43. https://doi.org/10.1016/j.electacta.2008.09.026.

[98] Cui T, Xiao G, Yan H, Zhang Y, Wang J-Q. Numerical simulation and analysis of the thermal stresses of a planar solid oxide electrolysis cell. International Journal of Green Energy 2023;20:432–44. https://doi.org/10.1080/15435075.2022.2065881.

[99] Han Y, Guo M, Sun A, Liu H, Xiao G, Sun Y, et al. Towards feasible temperature management and thermo-mechanical stability of carbon-assisted solid oxide electrolysis

cell. Energy Conversion and Management 2023;276:116483. https://doi.org/10.1016/j.enconman.2022.116483.

[100] Sun Y, Hu X, Gao J, Han Y, Sun A, Zheng N, et al. Solid oxide electrolysis cell under real fluctuating power supply with a focus on thermal stress analysis. Energy 2022;261:125096. https://doi.org/10.1016/j.energy.2022.125096.

[101] Jin X, Huang K. Mechanistic Understanding of OER Degradation of SOEC through Computational Modeling. ECS Meeting Abstracts 2020;MA2020-01:1791–1791. https://doi.org/10.1149/MA2020-01401791mtgabs.

[102] Wang Y, Virkar AV, Khonsari MM, Zhou X-D. Theoretical Analysis of Critical Conditions for Crack Formation and Propagation, and Optimal Operation of SOECs. Journal of The Electrochemical Society 2022;169:044529. https://doi.org/10.1149/1945-7111/ac5fee.

[103] Bao J, Karri N, Recknagle K, Wang C, Koeppel B, Marina OA. Modeling Framework to Analyze Performance and Structural Reliability of Solid Oxide Electrolysis Cells. Journal of The Electrochemical Society 2022;169:054523. https://doi.org/10.1149/1945-7111/ac6f87.

[104] Zhu S, Wang Y, Rao Y, Zhan Z, Xia C. Chemically-induced mechanical unstability of samaria-doped ceria electrolyte for solid oxide electrolysis cells. International Journal of Hydrogen Energy 2014;39:12440–7. https://doi.org/10.1016/j.ijhydene.2014.06.051.

[105] Lenser C, Zhang J, Russner N, Weber A, Guillon O, Menzler NH. Electro-chemo-mechanical analysis of a solid oxide cell based on doped ceria. Journal of Power Sources 2022;541:231505. https://doi.org/10.1016/j.jpowsour.2022.231505.

[106] Terada K, Kawada T, Sato K, Iguchi F, Yashiro K, Amezawa K, et al. Multiscale Simulation of Electro-Chemo-Mechanical Coupling Behavior of PEN Structure under SOFC Operation. ECS Transactions 2011;35:923. https://doi.org/10.1149/1.3570073.

[107] Swaminathan N, Qu J, Sun Y. An electrochemomechanical theory of defects in ionic solids. I. Theory. Philosophical Magazine 2007;87:1705–21. https://doi.org/10.1080/14786430601102973.

[108] Costamagna P, Costa P, Antonucci V. Micro-modelling of solid oxide fuel cell electrodes. Electrochimica Acta 1998;43:375–94. https://doi.org/10.1016/S0013-4686(97)00063-7.

[109] Chen D, Lin Z, Zhu H, Kee RJ. Percolation theory to predict effective properties of solid oxide fuel-cell composite electrodes. Journal of Power Sources 2009;191:240–52. https://doi.org/10.1016/j.jpowsour.2009.02.051.

[110] Suzuki M, Oshima T. Estimation of the co-ordination number in a multi-component mixture of spheres. Powder Technology 1983;35:159–66. https://doi.org/10.1016/0032-5910(83)87004-1.

[111] Shi J, Xue X. CFD analysis of a symmetrical planar SOFC with heterogeneous electrode properties. Electrochimica Acta 2010;55:5263–73. https://doi.org/10.1016/j.electacta.2010.04.060.

[112] Bouvard D, Lange FF. Relation between percolation and particle coordination in binary powder mixtures. Acta Metallurgica et Materialia 1991;39:3083–90. https://doi.org/10.1016/0956-7151(91)90041-X.

[113] Wang H, Wang X, Meng B, Tan X, Loh KS, Sunarso J, et al. Perovskite-based mixed protonic–electronic conducting membranes for hydrogen separation: Recent status and advances. Journal of Industrial and Engineering Chemistry 2018;60:297–306. https://doi.org/10.1016/j.jiec.2017.11.016.

[114] Chen D, Zhang Q, Lu L, Periasamy V, Tade MO, Shao Z. Multi scale and physics models for intermediate and low temperatures H+-solid oxide fuel cells with H+/e−/O2− mixed conducting properties: Part A, generalized percolation theory for LSCF-SDC-

BZCY 3-component cathodes. Journal of Power Sources 2016;303:305–16. https://doi.org/10.1016/j.jpowsour.2015.10.090.

[115] Beale SB, Andersson M, Boigues-Muñoz C, Frandsen HL, Lin Z, McPhail SJ, et al. Continuum scale modelling and complementary experimentation of solid oxide cells. Progress in Energy and Combustion Science 2021;85:100902. https://doi.org/10.1016/j.pecs.2020.100902.

[116] Kong W, Li J, Liu S, Lin Z. The influence of interconnect ribs on the performance of planar solid oxide fuel cell and formulae for optimal rib sizes. Journal of Power Sources 2012;204:106–15. https://doi.org/10.1016/j.jpowsour.2012.01.041.

[117] Li K, Araki T, Kawamura T, Ota A, Okuyama Y. Numerical analysis of current efficiency distributions in a protonic ceramic fuel cell using Nernst-Planck-Poisson model. International Journal of Hydrogen Energy 2020;45:34139–49. https://doi.org/10.1016/j.ijhydene.2020.09.143.

[118] Peters C. Grain-size Effects in Nanoscaled Electrolyte and Cathode Thin Films for Solid Oxide Fuel Cells (SOFC). KIT Scientific Publishing; 2009.

[119] Luo Y, Shi Y, Liao S, Chen C, Zhan Y, Au C-T, et al. Coupling ammonia catalytic decomposition and electrochemical oxidation for solid oxide fuel cells: A model based on elementary reaction kinetics. Journal of Power Sources 2019;423:125–36. https://doi.org/10.1016/j.jpowsour.2019.03.064.

[120] Su H, Hu YH. Degradation issues and stabilization strategies of protonic ceramic electrolysis cells for steam electrolysis. Energy Science & Engineering 2022;10:1706–25. https://doi.org/10.1002/ese3.1010.

[121] Xu Q, Xia L, He Q, Guo Z, Ni M. Thermo-electrochemical modelling of high temperature methanol-fuelled solid oxide fuel cells. Applied Energy 2021;291:116832. https://doi.org/10.1016/j.apenergy.2021.116832.

[122] Xu Q, Guo M, Xia L, Li Z, He Q, Zhao D, et al. Temperature Gradient Analyses of a Tubular Solid Oxide Fuel Cell Fueled by Methanol. Transactions of Tianjin University 2023;29:14–30. https://doi.org/10.1007/s12209-022-00331-0.

[123] Błesznowski M, Sikora M, Kupecki J, Makowski Ł, Orciuch W. Mathematical approaches to modelling the mass transfer process in solid oxide fuel cell anode. Energy 2022;239:121878. https://doi.org/doi.org/10.1016/j.energy.2021.121878.

[124] Kong W, Zhu H, Fei Z, Lin Z. A modified dusty gas model in the form of a Fick's model for the prediction of multicomponent mass transport in a solid oxide fuel cell anode. Journal of Power Sources 2012;206:171–8. https://doi.org/10.1016/j.jpowsour.2012.01.107.

[125] Jiang Y, Virkar A V. Fuel composition and diluent effect on gas transport and performance of anode-supported SOFCs. Journal of the Electrochemical Society 2003;150:A942. https://doi.org/doi.org/10.1149/1.1579480.

[126] Poling BE, Prausnitz JM, O'connell JP, others. The properties of gases and liquids. vol. 5. Mcgraw-hill New York; 2001.

[127] Brokaw RS. Predicting transport properties of dilute gases. Industrial & Engineering Chemistry Process Design and Development 1969;8:240–53. https://doi.org/doi.org/10.1021/i260030a015.

[128] Wilke CR, Chang P. Correlation of diffusion coefficients in dilute solutions. AIChE Journal 1955;1:264–70. https://doi.org/doi.org/10.1002/aic.690010222.

[129] Neufeld PD, Janzen AR, Aziz R. Empirical equations to calculate 16 of the transport collision integrals Ω(l, s)* for the Lennard-Jones (12-6) potential. The Journal of Chemical Physics 1972;57:1100–2. https://doi.org/doi.org/10.1063/1.1678363.

[130] Celik AN. Three-dimensional multiphysics model of a planar solid oxide fuel cell using computational fluid dynamics approach. International Journal of Hydrogen Energy 2018;43:19730–48. https://doi.org/10.1016/j.ijhydene.2018.08.212.

[131] Andersson M, Paradis H, Yuan J, Sundén B. Three dimensional modeling of an solid oxide fuel cell coupling charge transfer phenomena with transport processes and heat generation. Electrochimica Acta 2013;109:881–93. https://doi.org/10.1016/j.electacta.2013.08.018.

[132] Li Z, He Q, Xia L, Xu Q, Cheng C, Wang J, et al. Effects of cathode thickness and microstructural properties on the performance of protonic ceramic fuel cell (PCFC): A 3D modelling study. International Journal of Hydrogen Energy 2021. https://doi.org/doi.org/10.1016/j.ijhydene.2021.11.022.

[133] Guo M, Xiao G, Wang J, Lin Z. Parametric study of kW-class solid oxide fuel cell stacks fueled by hydrogen and methane with fully multiphysical coupling model. International Journal of Hydrogen Energy 2021;46:9488–502. https://doi.org/10.1016/j.ijhydene.2020.12.092.

[134] Guo M, Ru X, Yang L, Ni M, Lin Z. Effects of methane steam reforming on the mechanical stability of solid oxide fuel cell stack. Applied Energy 2022;322:119464. https://doi.org/10.1016/j.apenergy.2022.119464.

[135] Yang S, Lu Y, Liu B, Che Q, Wang F. Modeling of cooperative defect transport and thermal mismatch in a planar solid oxide fuel cell. International Journal of Hydrogen Energy 2023;48:12461–73. https://doi.org/10.1016/j.ijhydene.2022.12.107.

[136] Hashin Z, Shtrikman S. A variational approach to the theory of the elastic behaviour of multiphase materials. Journal of the Mechanics and Physics of Solids 1963;11:127–40. https://doi.org/10.1016/0022-5096(63)90060-7.

[137] Kong W, Zhang W, Zhang S, Zhang Q, Su S. Residual stress analysis of a micro-tubular solid oxide fuel cell. International Journal of Hydrogen Energy 2016;41:16173–80. https://doi.org/10.1016/j.ijhydene.2016.05.256.

[138] Freddi A, Salmon M. Design Principles and Methodologies: From Conceptualization to First Prototyping with Examples and Case Studies. Springer International Publishing; 2019. https://doi.org/10.1007/978-3-319-95342-7.

[139] Devore JL, Farnum NR, Doi J. Applied statistics for engineers and scientists. 3rd ed. Stamford, CT: Cengage Learning; 2014.

[140] Antony J. Design of experiments for engineers and scientists. 2nd edition. London: Elsevier; 2014.

[141] Niri MF, Liu K, Apachitei G, Román-Ramírez LAA, Lain M, Widanage D, et al. Quantifying key factors for optimised manufacturing of Li-ion battery anode and cathode via artificial intelligence. Energy and AI 2022;7:100129. https://doi.org/10.1016/j.egyai.2021.100129.

[142] Wang J, Jiang H, Chen G, Wang H, Lu L, Liu J, et al. Integration of multi-physics and machine learning-based surrogate modelling approaches for multi-objective optimization of deformed GDL of PEM fuel cells. Energy and AI 2023;14:100261. https://doi.org/10.1016/j.egyai.2023.100261.

[143] Samek W, Montavon G, Lapuschkin S, Anders CJ, Muller K-R. Explaining Deep Neural Networks and Beyond: A Review of Methods and Applications. Proc IEEE 2021;109:247–78. https://doi.org/10.1109/JPROC.2021.3060483.

[144] Gullì A, Pal S. Deep learning with Keras: implement neural networks with Keras on Theano and TensorFlow. Birmingham Mumbai: Packt Publishing; 2017.

[145] Chicco D, Warrens MJ, Jurman G. The coefficient of determination R-squared is more informative than SMAPE, MAE, MAPE, MSE and RMSE in regression analysis evaluation. PeerJ Computer Science 2021;7:e623. https://doi.org/10.7717/peerj-cs.623.

[146] Shao Q, Gao E, Mara T, Hu H, Liu T, Makradi A. Global sensitivity analysis of solid oxide fuel cells with Bayesian sparse polynomial chaos expansions. Applied Energy 2020;260:114318. https://doi.org/10.1016/j.apenergy.2019.114318.

[147] Nossent J, Elsen P, Bauwens W. Sobol' sensitivity analysis of a complex environmental model. Environmental Modelling & Software 2011;26:1515–25. https://doi.org/10.1016/j.envsoft.2011.08.010.

[148] Tarutin A, Kasyanova A, Lyagaeva J, Vdovin G, Medvedev D. Towards high-performance tubular-type protonic ceramic electrolysis cells with all-Ni-based functional electrodes. Journal of Energy Chemistry 2020;40:65–74. https://doi.org/10.1016/j.jechem.2019.02.014.

[149] Frey DD, Engelhardt F, Greitzer EM. A role for "one-factor-at-a-time" experimentation in parameter design. Res Eng Design 2003;14:65–74. https://doi.org/10.1007/s00163-002-0026-9.

[150] Zeng Z, Qian Y, Zhang Y, Hao C, Dan D, Zhuge W. A review of heat transfer and thermal management methods for temperature gradient reduction in solid oxide fuel cell (SOFC) stacks. Applied Energy 2020;280:115899. https://doi.org/10.1016/j.apenergy.2020.115899.

[151] Li Z, Bello IT, Wang C, Yu N, Chen X, Zheng K, et al. Revealing interactions between the operating parameters of protonic ceramic electrolysis cell: A modelling study. Applied Energy 2023;351:121886. https://doi.org/10.1016/j.apenergy.2023.121886.

[152] AlZahrani AA, Dincer I. Thermodynamic and electrochemical analyses of a solid oxide electrolyzer for hydrogen production. International Journal of Hydrogen Energy 2017;42:21404–13. https://doi.org/10.1016/j.ijhydene.2017.03.186.

[153] Wang Y, Banerjee A, Wehrle L, Shi Y, Brandon N, Deutschmann O. Performance analysis of a reversible solid oxide cell system based on multi-scale hierarchical solid oxide cell modelling. Energy Conversion and Management 2019;196:484–96. https://doi.org/10.1016/j.enconman.2019.05.099.

[154] Vojdani M, Fakhari I, Ahmadi P. A novel triple pressure HRSG integrated with MED/SOFC/GT for cogeneration of electricity and freshwater: Techno-economic-environmental assessment, and multi-objective optimization. Energy Conversion and Management 2021;233:113876. https://doi.org/10.1016/j.enconman.2021.113876.

[155] Deb K. Multi-objective Optimisation Using Evolutionary Algorithms: An Introduction. In: Wang L, Ng AHC, Deb K, editors. Multi-objective Evolutionary Optimisation for Product Design and Manufacturing, London: Springer London; 2011, p. 3–34. https://doi.org/10.1007/978-0-85729-652-8_1.

[156] Deb K, Pratap A, Agarwal S, Meyarivan T. A fast and elitist multiobjective genetic algorithm: NSGA-II. IEEE Transactions on Evolutionary Computation 2002;6:182–97. https://doi.org/10.1109/4235.996017.

[157] Deb K, Jain H. An Evolutionary Many-Objective Optimization Algorithm Using Reference-Point-Based Nondominated Sorting Approach, Part I: Solving Problems With Box Constraints. IEEE Transactions on Evolutionary Computation 2014;18:577–601. https://doi.org/10.1109/TEVC.2013.2281535.

[158] Jain H, Deb K. An Evolutionary Many-Objective Optimization Algorithm Using Reference-Point Based Nondominated Sorting Approach, Part II: Handling Constraints

and Extending to an Adaptive Approach. IEEE Trans Evol Computat 2014;18:602–22. https://doi.org/10.1109/TEVC.2013.2281534.

[159] Etghani MM, Shojaeefard MH, Khalkhali A, Akbari M. A hybrid method of modified NSGA-II and TOPSIS to optimize performance and emissions of a diesel engine using biodiesel. Applied Thermal Engineering 2013;59:309–15. https://doi.org/10.1016/j.applthermaleng.2013.05.041.

[160] Mojaver P, Khalilarya S, Chitsaz A, Assadi M. Multi-objective optimization of a power generation system based SOFC using Taguchi/AHP/TOPSIS triple method. Sustainable Energy Technologies and Assessments 2020;38:100674. https://doi.org/10.1016/j.seta.2020.100674.

[161] Sarkar A. A TOPSIS method to evaluate the technologies. International Journal of Quality & Reliability Management 2014;31:2–13. https://doi.org/10.1108/IJQRM-03-2013-0042.

[162] Jing R, Wang M, Wang W, Brandon N, Li N, Chen J, et al. Economic and environmental multi-optimal design and dispatch of solid oxide fuel cell based CCHP system. Energy Conversion and Management 2017;154:365–79. https://doi.org/10.1016/j.enconman.2017.11.035.

[163] Li Z, He Q, Xia L, Xu Q, Cheng C, Wang J, et al. Effects of cathode thickness and microstructural properties on the performance of protonic ceramic fuel cell (PCFC): A 3D modelling study. International Journal of Hydrogen Energy 2022;47:4047–61. https://doi.org/10.1016/j.ijhydene.2021.11.022.

[164] Jang D, Kim J, Kim D, Han W-B, Kang S. Techno-economic analysis and Monte Carlo simulation of green hydrogen production technology through various water electrolysis technologies. Energy Conversion and Management 2022;258:115499. https://doi.org/10.1016/j.enconman.2022.115499.

[165] Cao Y, parikhani T. A solar-driven lumped SOFC/SOEC system for electricity and hydrogen production: 3E analyses and a comparison of different multi-objective optimization algorithms. Journal of Cleaner Production 2020;271:122457. https://doi.org/10.1016/j.jclepro.2020.122457.

[166] Sun Y, Lu J, Liu Q, Shuai W, Sun A, Zheng N, et al. Multi-objective optimizations of solid oxide co-electrolysis with intermittent renewable power supply via multi-physics simulation and deep learning strategy. Energy Conversion and Management 2022;258:115560. https://doi.org/10.1016/j.enconman.2022.115560.

[167] Duan C, Tong J, Shang M, Nikodemski S, Sanders M, Ricote S, et al. Readily processed protonic ceramic fuel cells with high performance at low temperatures. Science 2015;349:1321–6. https://doi.org/10.1126/science.aab3987.

[168] Wrubel JA, Gifford J, Ma Z, Ding H, Ding D, Zhu T. Modeling the performance and faradaic efficiency of solid oxide electrolysis cells using doped barium zirconate perovskite electrolytes. International Journal of Hydrogen Energy 2021;46:11511–22. https://doi.org/10.1016/j.ijhydene.2021.01.043.

[169] Hinata K, Sata N, Costa R, Iguchi F. High Temperature Elastic Modulus of Proton Conducting Ceramics Y-Doped Ba(Zr,Ce)O3. ECS Meeting Abstracts 2020;MA2020-02:2617–2617. https://doi.org/10.1149/MA2020-02402617mtgabs.